

Low Cost Thermal Imaging System for Welding Applications

by
Christopher Gobbi

A thesis
presented to the University of Waterloo
in fulfilment of the
thesis requirement for the degree of
Master of Applied Science
In
Mechanical Engineering

Waterloo, Ontario, Canada, 2016

©Christopher Gobbi 2016

AUTHOR'S DECLARATION

I hereby declare that I am the sole author of this thesis. This is a true copy of the thesis, including any required final revisions, as accepted by my examiners. I understand that my thesis may be made electronically available to the public.

Abstract

A significant component of welding research is devoted to studying the relationship between welding parameters and material properties. The fundamental link between process parameters and material properties is established through the thermo-physical history of the material. Currently, there are very few measurement techniques that are suitable for quantifying the local thermal history induced by welding, and as a result, the application of fundamental materials science principles is severely limited in the welding industry. The goal of the following report is to develop a low cost CCD based thermal imaging camera which can be used to provide thermal feedback information for welding applications. The details regarding the design and operation of the thermal imaging system and calibration equipment are discussed. In addition, the performance characteristics of the thermal camera system is investigated under a variety of operation conditions. It was found that the newly developed system is capable of measuring the temperature of steel alloys across the 800°C to 500°C range required for direct T8/5 time measurement and microstructure prediction applications.

Acknowledgements

I would like to take this opportunity to thank Professor Adrian Gerlich for his mentorship during this project. In particular, I would like to thank him for his assistance with the editing of this report. Finally, I would like to express gratitude towards my parents for their continual support.

Table of Contents

AUTHOR'S DECLARATION	ii
Abstract.....	iii
Acknowledgements.....	iv
List of Figures	viii
List of Tables	xi
List of Abbreviations	xii
List of Symbols	xiii
Chapter 1: Introduction	1
1.1. Historical Welding Trends: Art before Science	1
1.2. Modern Welding Science: A Multidisciplinary Endeavour.....	3
1.3. Materials Science for Welding Applications: Great Potential.....	5
1.4. Conventional Welding Process Development: Opportunities for Improvement	8
1.5. Problem Identification: Moving from art to science.....	9
1.5.1. Academic Perspective.....	10
1.5.2. Industrial Perspective	10
1.6. Potential Thermal Measurement Techniques	10
1.6.1. Contact Thermal Measurement Techniques	11
1.6.2. Non-Contact Thermal Measurement Techniques	12
1.7. Preliminary Hypothesis: Rudimentary Thermal Imaging	14
1.8. Similar Work Involving Conventional Cameras as Thermal Imaging Devices	15
1.9. Goals and Scope of the Project.....	17
Chapter 2: Thermal Imaging Theory	18
2.1. Thermal Radiation Theory	18
2.2. Fundamentals of Pyrometry	20
2.2.1. Broadband and Single-Band Pyrometers.....	20
2.2.2. Dual and Multi-Band Pyrometers	21
2.3. Additional Thermal Imaging Challenges	22
2.4. Camera Selection Factors for use as a Thermal Imaging Device	24

2.4.1. Image Sensor Technology	24
2.4.2. Lenses and Filters for Near-Infrared Imaging	26
2.4.3. Connectivity and Control Software.....	27
2.5. Sensor-Compensated Model of Dual-Band Pyrometry of a Blackbody	28
Chapter 3: Camera Calibration Equipment	35
3.1. Camera Calibration Test Chamber	35
3.2. Temperature Control System.....	36
3.2.1. Thermocouple Selection and Implementation	37
3.2.2. Ohmic Offset Errors	39
3.2.3. PID Tuning & Ramp Tracking Tests	44
3.3. Dual Camera Spatial Calibration	45
3.4. Measurement System Synchronization	46
3.5. Maintaining an Inert Atmosphere in the Calibration Chamber	47
Chapter 4: Thermal Camera Calibration Procedure.....	52
4.1. Material Selection and Sample Preparation	52
4.2. Imaging Settings and Filter Specification	53
4.3. Data Collection and Processing.....	56
4.3.1. Step 1: Data Collection	56
4.3.2. Step 2: Thermal Calibration Data Extraction	57
4.3.3. Step 3: Separation of Valid and Invalid Thermal Calibration Results	58
4.3.4. Step 4: Identification of Thermal Calibration Polynomial	62
4.3.5. Step 5: Apply the Thermal Camera Calibration Polynomial	62
Chapter 5: Thermal Calibration Results	65
5.1. Calibration Repeatability Study	65
5.1.1. Repeatability of Separate Samples	65
5.1.2. Repeatability of Consecutive Testing	66
5.2. Influence of Imaging Settings on Calibration Results	69
5.3. Effect of Surface Type and Perspective Angle	72
Chapter 6: Conclusions and Recommendations	74
References	78

Appendix A: Camera Calibration Chamber Dimensional Drawings	81
Appendix B: LabView Thermal Measurement and Control System.....	94
Appendix C: Dual Camera Graphical User Interface	97
Appendix D: Matlab Data Processing Code: Image_Processor_2CameraCalibrationProcessor_2.m	98
Appendix E: Matlab Thermal Image Code: ThermallImageGenerator2.m	101

List of Figures

Figure 1: Ancient artwork of Egyptian silversmith performing braze joining [2].....	1
Figure 2: World War 2 welding application of shielded metal arc welding (SMAW) process [4].....	2
Figure 3: Welding science and some of its relevant disciplines.....	3
Figure 4: Schematic representation of SMAW [6]	4
Figure 5: Key components of materials science and engineering [10]	5
Figure 6: Schematic cross section of weld microstructural regions [13]	6
Figure 7: a) Iron-Carbon phase diagram [14]; b) TTT diagram of AISI 1050 steel [14]; c) generic solidification diagram [6].....	7
Figure 8: Typical arc welding process inputs in relation to measurable outputs	8
Figure 9: Multiphysics computer simulation of electron beam weld [16].....	11
Figure 10: Scanning pyrometer applications by HKS Prozesstechnik; a) High frequency induction welding; b) GMAW [17]	12
Figure 11: FLIR A315/A615 thermal imaging camera [18].....	13
Figure 12: Hot iron surface with visible thermal gradients [19]	14
Figure 13: Dual wavelength CCD pyrometry image of molten copper heated by induction coil [21].....	15
Figure 14: a) Schematic of dual-camera high speed CCD thermal imaging [22]; b) Raw image (left) and thermal image (right) of Laser weld [22]; c) Raw image (left) and thermal image (right) of GMAW droplet [23].....	16
Figure 15: Spectral blackbody emissive power at various temperatures in Kelvin, modified from [25]....	19
Figure 16: a) Schematic spectral emissivity of a real surface; b) Schematic directional emissivity of a real surface [26]	20
Figure 17: Correlation of radiation intensity ratio and temperature, modified from reference [25]	22
Figure 18: Normal total emittance of oxidized stainless steels with various surface conditions [28]	23
Figure 19: Photoelectric transduction by a semiconductor [29]; colour CCD sensor schematic [30]	24
Figure 20: Spectral sensitivity of SONY ICX618 CCD sensor [31]	25
Figure 21: a) Combined spectral sensitivity of Sony ICX618 with colour Bayer filter [32];	26
Figure 22: Spectral transparency of an IR reduction filter from a CCD camera [32]	26
Figure 23: a) Edmund Optics anti-reflective coating spectral range; b) Edmund Optics 67-716 VIS-NIR lens [33].....	27
Figure 24: DMK 23U618 camera which includes Imaging Control 3.4 software development kit	28

Figure 25: Blackbody spectral responses for temperatures of interest	29
Figure 26: Polynomial approximation of Sony ICX618 sensor spectral sensitivity, modified from [31].....	29
Figure 27: Spectrally corrected CCD response to blackbody radiation	30
Figure 28: Spectrally corrected CCD response with logarithmic scale	31
Figure 29: Theoretical sensor intensity of bandpass filter ratios for blackbody radiation	33
Figure 30: Thermal measurement range for filters separated by 150nm	34
Figure 31: Thermal measurement range for filters separated by 50nm	34
Figure 32: Camera calibration test chamber schematic	36
Figure 33: Schematic of closed loop temperature control system.....	37
Figure 34: a) Single-band thermal image showing welded thermocouple junctions; b) Isotherms visualized by colour map	37
Figure 35: a) Circuit diagram of Joule heated specimen; b) Thermocouple placement error with respect to equipotential line	39
Figure 36: Thermocouple locations of Ohmic offset voltage test specimen	40
Figure 37: Ohmic offset error experiment results	41
Figure 38: a) Complete error cancelation using AC current; b) Incomplete error cancelation	41
Figure 39: Ohmic offset error sampling harmonics (1Hz sampling rate).....	42
Figure 40: Ohmic offset error after AC duty cycle balancing procedure (60Hz AC, 1Hz sampling, 10A)....	43
Figure 41: a) Step tracking response; b) Ramp tracking response	44
Figure 42: Camera tilt angle and X-axis spatial compression factor.....	45
Figure 43: Spatial mismatch between camera A and camera B	46
Figure 44: Synchronization of images and thermal feedback data	46
Figure 45: left) Dual camera control GUI; right) Thermal control and data logging GUI.....	47
Figure 46: Mixing chamber schematic	48
Figure 47: Oxygen concentration during argon purge process	48
Figure 48: Visual effect of oxidation on emissivity (570°C, 850nm filter, sandblasted preparation).....	49
Figure 49: Effect of oxidation on average pixel value at 570°C and 850nm	49
Figure 50: SEM image and energy dispersive x-ray (EDX) chemical analysis of fractured oxide layer	50
Figure 51: Sandblasted steel shielded with argon nozzle after cycling at 800°C.....	51
Figure 52: Visual effect of oxidation on emissivity (800°C, 850nm filter)	51

Figure 53: Effect of oxidation on average pixel value a sandblasted steel sample at 800°C.....	51
Figure 54: Dimensions of the standardized thermal camera calibration test specimen	52
Figure 55: Examples of polished and sandblasted thermal camera calibration test specimens	53
Figure 56: 800nm bandpass filter spectral transmissivity [38]	55
Figure 57: 900nm bandpass filter spectral transmissivity [39]	55
Figure 58: Synchronization of temperature ramp, thermocouple measurements, and image acquisition	57
Figure 59: Surface appearance of heated steel specimen, highlighting region of interest for extracting thermal image calibration data.....	57
Figure 60: Maximum camera pixel values for both cameras versus thermocouple temperature measurments and the identification of a signal inflection	59
Figure 61: Identification of signal inflection temperature by using the maxima of pixel range curve.....	60
Figure 62: Instability of standard deviation results at low signal intensities.....	61
Figure 63: Valid thermal measurement range with respect to average pixel intensity and pixel ratio	61
Figure 64: 5 th order polynomial fit for pixel intensity ratio measured for cameras using 800 and 900 nm filters	62
Figure 65: Selection of a thermal analysis ROI.....	63
Figure 66: Pixel homogeneity with varrying degrees of Gaussian blurr a) $\sigma=0$; b) $\sigma=2$; c) $\sigma=4$; d) $\sigma=8$	64
Figure 67: Temperature map generated by the CCD imaging system.....	64
Figure 68: Thermal calibration repeatability tests using separate samples (Settings: Sandblasted surface oriented at 0°, imaging at 15Hz, and 0dB gain)	66
Figure 69: Thermal calibration repeatability tests using the same sample (Settings: Polished surface oriented at 0°, imaging at 4Hz and 0dB gain)	67
Figure 70: Comparisson of standard deiation in thermal calibration data between sandblasted and polished samples (Settings: surface oriented at 0°, imaging at 15Hz and 0dB gain).....	68
Figure 71: Thermal calibration results for various camera settings	69
Figure 72: Example application of high dynamic range imaging [40]	70
Figure 73: Evidence of spectral peaks through comparing simulated and measured pixel intensity ratios.	71
Figure 74: Thermal calibration comparisson between surface types and perspective angles.....	72

List of Tables

Table 1: Peak signal intensities and adjacent ratios	31
Table 2: K-type thermocouple issues reported for high temperature applications [36], [37]	38
Table 3: Standardized exposure frequency and gain settings	54
Table 4: Thermal measurement capabilities of the standardized camera settings.....	69
Table 5: Thermal measurement discrepancy between surface types.....	73
Table 6: Thermal measurement discrepancy between viewing angles.....	73

List of Abbreviations

A – Amperes
AC – Alternating Current
AWG – American Wire Gauge
CCD – Charge Coupled Device
CCT – Continuous Cooling Transformation
CMOS – Complementary Metal Oxide Semiconductor
dB – Decibel
DC – Direct Current
EDX – Energy Dispersive X-Ray
FWHM – Full Width Half Max
GMAW – Gas Metal Arc Welding
GTAW – Gas Tungsten Arc Welding
GUI – Graphical User Interface
HDRI – High Dynamic Range Imaging
Hz – Hertz
I – Conventional Current
IR – Infrared
NIR – Near Infrared
PID – Proportional-Integrative-Differential
PPM – Parts Per Million
R – Resistance
ROI – Region of Interest
RSW – Resistance Spot Welding
SEM – Scanning Electron Microscopy
SMAW – Shielded Metal Arc Welding
TTT – Time Temperature Transformation
V – Voltage

List of Symbols

$E_{\lambda, \text{blackbody}}$ – blackbody spectral emissive power ($\text{W}/\text{m}^2 \cdot \mu\text{m}$)

h – Planck constant ($6.626 \times 10^{-34} \text{ J}\cdot\text{s}$)

c_o – speed of light in vacuum ($2.998 \times 10^8 \text{ m/s}$)

λ – wavelength (μm)

k_B – Boltzmann constant ($1.381 \times 10^{-23} \text{ J/K}$)

T – temperature ($^{\circ}\text{K}$)

ϵ – emissivity

Chapter 1: Introduction

The purpose of this chapter is to provide the reader with sufficient background information so as to understand the motivation for the following work. To accomplish this goal, it is necessary to briefly discuss current trends in welding research within a broader historical context. This historical discussion has been provided in order to help emphasize long term trends and highlight their ongoing effects in modern welding engineering.

1.1. Historical Welding Trends: Art before Science

Ever since humans first discovered metals, they have looked for ways to weld them. Be it for tools or trinkets, archeological evidence of small-scale soldering and forge welding has been found from as far back as 3000 BC [1]. Despite their limited scientific understanding, ancient civilizations have managed to find ways to weld metals such as copper, gold, and iron. Although the accomplishments of these ancient welders is impressive, primitive welding was still slow, laborious, and only suitable for a handful applications.



Figure 1: Ancient artwork of Egyptian silversmith performing braze joining [2]

The basic welding techniques of ancient times would remain relatively unchanged for many centuries; improving very little even with the surge of technological developments that occurred during the industrial revolution. It was not until the arrival of inexpensive electricity during the early 1900's that new life was sparked into the field of welding. In just a few decades, many of the modern electric welding processes, such as Resistance Spot Welding (RSW), Shielded Metal Arc Welding (SMAW), Gas Metal Arc Welding (GMAW) and Gas Tungsten Arc Welding (GTAW), had been developed and adopted by industry to great success [3]. Although much more scientific knowledge was available to engineers and researchers during the debut of the electric welding processes, the surge of innovation in welding applications far outpaced the maturation of the corresponding welding science. As a result, welding had developed into a major industrial process even though many of the details behind its operation were still a mystery. Since then, several decades of welding research have greatly enhanced the understanding of welding, however, welding is still often regarded as somewhat of a technical art form rather than a truly scientific discipline.



Figure 2: World War 2 welding application of shielded metal arc welding (SMAW) process [4]

The inclusion of this brief review of welding history has been provided in order to illustrate an underlying and ongoing theme: welding is a combination of an art and a science [5]. Uncovering the reasons behind this theme, as well as its ongoing effects on modern welding science, are important to the overall motivation of this project.

1.2. Modern Welding Science: A Multidisciplinary Endeavour

A major reason why it has always been challenging for welding engineers to rely entirely on scientific principles is because welding science is very multidisciplinary. Some of the various scientific and engineering disciplines which are relevant to welding are summarized in Figure 3.

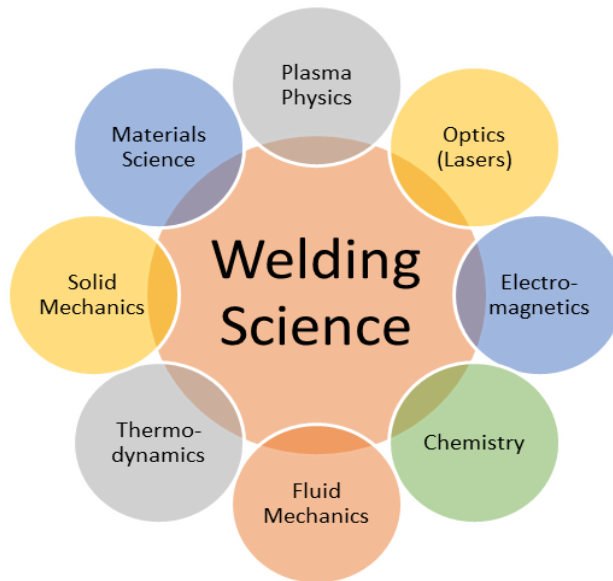


Figure 3: Welding science and some of its relevant disciplines

As a brief illustration of how these topics are relevant to everyday welding, consider the physical principles involved in performing a weld with a common process such as SMAW. A schematic representation of SMAW is provided in Figure 4. SMAW is an arc welding process, therefore an understanding of plasma physics and electromagnetics is highly relevant. In addition, understanding the high temperature reactions between the flux and molten metals involves the field of chemistry. An understanding of fluid mechanics is also required in order to describe the flow of the molten weld pool and its interactions at the various fluid interfaces. Thermodynamics is also important since large amounts of heat are being transferred through the electrode and base metal. Solid mechanics principles such as stress and fatigue are important to ensure that the size and shape of the weld is sufficient for the application. Finally, a clear understanding of materials science is necessary in order to understand concepts such as solidification and solid state phase transformations.

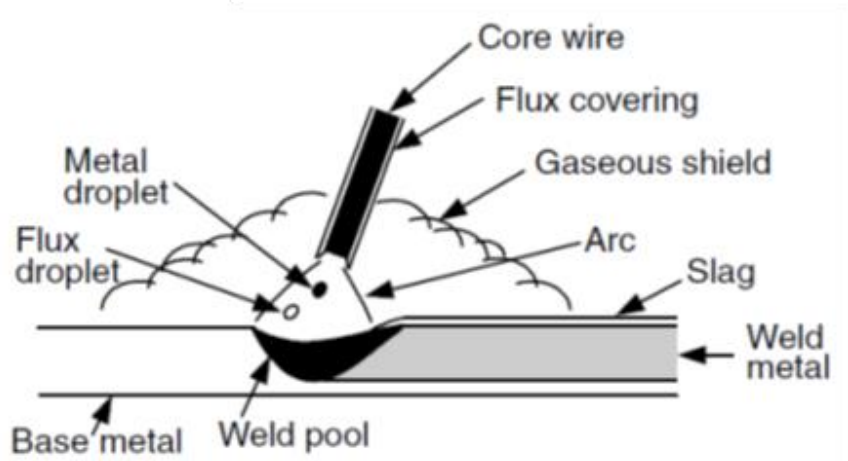


Figure 4: Schematic representation of SMAW [6]

Fortunately for welding researchers, many of the physical principles that are relevant to welding have already been studied and explained within the surrounding scientific disciplines listed in Figure 3. Although many of relevant physical principles have been adequately described individually, their incorporation into welding science requires that they be described simultaneously. Unfortunately, a general theory or model of welding has not yet been successfully developed due to the complexities involved in solving highly coupled systems at extreme operating conditions. The capabilities of computer simulations have been steadily increasing in order to better accommodate the complex nature of welding [7] [8] [9], however, these simulation programs have yet to make a significant impact on the majority of practical welding applications. As a result, it is still necessary for welding engineers and researchers to rely heavily on experience, qualitative reasoning, generalizations, and intuition. Although these traditional techniques can be quite effective, the limitations of the semi-scientific approach can become significant in certain applications. One such area where the current approach is quite limiting is in the realm of welding materials science.

1.3. Materials Science for Welding Applications: Great Potential

One of the major areas of ongoing welding research is the study of materials science for welding applications. From a conceptual point of view, the goal of materials science is to understand the physical laws which govern the relationships between a material's chemistry, processing, structure, properties, and performance. As depicted in Figure 5, the conceptual relationships are manifested through the underlying core physical principles of thermodynamics, reaction kinetics, and crystallography [6] [10] [11]. Furthermore, it is important to note that a comprehensive understanding of the material's performance cannot be properly appreciated without relying on the innermost principles.

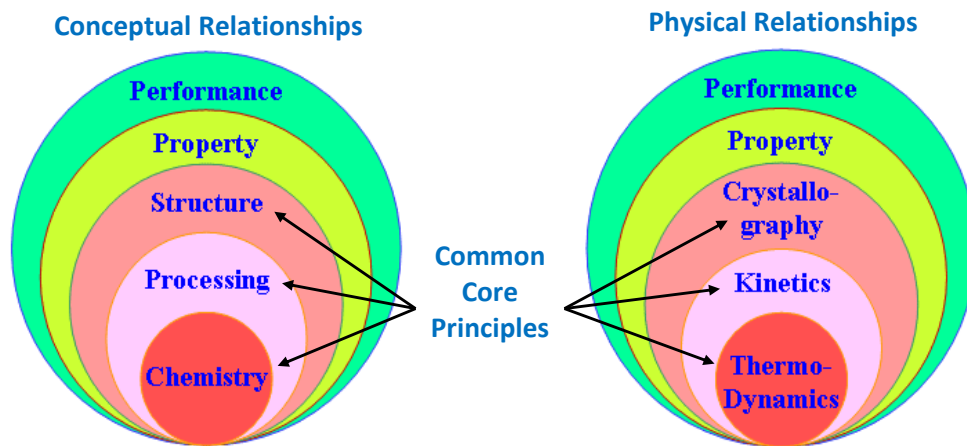


Figure 5: Key components of materials science and engineering [10]

Due to the tremendous amount of work which has already gone into materials research, many engineering materials are quite well understood at the core levels shown in Figure 5. For example, thermodynamic information about a material's equilibrium phases is available through the phase diagram. Reaction kinetics information regarding the influence of thermal processing on the transformation between phases and morphologies is available through the Time-Temperature Transformation (TTT) and solidification diagrams [12]. Crystallography information about the atomic structure and arrangement of a material is observable through optical and scanning electron microscopy (SEM).

The aforementioned tools are routinely applied to great effect for the study of common manufacturing processes such as casting or heat treatment. Since welding applications can be thought of as a localized casting and heat treating process, the same materials engineering tools can be applied across the various sub regions of a weld. A schematic cross-section of a common fusion weld, its microstructural subzones, and examples of some of the available analysis tools are included in Figure 6 and Figure 7. These diagrams are useful engineering tools which describe the relationships between thermal history and microstructure, and are the key to understanding how mechanical properties develop.

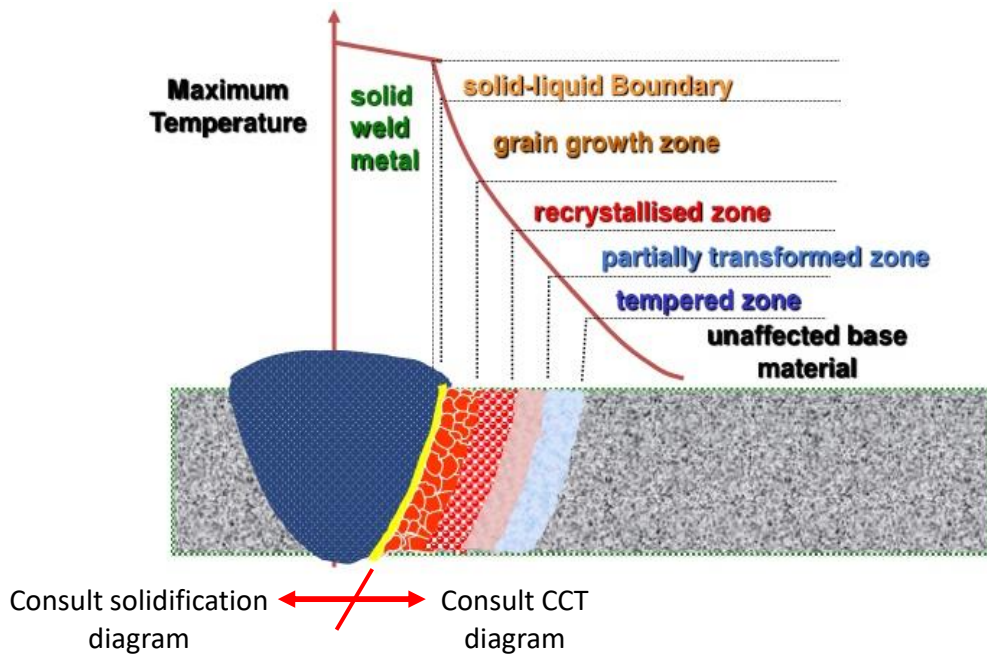


Figure 6: Schematic cross section of weld microstructural regions [13]

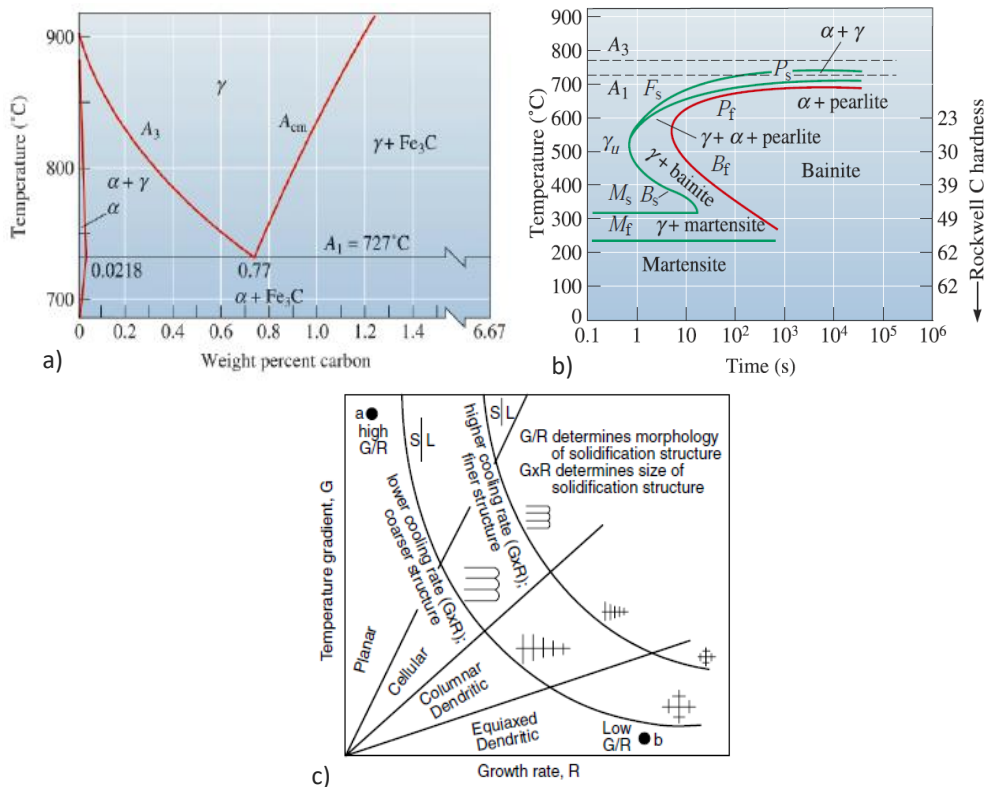


Figure 7: a) Iron-Carbon phase diagram [14]; b) TTT diagram of AISI 1050 steel [14]; c) generic solidification diagram [6]

Although a significant amount of materials science information is available for materials that are commonly welded, it is rare that this information can be easily applied to practical applications. Since reaction kinetics are a major factor involved in defining the primary materials science relationships, even the most basic materials science relationships can only be applied quantitatively if the thermo-physical history of the material is known. For conventional materials science, the thermo-physical history is relatively easy to specify and measure. For example, the heating rate of a furnace, hold time, and quenching rate are parameters which can be readily chosen, verified, and related directly to the thermal history. In contrast, the available input parameters for welding applications are much more complex and far removed from defining the localized thermal histories. Figure 8 includes a graphic representation of how the measurable inputs of a welding process are far removed from the governing factors that must be known in order to apply materials science data directly. The fact that welding applications are missing the

fundamental kinetics information constitutes a massive limitation for the application of materials science data to welding applications.

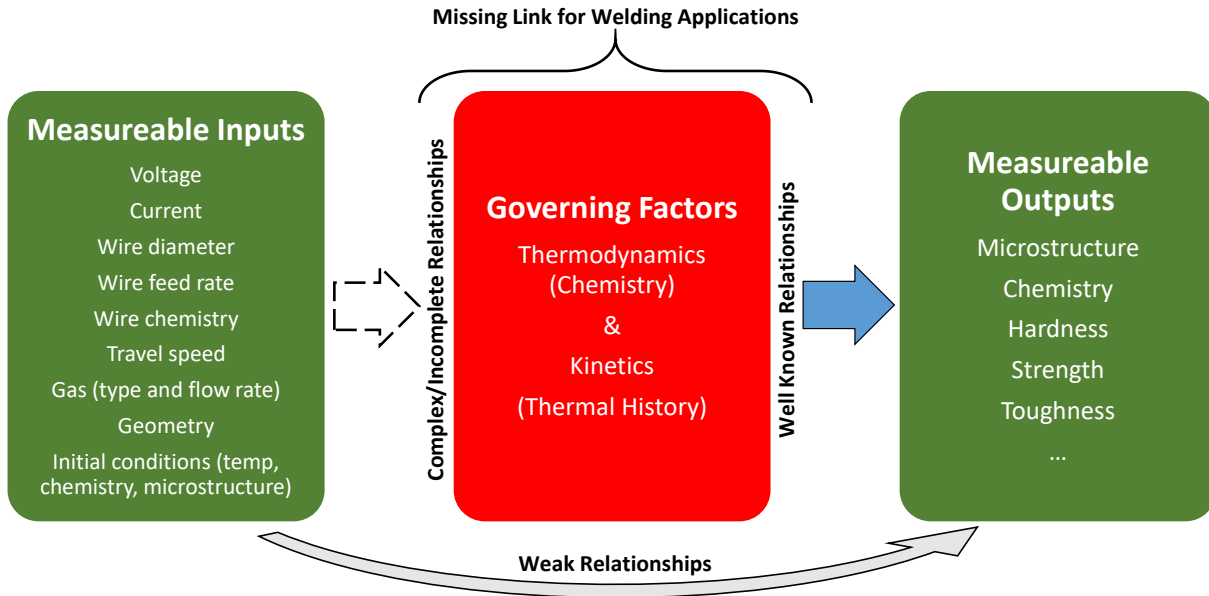


Figure 8: Typical arc welding process inputs in relation to measurable outputs

1.4. Conventional Welding Process Development: Opportunities for Improvement

Although thermal history information is seldom available for welding applications, welding engineers and researchers still apply a significant amount of materials science principles in a qualitative manner. For example, a typical welding development project begins by selecting welding parameters through consulting a combination of welding codes, manufacturer recommendations, and previous experience [15]. Test welds are performed using the recommended parameters and then inspection coupons are cut and polished to study the microstructure, hardness, strength, and any other parameters of interest. When the observed microstructure and properties do not match the desired results, the welding engineer or researcher applies their qualitative understanding of materials principles to interpret how the thermal history should be changed in order to improve the properties. Past experience and intuition are then used to identify a new set of welding which may provide a desirable thermal history, often by iteration or trial and error until the desired performance is achieved.

Although the conventional welding development process described here is sufficient at achieving good final results, there are many disadvantages associated with the current process. First of all, this process is very indirect, labour intensive, and time consuming. In addition, since the final procedures are not linked directly to any underlying principles, such as chemistry and thermal history, the results of a given study cannot be readily transferred to similar processes or alloys. This shortcoming significantly increases the amount of work required to develop welding procedures and weakens the link between research activities and practical applications. A final disadvantage of the current process is that it relies largely on destructive testing; which cannot be repeated on the final product. Since there is currently no method of observing and comparing the thermal histories of the test welds and actual welds, the only way to be confident that the final part possesses the desired properties is to employ significant process control measures which ensure that the process conditions are identical the test conditions. In general, it is evident that the current welding development process is not ideal.

1.5. Problem Identification: Moving from art to science

Considering the historical trends in welding, it was possible to identify the underlying trend that welding is a combination of an art and a science [5]. Given both the specific challenges and relative successes involved in modern welding science, an appreciation for the accomplishments of the art-science duality was presented. Through discussing of the capabilities of modern materials science, and its incomplete adoption by welding applications, an area of potential improvement has been identified. The inconvenience and limitations of the current welding development approach has provided an additional source of motivation to pursue potential improvements. Finally, the root cause behind the problem has been identified as the lack of thermal history information. Based on this problem, a need statement can be given from the two following perspectives:

1.5.1. Academic Perspective

- A method of measuring the thermal histories induced by welding is needed to provide greater insight into the study of welding processes.
- The knowledge of thermal history will allow welding researchers to leverage the vast collective resources of materials science.

1.5.2. Industrial Perspective

- A way to monitor the thermal history of welded components is needed since controlling the traditional input variables does not directly guarantee the desired properties have been achieved.
- Quality control measures can be based on thermal history information.

1.6. Potential Thermal Measurement Techniques

Now that the problem and motivation behind this work have been identified and attributed to a long-existing lack of thermal history information, it is necessary to consider the thermal measurement techniques that may be useful for solving the problem. In order to assess the suitability of the available techniques, it is important to first understand the needs of the given application. For example, fusion welding of steel requires the formation of a molten weld pool. The melting point of steel occurs at roughly 1550°C, and significant microstructural phase transformations occur while cooling through the range of 800°C-500°C¹. As a result, the desired thermal measurement technique must be able to measure high temperatures. Furthermore, the technique must be able to withstand the rigors of industrial welding applications while being practical to use and economical to implement. The combination of these requirements are certainly not easy to fulfill, and so it is likely that very few

¹ The time required to cool from 800°C to 500°C is an important parameter for assessing the final microstructure and properties of a steel alloy. This time is often called the T8/5 time.

measurement techniques will be suitable. Before continuing on to the discussion of the potential measurement techniques, it is beneficial to take a moment to acknowledge that computer simulation is also a viable approach to improving the knowledge of thermal history information for welding. Welding simulation programs are growing in both capability and popularity, however, it is always desirable to have direct measurement capability as well. Although simulation is an interesting and worthwhile topic, the goal of the work contained in this report is the improvement of direct measurement techniques.

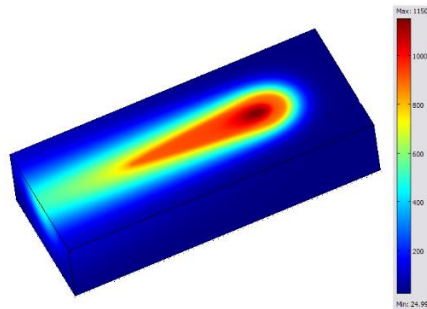


Figure 9: Multiphysics computer simulation of electron beam weld [16]

1.6.1. Contact Thermal Measurement Techniques

The most common and inexpensive form of thermal measurement techniques are the contact measurement techniques; or those which rely on physical contact with the surface being measured. The most basic forms of contact measurement transducers, such as liquid volumetric expansion and bimetallic strip thermometers, are clearly not suitable for this application. Other transducers based on electrical effects, such as thermistors and thermocouples, do offer adequate properties such as precision, high temperature capability, dynamic range, responsiveness, durability, and affordability. Unfortunately, thermocouples and thermistors provide temperature measurements at only a single point location. Since welding applications involve highly localized heating and large thermal gradients, measuring the temperature at a single point along a weld is unlikely provide sufficient detail about the thermal history across the various welding zones. As a result, an array of many sensors would be required in order to have a chance at gathering the required thermal history information. The need to connect many

thermocouple sensors prior to welding may be accommodated in a laboratory environment, however, it would be far too impractical for most industrial applications. In summary, the available contact measurement techniques are not suitable for this application.

1.6.2. Non-Contact Thermal Measurement Techniques

An additional classification of thermal measurement techniques are the non-contact methods; or those which sense temperature based on thermal radiation. Standard pyrometers are not overly expensive and can measure temperature accurately over the desired temperature range, however, much like a thermocouple, they only provide thermal information about a single location. The pyrometer can be made more suitable to welding applications by scanning the pyrometer back and forth across the weld zone to measure the temperature along a line or area. The technique of using a raster-scanning pyrometer has been used successfully for detecting welding defects and monitoring the cooling rate from 800 to 500°C (or T8/5 time) in tube welding applications. One such system is illustrated in Figure 10.

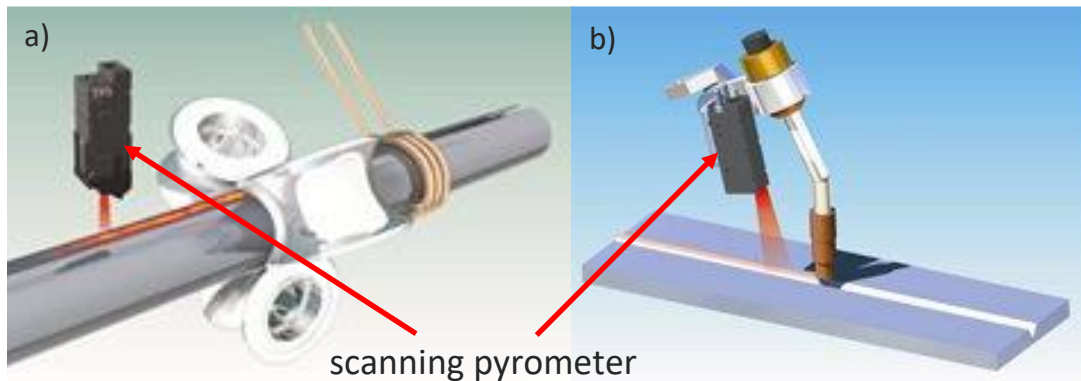


Figure 10: Scanning pyrometer applications by HKS Prozesstechnik; a) High frequency induction welding; b) GMAW [17]

Although the scanning pyrometer approach can successfully monitor for welding defects and measure T8/5 time, the existing systems are quite expensive, require expert knowledge to calibrate, and are limited to use on simple geometries. Since these systems already exist, yet have only been adopted by a few specialty applications, it is evident that a more capable system is needed for general welding applications.

The most advanced non-contact thermal measurement technique is the use of a thermal imaging camera. Since a thermal imaging camera is essentially a high density pyrometer array, thermal cameras share all the benefits of pyrometers while providing much more spatial information about the temperature distribution across the weld. Figure 11 shows a sample thermal image which illustrates the high dynamic range and spatial resolution possible with current infrared cameras.



Figure 11: FLIR A315/A615 thermal imaging camera [18]

A thermal imaging system based on conventional thermal cameras would surely have high potential for use as a welding thermal monitoring device, however, there are several limitations to this approach. The first limitation behind the use of a commercial thermal cameras is their high cost; although costs are gradually decreasing towards more practical levels. Another limitation is the fact that the most affordable thermal cameras only measure broadband thermal radiation and require an emissivity correction factor. Since many welding applications do not have consistent emissivity, it is likely that the temperature measurements may be erroneous by a significant amount. The details behind why emissivity correction is required will be discussed in Chapter 2: Thermal Imaging Theory. In summary, it seems as though standard thermal imaging cameras may be viable for some applications, but expense and emissivity corrections are major drawbacks.

1.7. Preliminary Hypothesis: Rudimentary Thermal Imaging

Although the review of the available thermal measurement techniques failed to provide a satisfactory solution, an alternative approach is being proposed. Based on everyday experience, it is likely that most individuals have been able to identify a hot surface visually. For example, an incandescent lightbulb or electric toaster element are everyday examples of surfaces that are hot enough to emit significant visible radiation. Similarly, the fusion welding of iron-based alloys also involves temperatures high enough to be visible to the human eye. Figure 12 has been included as an example of how the temperature of iron-based alloys can be qualitatively examined by the human eye.

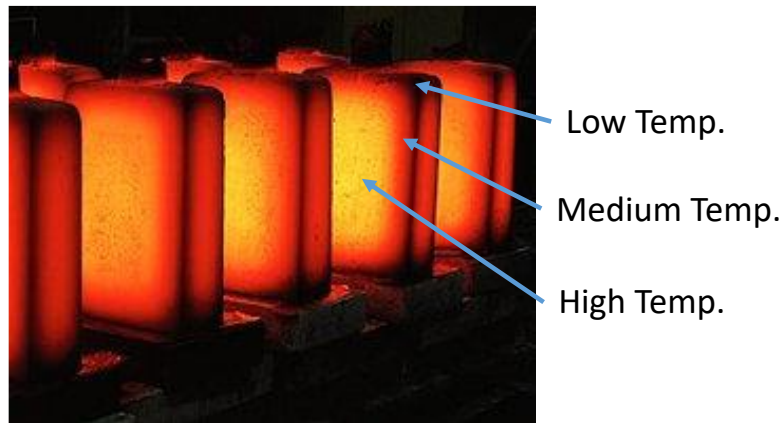


Figure 12: Hot iron surface with visible thermal gradients [19]

For the experienced welder, it is possible to observe the differences between a fast cooling weld and a slow cooling weld by visual inspection. As a result, it is proposed that a standard camera designed for visible light imaging could be modified to observe and quantify the cooling rate of welds performed on high temperature alloys. Due to the very low cost of visible spectrum cameras, it is expected that a low cost emissivity compensated thermal imaging system can be developed using standard cameras and applied to monitor the thermal history of welds.

1.8. Similar Work Involving Conventional Cameras as Thermal Imaging Devices

Before beginning the development of the custom thermal imaging system, a review of similar work was conducted in order to gauge the validity of the preliminary hypothesis and gain any insights which may aid the development process. Several sources were found which confirm the ability to use a low cost standard visible light sensor for high temperature pyrometry measurements. For example, Zauner et al. documented the use of a single camera for measuring a temperature of 350°C for a heat treatment process [20], however, this work required a carefully controlled environment, long exposure times, and emissivity correction in order to provide accurate measurements. A different study by Meriaudeau described the ability to greatly increase the accuracy of a standard camera by using multi-wavelength imaging techniques [21]. A review of how the image sensors and acquisition parameters were calibrated using a controlled grey body was also provided. An example of a thermal image taken by the camera developed by Meriaudeau is included in Figure 13.

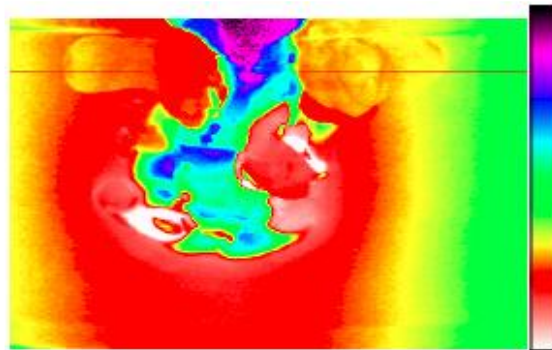


Figure 13: Dual wavelength CCD pyrometry image of molten copper heated by induction coil [21]

Standard high-speed cameras have also been modified by Yamashita for measuring the molten pool temperature of laser welds [22], and by Tanaka for the measurement of molten droplet temperature in GMAW [23]. Examples of thermal images from these studies are included in Figure 14.

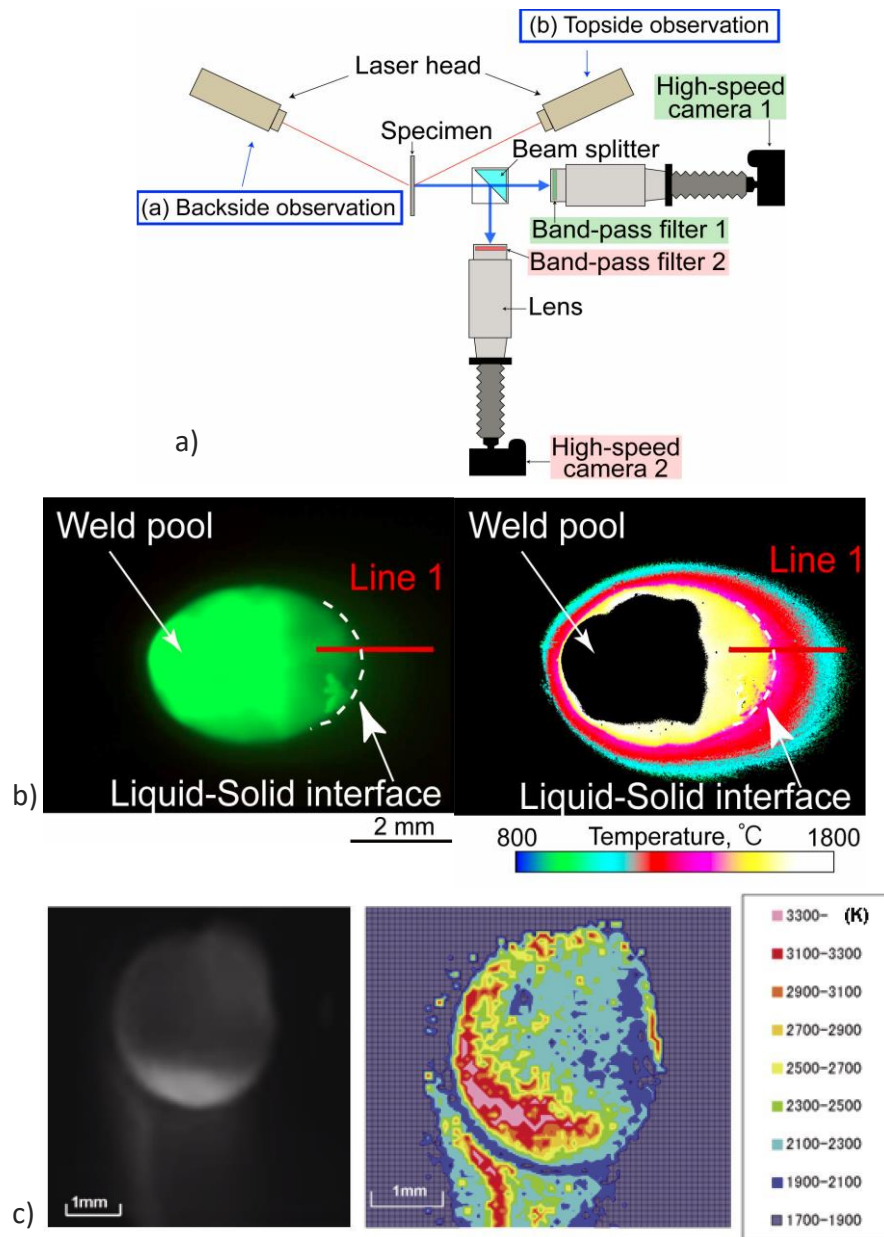


Figure 14: a) Schematic of dual-camera high speed CCD thermal imaging [22]; b) Raw image (left) and thermal image (right) of Laser weld [22]; c) Raw image (left) and thermal image (right) of GMAW droplet [23]

Based on the information contained in these other works in these and other works, it is possible to proceed with confidence that the proposed low cost thermal imaging system can be developed and will be capable of achieving good performance for welding applications.

1.9. Goals and Scope of the Project

The thermal imaging systems which have been reviewed so far were all custom designed for a specific research application. Since these systems are not readily commercially available, the development of a thermal history measurement system for welding applications cannot proceed without first designing and building the thermal imaging system itself. Although some information about the development of similar thermal imaging systems is available from published sources, a significant portion of the development details are not given. As a result, the goals of the following work are to:

- Develop a multispectral thermal imaging system for welding applications which is based on low cost conventional cameras
- Calibrate the system to measure temperatures of interest to steel alloys (800°C to 500°C)
- Describe the development and calibration process in detail

Due to the significant effort involved in developing a new thermal imaging system from the ground up, this report will focus primarily on development process and preliminary thermal measurement results, while the practical use of the camera to record thermal histories and predict microstructures of weldments will be studied in a future report.

Chapter 2: Thermal Imaging Theory

The purpose of this chapter is to describe the background theory relevant to thermal imaging. A basic knowledge of thermal radiation theory is required since it is fundamental to understanding thermal imaging approaches. In addition, this chapter will discuss the important parameters which should be considered when choosing camera equipment for use in a thermal imaging system.

2.1. Thermal Radiation Theory

All atoms consist of protons, neutrons, and electrons which are arranged in quantized energy states. Electrons can change energy levels spontaneously through the absorption or emission of energy in the form of a photon, however, the most stable configuration for the electrons is when they inhabit the lowest available energy states. Similarly, multi-atom systems can change between quantized vibration states through the absorption or emission of a photon, and are most stable when inhabiting the lowest energy vibration mode. The extra kinetic energy stored in group of atoms defines its temperature with respect to absolute zero, or -273°C . Since all practical situations involve objects at temperatures above absolute zero, all surfaces will possess extra thermal energy which is unstable and can be released through the radiant emission of photons.

A surface which emits thermal radiation in an ideal fashion is referred to as a blackbody. The total radiation from a blackbody is distributed across a spectrum of wavelengths and is influenced by the object's temperature according to the Planck Distribution given in Equation 1 [24].

$$\textbf{Equation 1: } E_{\lambda,blackbody}(\lambda,T) = \frac{2\pi hc_o^2}{\lambda^5 \left[e^{\frac{hc_o}{\lambda k_B T}} - 1 \right]}$$

A graphical depiction of the blackbody spectral emissive power from Equation 1 is provided in Figure 15, which illustrates several important traits about blackbody radiation. First of all, increasing the temperature of a blackbody will cause it to emit a greater amount energy overall, as well as at any

particular wavelength. Secondly, increasing the temperature of a blackbody will shift its peak emissive power towards shorter wavelengths. Finally, surfaces which are relevant to welding applications, for example at temperatures of 1000°K or 727°C, emit a small portion of their total energy at visible wavelengths and a larger portion at near-infrared (NIR) or far-infrared wavelengths.

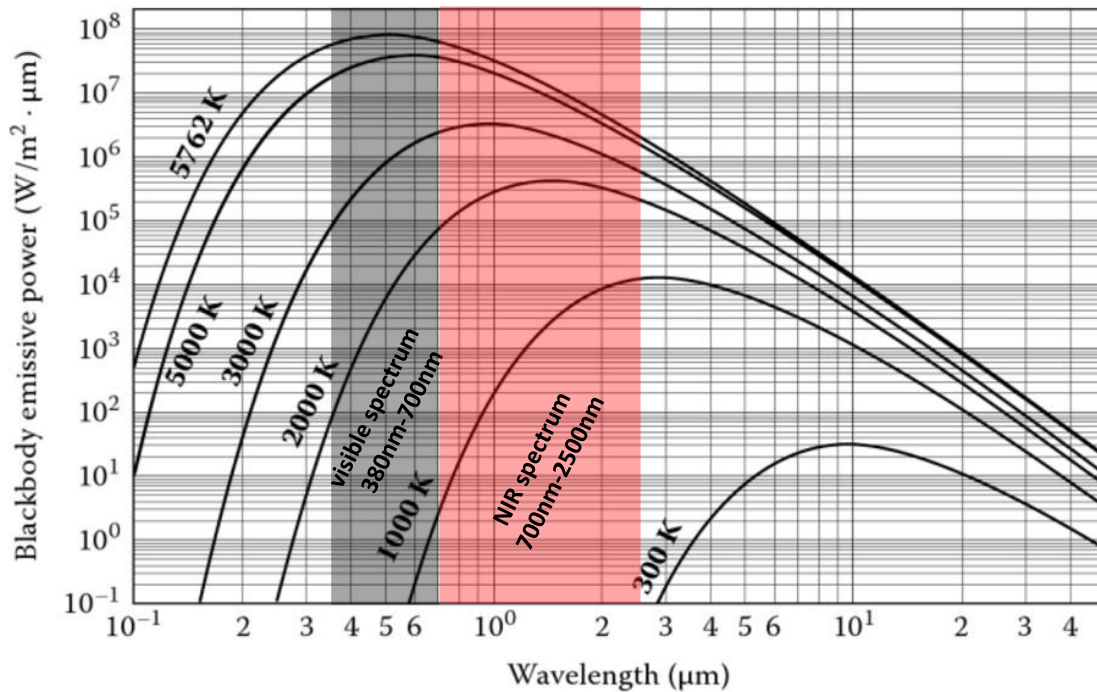


Figure 15: Spectral blackbody emissive power at various temperatures in Kelvin, modified from [25]

In practice, most surfaces are not ideal and do not emit radiation in the exact same manner as a blackbody. The simplest form of non-ideal surface is referred to as a grey-body; which emits its radiation with the same spectral distribution as a blackbody, although at a reduced intensity. The emission from a grey-body is a constant fraction of the blackbody emissive power and is independent of wavelength. As a result, the emission of a grey-body is defined in Equation 2 as equivalent to that a blackbody with a single correction factor called emissivity (ϵ).

$$\text{Equation 2: } E_{\lambda, \text{greybody}}(\lambda, T) = \epsilon \cdot E_{\lambda, \text{blackbody}}$$

Although black and grey-bodies emit an ideal spectral pattern given by the Planck distribution, many real surfaces emit radiation with a different distribution. Since the emission from real surfaces originates from a combination of quantized electronic and vibrational energy transitions, factors such as the chemical composition and surface structure of the material will introduce resonant frequencies which are more likely to emit radiation than others. As a result, real surfaces may have characteristic spectral peaks and an emissivity which is wavelength as well as directionally dependent. Schematic representations of the spectral and directional differences between a real surface and a blackbody are included in Figure 16.

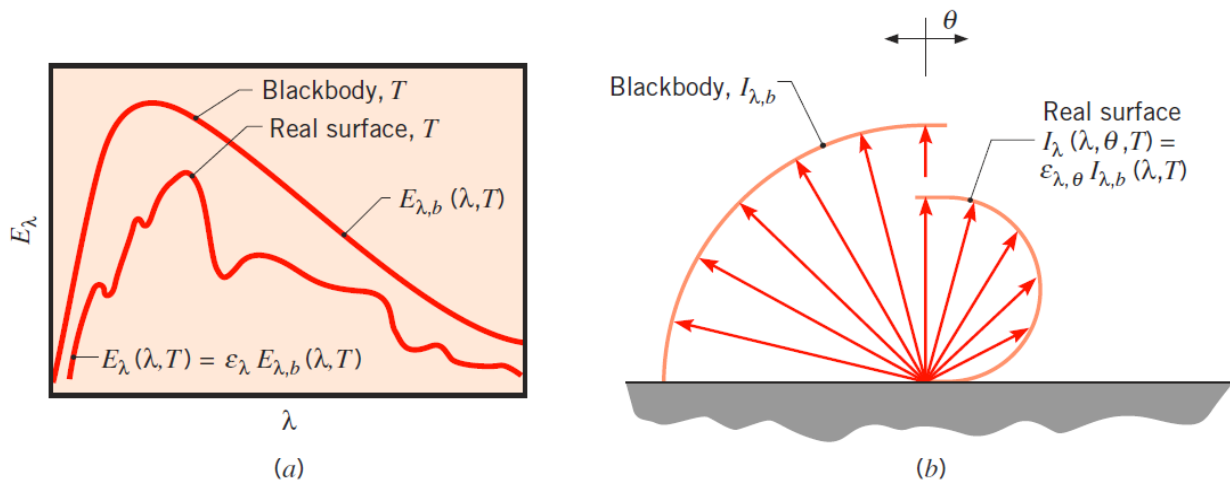


Figure 16: a) Schematic spectral emissivity of a real surface; b) Schematic directional emissivity of a real surface [26]

2.2. Fundamentals of Pyrometry

By applying the basic radiation principles described in Section 2.1: Thermal Radiation Theory, it is possible to explain how thermal radiation can be used to measure a surface's temperature. This measurement technique is referred to as pyrometry, and two common techniques will be discussed in the following sections.

2.2.1. Broadband and Single-Band Pyrometers

The simplest form of pyrometer uses a sensor which detects the intensity of the incident radiation across a single band of wavelengths, $\lambda \pm \Delta\lambda$, where λ is the central wavelength and $\Delta\lambda$ can be either small or large. Since the total intensity of the radiation emitted over the given band will be a function of the

object's temperature, a measurement of radiation intensity is sufficient to estimate the surface temperature. Unfortunately, this type of pyrometry is susceptible to large errors from a variety of sources. For example, consider if a standard camera is used in order to gather and quantify the light being emitted from a hot object. If the size of the lens, aperture, or exposure time are changed, the amount of light arriving at the sensor will be changed even if the temperature of the radiating surface remains the same. In addition, the emissivity of the surface must be known since it affects the relationship between temperature and the intensity of radiation emitted by the surface. As summarized in Equations 3 and 4, any effects which change the radiation intensity departing the source or arriving at the sensor must be accounted for by this type of pyrometer².

$$\textbf{Equation 3: } \textit{Radiant Power available to Sensor} \cong \int_{\lambda-\Delta\lambda}^{\lambda+\Delta\lambda} \epsilon_{\lambda,\theta} * E_b(\lambda, \theta, T) * C'$$

$$\textbf{Equation 4: } C' = C_{lens\ efficiency} * C_{aperture\ correction} * C_{exposure} * C_{gain} * C_{sensor\ efficiency}$$

2.2.2. Dual and Multi-Band Pyrometers

Dual and multi-band pyrometry is an alternative measurement technique which offers the benefit of reducing the need for careful calibration of emissivity and other scalar effects. Rather than relying on the measured radiation intensity directly, dual-band pyrometers filter the incoming radiation into two separate bands and use the intensity ratio to estimate the temperature. According to the approximation of Equation 5, taking the ratio of emission power causes emissivity and other scalar effects to be canceled out. The cancelation is complete under the assumption that the emissivity, bandwidth, and correction factors are the same at λ_1 and λ_2 . The ratio of radiation at narrow wavebands is illustrated in Figure 17.

$$\textbf{Equation 5: } \textit{Power Ratio at Sensor} \cong \frac{[\epsilon \cdot E]_{\lambda_1,\theta,T} * \Delta\lambda_1 * C'_1}{[\epsilon \cdot E]_{\lambda_2,\theta,T} * \Delta\lambda_2 * C'_2} \approx \frac{E_{\lambda_1}}{E_{\lambda_2}}$$

² C' represents several correction factors which account for the light-gathering efficiency of the camera system

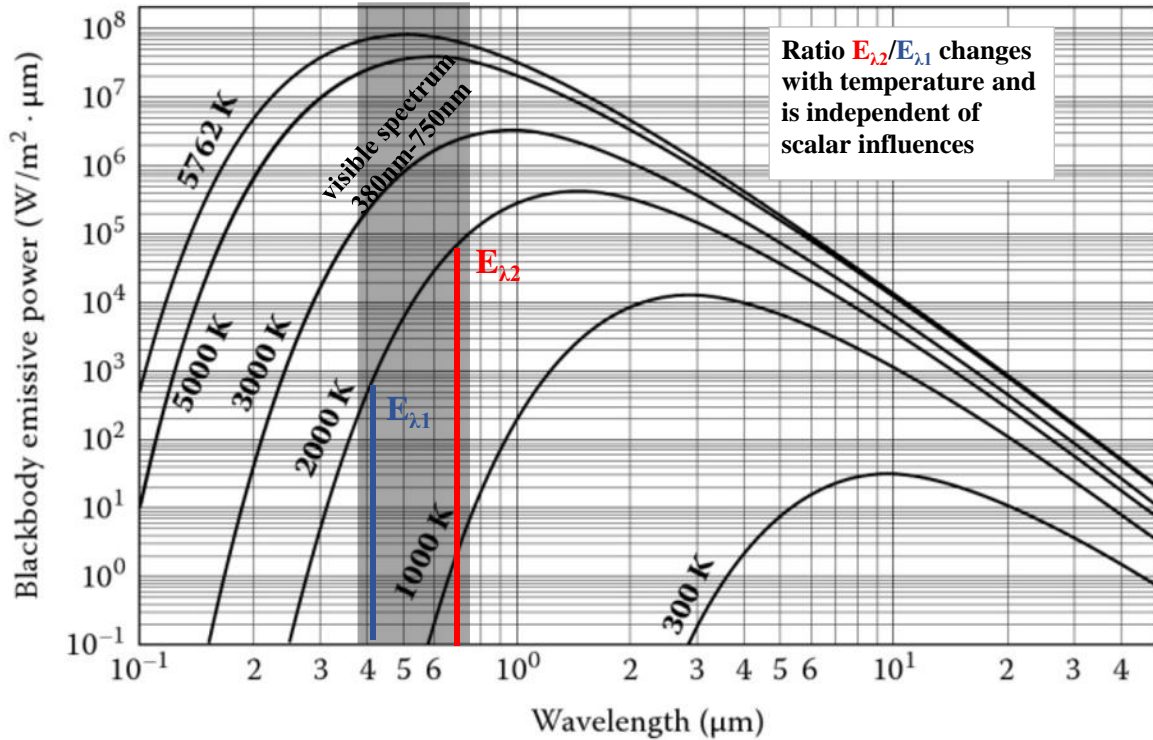


Figure 17: Correlation of radiation intensity ratio and temperature, modified from reference [25]

2.3. Additional Thermal Imaging Challenges

Although dual-band pyrometers can cancel out the scalar effects of emissivity, the cancellation is only guaranteed for the case of a black or grey-body radiation spectrum [27]. For example, consider an emission profile with pronounced spectral peaks. Since the emissivity of such a surface is not constant across all wavelengths, ϵ_{λ_1} and ϵ_{λ_2} may be significantly different depending on which λ_1 and λ_2 are chosen. If the ratio $\epsilon_{\lambda_1}/\epsilon_{\lambda_2}$ is not equal to 1, the radiant power ratio predicted by Equation 5 will be erroneous by a factor of $\epsilon_{\lambda_1}/\epsilon_{\lambda_2} - 1$. This source of error can be accounted for and corrected if the spectral emission profile of the material is known ahead of time. Unfortunately, useful sources of NIR spectral emission data for engineering alloys are difficult to find since the optical properties of the surface are largely influenced by the surface's topographical, chemical, or structural constitution [28]. In other words, the spectral emission is affected by practical factors such as surface roughness, oxidation, and microstructure.

Figure 18 illustrates the large effect that surface roughness conditions, such as polishing and shot blasting, and oxidation conditions can have on the normal total emission of stainless steels. Since the surface condition of the material can vary greatly depending on the application, it is unlikely that spectral emission data can be found for every surface condition encountered in practice. In order to overcome this obstacle, it is possible use an experimental calibration process in which the radiation from the actual material of interest is used to calibrate the thermal camera directly. By using the actual material and surface condition of interest as the calibration master, any effects from the surface structure, chemistry, and choice of filter wavelengths will be incorporated into the thermal calibration itself. The details behind the thermal calibration equipment and process will be discussed in Chapter 3: Camera Calibration Equipment.

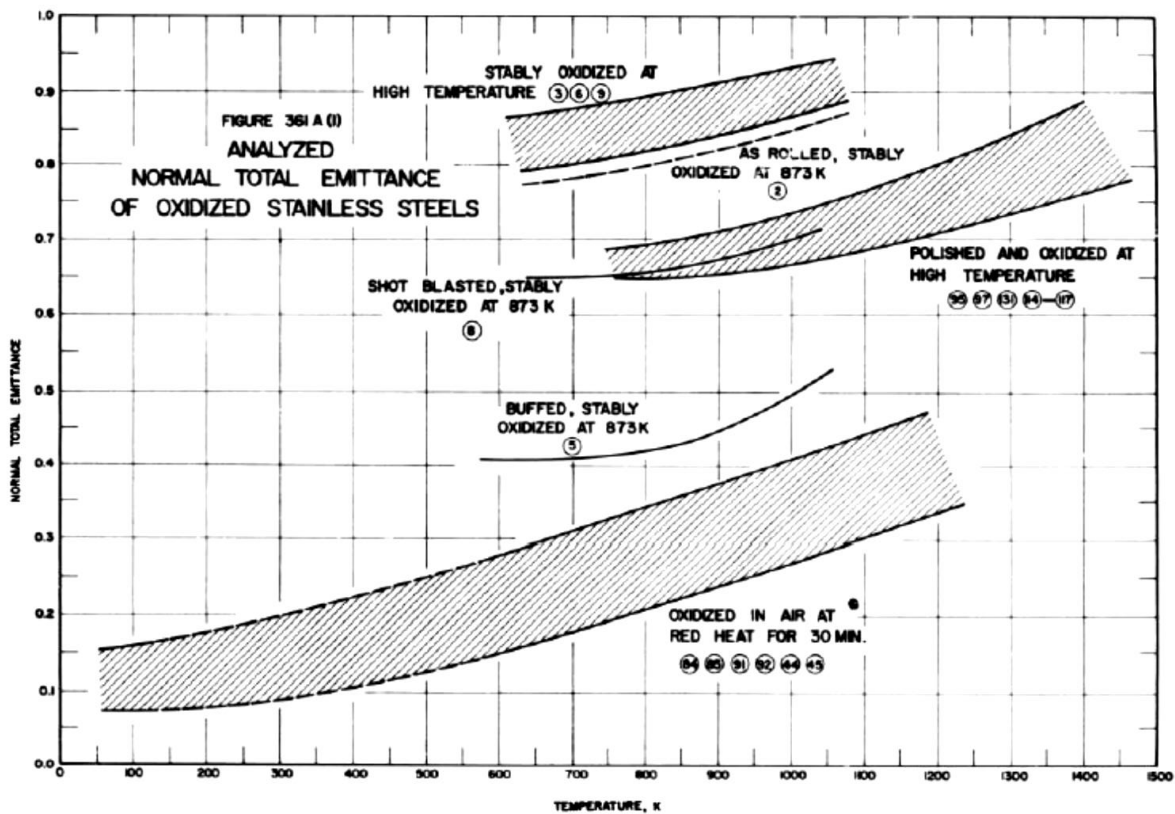


Figure 18: Normal total emittance of oxidized stainless steels with various surface conditions [28]

2.4. Camera Selection Factors for use as a Thermal Imaging Device

In addition to the thermal radiation theory and pyrometry techniques discussed thus far, it is also necessary to consider the factors involved in selecting a camera system which is suitable for being modified into a thermal imaging device.

2.4.1. Image Sensor Technology

Digital imaging sensors designed for operation in the visible spectrum are available in two main variants: charge coupled devices (CCD) and complementary metal oxide semiconductor (CMOS) sensors. Both CCD and CMOS sensors are based on doped silicon semiconductors which use the photoelectric effect to transduce incident photons into electron-hole pairs. A schematic representation of the photoelectric transduction process and the conversion of multiple analog signals into a digital image is included in Figure 19.

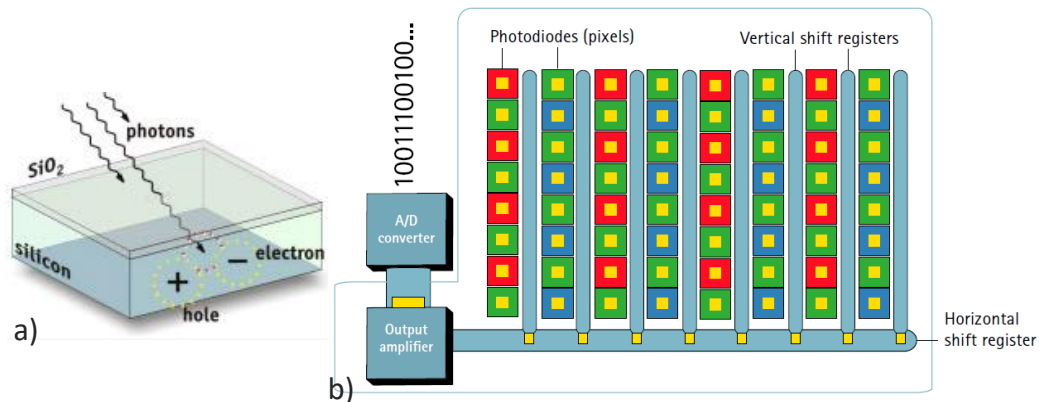


Figure 19: Photoelectric transduction by a semiconductor [29]; colour CCD sensor schematic [30]

Although CCD and CMOS image sensors are both semiconductors, the differences in the semiconductor's construction lead to significant differences in spectral response to long wavelengths. For example, the extinction depth for long wavelengths in silicon is often deeper than the doping depth for CMOS sensors, and as a result, long wavelengths will be ineffective at generating electron-hole pairs [29]. A low sensitivity to long wavelengths is beneficial for imaging at standard visible wavelengths since any signal from NIR sources will degrade the perceived image quality. Thermal imaging applications, however,

require the sensor to detect as much of the NIR energy as possible. Since CCD sensors have a much deeper doping depth, their ability to detect long wavelengths is better than CMOS sensors³ [29]. The Sony ICX618 CCD sensor is an example of a common sensor which is designed for standard imaging, yet has relatively good NIR sensitivity. The spectral sensitivity chart for this sensor is provided in Figure 20. Based on Figure 20, it can be seen that the sensor does have the capability to detect NIR wavelengths up to 1000 nm, however, the sensor's efficiency decreases significantly at longer wavelengths. As a result, from the camera's perspective, it is desirable to perform thermal imaging using shorter wavelengths.

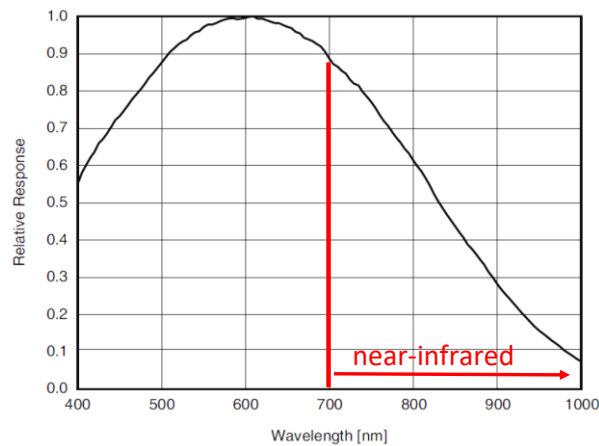


Figure 20: Spectral sensitivity of SONY ICX618 CCD sensor [31]

In addition to the spectral response of the semiconductor material, it is important to ensure that the sensor is manufactured as a greyscale sensor, and not a sensor designed for colour imaging. Sensors designed for colour imaging have a grid of dichroic filters such as the Bayer filter depicted in Figure 21. The grid of coloured filters allows each underlying pixel to focus on measuring one of the red, green, or blue components of the incident light's colour content. Since the green and blue filters remove the majority of red and NIR light, more than two thirds of the pixels on a colour-imaging sensor will be ineffective for thermal imaging. The consequence of the ineffective pixels on a thermal image is a checkerboard image, such as included in Figure 21.

³ Companies such as Teledyne DALSA offer specialized CCD sensors with enhanced near-infrared sensitivity

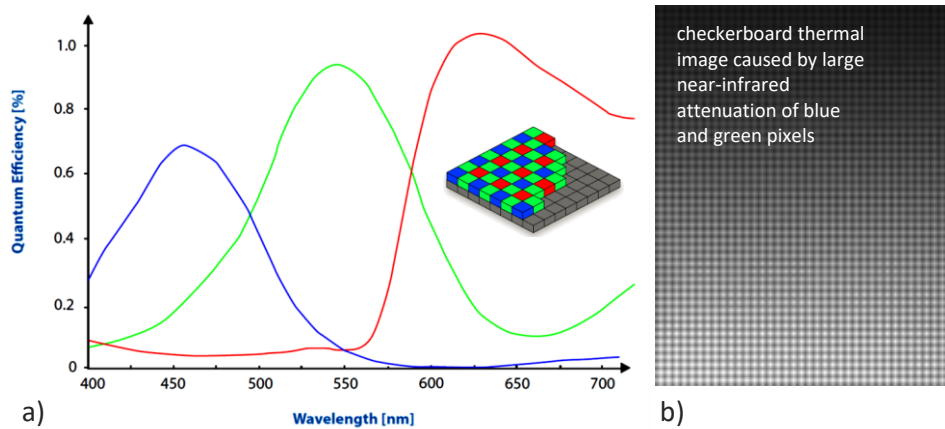


Figure 21: a) Combined spectral sensitivity of Sony ICX618 with colour Bayer filter [32];
b) Thermal image taken using Bayer filtered sensor

2.4.2. Lenses and Filters for Near-Infrared Imaging

In addition to the NIR performance of the sensor itself, the other components in the camera system, such as the lenses and filters, should also have good NIR properties. Since most CCD cameras are designed for standard visible light imaging, they often come with an IR reduction low-pass filter. Such a filter will greatly diminish the capabilities of the CCD sensor as a thermal imaging device. The spectral transparency of an IR filter from a standard imaging camera is provided in Figure 22. When selecting a camera for a thermal imaging application, it is important to ensure that the camera housing is manufactured without a built in infrared (IR) reduction filter; or at least has one that can be easily removed.

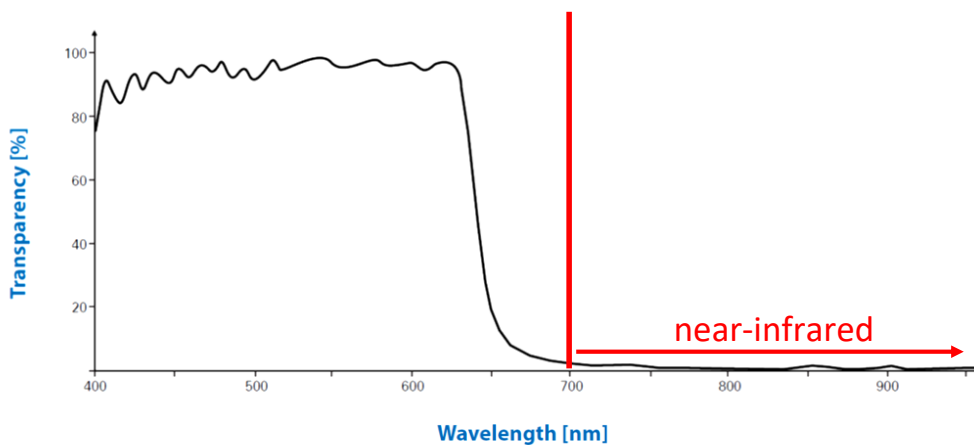


Figure 22: Spectral transparency of an IR reduction filter from a CCD camera [32]

Another important factor for a thermal imaging system is the optics that are used to focus the diffuse radiant light into a clear image at the sensor array. A standard optical lens will not be a good choice for a thermal imaging application since the anti-reflective coatings on the lens elements are not designed to operate with NIR wavelengths. Anti-reflective coatings are used to reduce the reflectivity of the lens surfaces, which in turn improves transmissivity and reduces ghost images from internal lens surface reflections [33]. For this project, all lenses used Edmund Optics' VIS-NIR™ lens coating. The permissible spectral imaging range of the VIS-NIR™ coating as well as other anti-reflection coatings are provided in Figure 23.

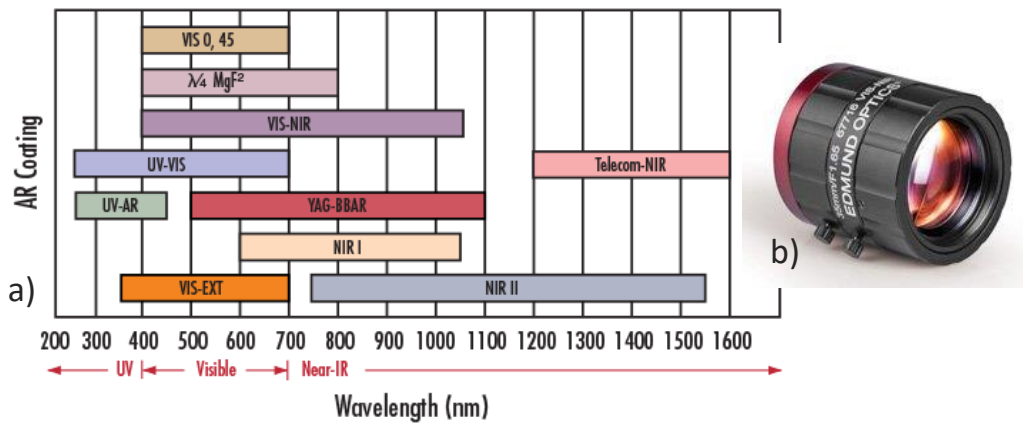


Figure 23: a) Edmund Optics anti-reflective coating spectral range; b) Edmund Optics 67-716 VIS-NIR lens [33]

2.4.3. Connectivity and Control Software

Another factor to consider when choosing a camera system for thermal imaging is the availability of control software for the camera. Since commonly available camera systems are not originally designed to be thermal imaging devices, it is expected that some customized control over the camera will be needed. As a result, it is beneficial to choose a camera system which is supplied with a software library that allows the camera to be controlled by computer. For this project, the DMK-23U618 monochromatic CCD industrial camera designed by The Imaging Source [34] has been selected. This camera is based on the Sony ICX618 sensor and supports 8-bit images; which means that the greyscale pixel value can be any value from 0 to 255. Since this is an industrial camera, it is provided with a software development kit

called Imaging Control 3.4™, which is compatible with the Microsoft Visual Basic.Net™ framework. The software development kit includes many useful functions and libraries for customizing the camera system's operation, such as low level access to the camera's pixel buffers as well as high level features such as built in real-time video display.



Figure 24: DMK 23U618 camera which includes Imaging Control 3.4 software development kit

2.5. Sensor-Compensated Model of Dual-Band Pyrometry of a Blackbody

By combining the thermal radiation theory for a blackbody with the spectral response of the camera selected for this project, it is possible to model the ideal response of the system as a dual-band pyrometer. Although the simplified model developed here is based on the ideal scenario of blackbody radiation and a noise-free sensor, it is sufficient to provide insights into the general performance characteristics of the camera as a thermal imaging device. In order to model the combined spectral response of the system, the spectral blackbody emissive power was first calculated for several temperatures of interest to welding applications. The results of the blackbody spectral emissive power calculations are plotted in Figure 25, and indicate that the peak emission power for the temperatures of interest occur at wavelengths that are longer than the NIR range of the CCD sensor. As a result, the CCD based thermal imaging system will have the most available incident radiation to form a signal when operating with its longest available wavelength of 1000nm. However, recall that the spectral sensitivity of the ICX618 sensor, provided in Figure 26, degrades rapidly for wavelengths longer than 700nm. As a result, it is expected that the actual peak sensitivity will occur at some intermediate wavelength between 700nm and 1000nm.

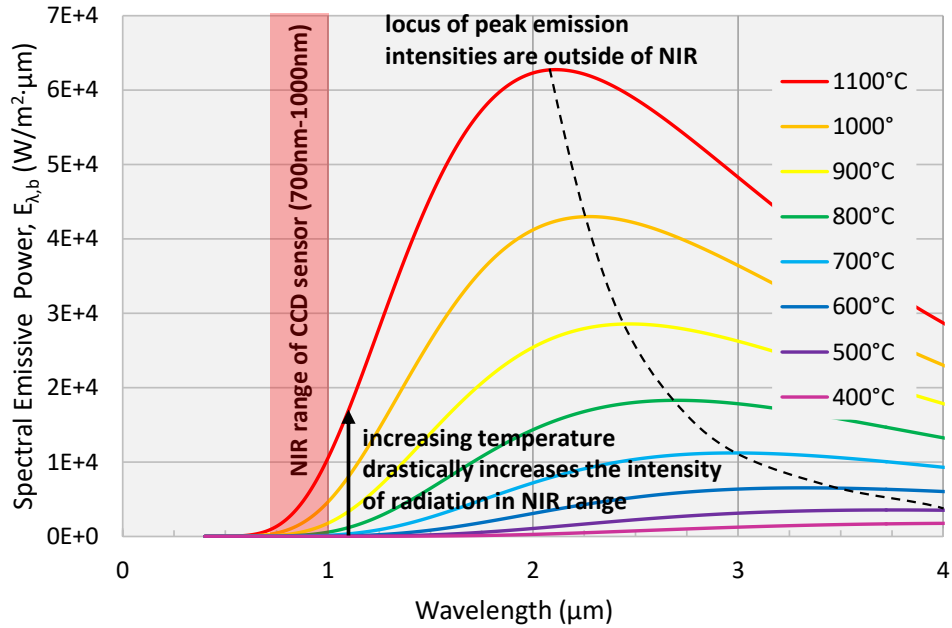


Figure 25: Blackbody spectral responses for temperatures of interest

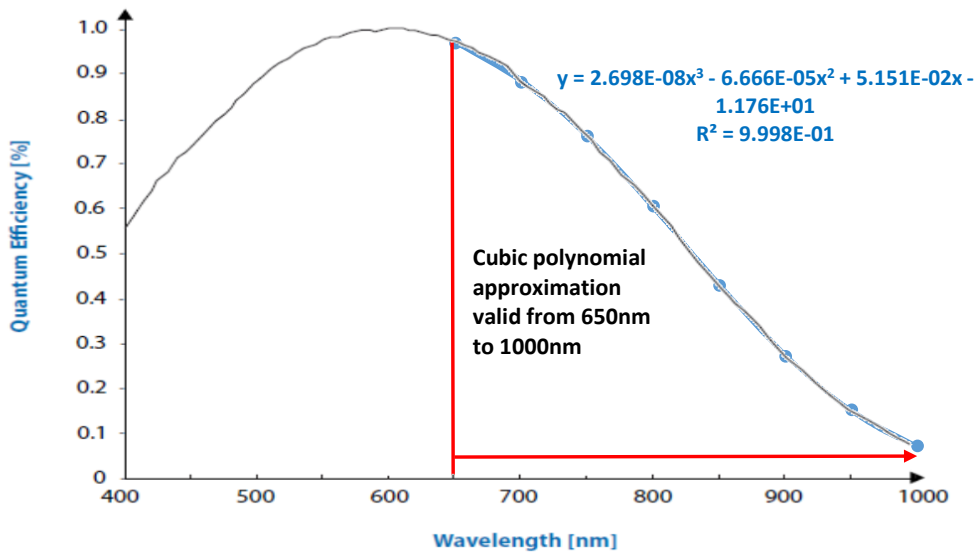


Figure 26: Polynomial approximation of Sony ICX618 sensor spectral sensitivity, modified from [31]

In order to solve for the actual response of the camera to blackbody radiation, it is necessary to correct for the spectral efficiency of the sensor. The sensor's spectral efficiency was approximated using data from the manufacturer's graphical spectral efficiency curve and a least-squares third order polynomial regression applied to the region of 650nm to 1000nm. The cubic polynomial curve overlaid with the original graphical data is included in Figure 26. Equation 6, which multiplies the blackbody

emission by the sensor efficiency for across a spectrum of wavelengths, was used to model the sensor-compensated blackbody response.

Equation 6: $Sensor\ Signal_{blackbody}(\lambda, T) \cong E_{\lambda,blackbody}(\lambda, T) \times Sensor\ Efficiency(\lambda)$

The results of the model based on Equation 6 are included in Figure 27, and several important observations can be drawn. Firstly, the competing factors of improved radiation at long wavelengths and improved sensor efficiency at short wavelengths do indeed cause the peak signal intensity to occur between 850nm and 1000nm for the temperature range of interest. In addition, increasing the surface temperature shifts the peak signal intensity towards shorter wavelengths. Furthermore, there is a massive range in signal intensity from 400 to 1100°C.

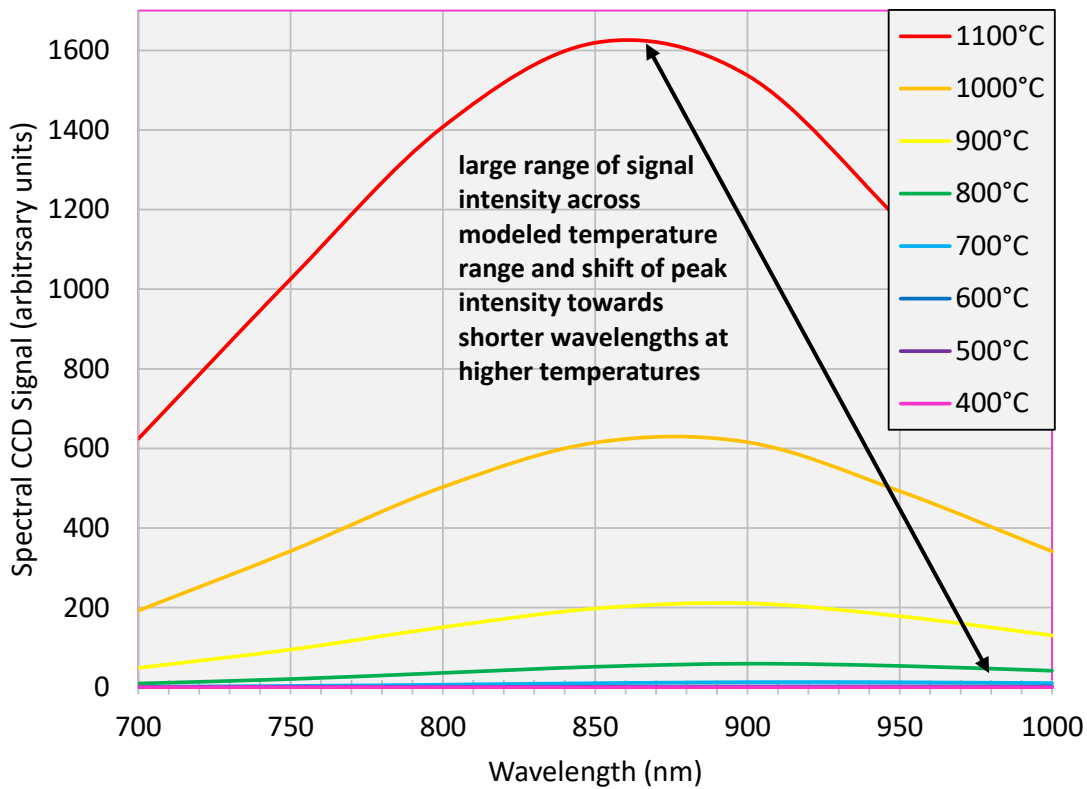


Figure 27: Spectrally corrected CCD response to blackbody radiation

Since the range of intensities detected by the sensor is so large, a second plot which uses a logarithmic scale has been provided in Figure 28. In addition, the peak signal intensities and the signal

intensity ratio between adjacent temperatures have been provided in Table 1. According to Figure 28 and Table 1, the signal intensity at 1100°C is 112975 times greater than the signal intensity at 400°C. Since the camera is an 8-bit camera and is only capable of detecting 256 equally spaced radiation levels, it is clear that the thermal measurement range of the camera will not be able to detect all temperatures within the modeled range with a great deal of precision.

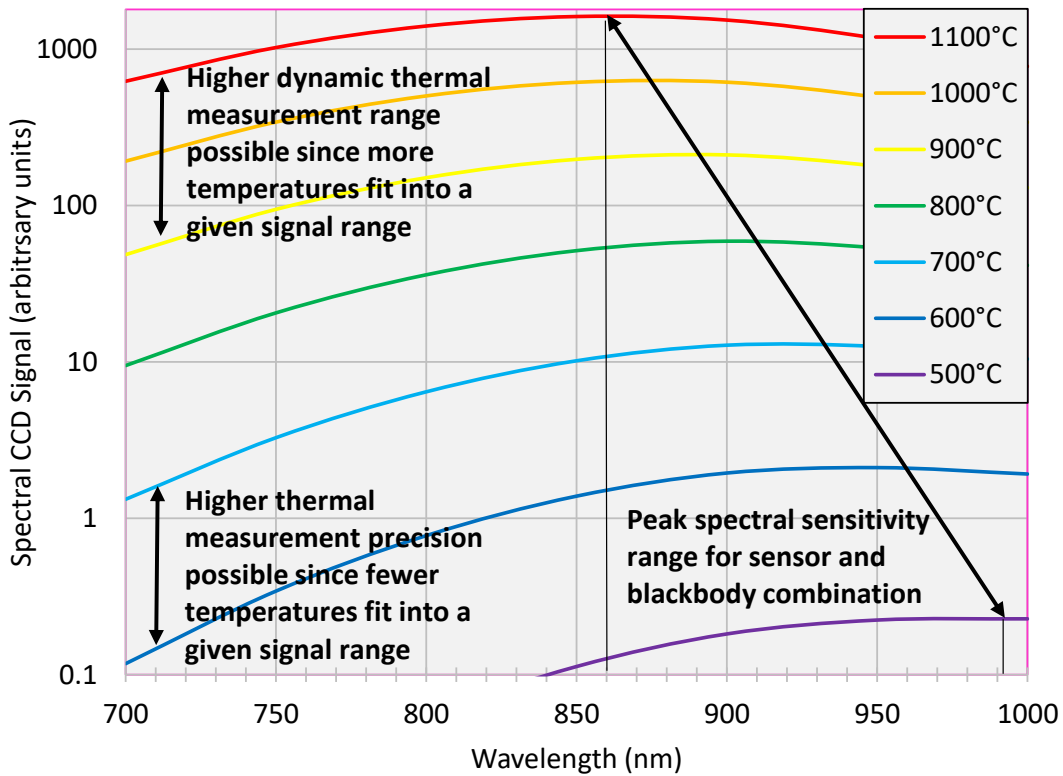


Figure 28: Spectrally corrected CCD response with logarithmic scale

Table 1: Peak signal intensities and adjacent ratios

Temperature (°C)	400	500	600	700	800	900	1000	1100
Peak CCD Signal Intensity, P (arbitrary units)	0.014	0.228	2.112	12.8	59.2	211.0	615.7	1619.2
Signal Intensity Ratio		15.9	9.3	6.1	4.6	3.6	2.9	2.6
		P500/P400	P600/P500	P700/P600	P800/P700	P900/P800	P1000/P900	P1100/P1000
		112975						
		P1100/P400						

Since the dynamic range of the thermal radiation intensity is far larger than the dynamic range of the imaging sensor, it will be necessary to choose a compromised configuration for the thermal camera which focusses on performing measurements across a narrower measurement range. As with all compromises, different performance trade-offs will manifest themselves depending on which temperature range the system is optimized for. According to Table 1, if the camera is configured to detect low temperatures, an incremental increase in temperature will lead to a large change in signal intensity. For example, the signal intensity for 500°C is 15.9 times greater than the signal at 400. Since the camera has a fixed dynamic range of 256 values, the camera will go from no signal to a fully saturated signal with only a small change in temperature. As a result, a camera tuned for detecting low temperatures will have good thermal resolution but poor thermal measurement range. In contrast, if the camera system is configured to measure higher temperatures, an incremental increase in temperature will lead to a relatively small change in signal intensity. For example, the signal intensity for 1100°C is only 2.6 times as large as the signal at 1000°C. As a result, the camera will have an increased thermal measurement range and a decreased thermal resolution when configured to measure high temperatures.

So far, the intensity of radiation detected by the sensor has been investigated, however, recall that a dual-wavelength pyrometer does not rely on signal intensity alone; it relies on the signal intensity ratio of two separate wavelengths. As a result, the modeling of various filter ratio choices is also beneficial. The modeled correlation between the temperature and camera intensity ratio for several NIR filter combinations is included in Figure 29. Based on the Figure 29, several generalizations for the given NIR range and temperature range can be made. Firstly, choosing bandpass filters which are farther apart in their central wavelength will cause a greater ratio in signal intensity as well as a steeper gradient of signal ratio, R , with respect to temperature, T , or $\frac{dR}{dT}$. For example, the curve for 950nm/800nm has the

largest wavelength difference of the given scenarios (150nm), and it also has the greatest intensity ratio and the steepest slope.

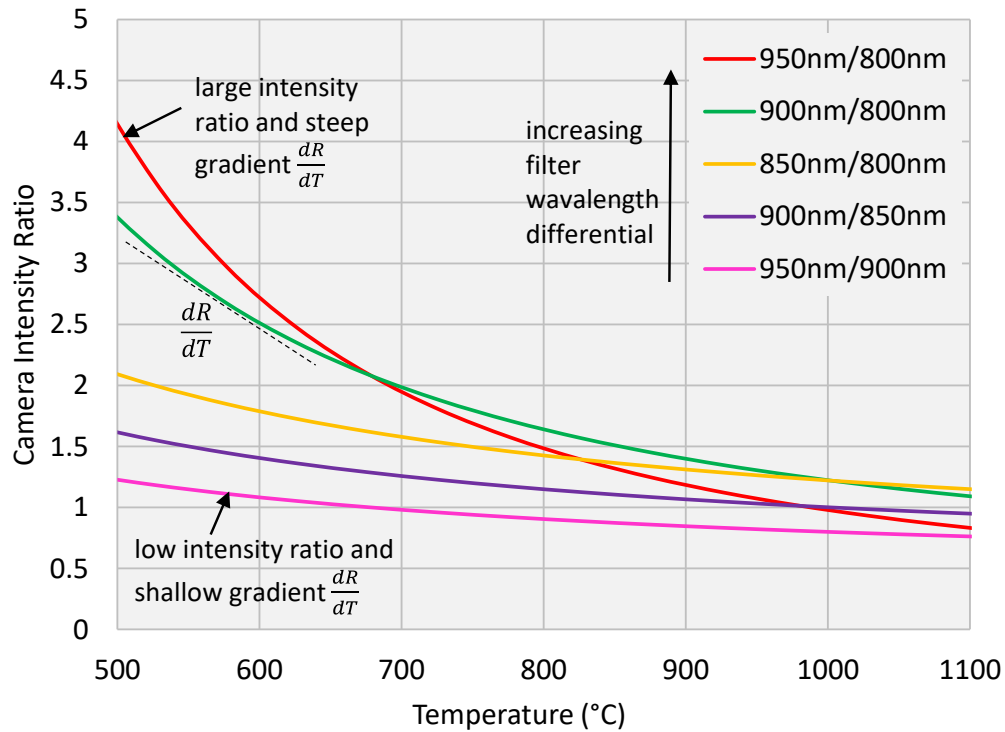


Figure 29: Theoretical sensor intensity of bandpass filter ratios for blackbody radiation

A steep slope for the intensity ratio vs temperature relationship is beneficial for temperature measurement resolution, since an incremental change in temperature corresponds to an easily detectable steep change in camera signal, however, a large intensity ratio will also reduce the dynamic thermal measurement range of the system. For example, if the radiation at λ_1 is much brighter than the radiation at λ_2 , the pixels measuring at λ_1 will saturate at their peak measurement intensity while the pixels measuring at λ_2 will not have used all of their potential range. Similarly, the pixels measuring at λ_1 will be detecting signal for a certain temperature range while pixels measuring at λ_2 are still operating below their least significant bit of resolution. Since a valid signal is necessary at both imaging wavelengths in order to estimate temperature, any temperatures where the valid pixel intensities do not overlap represents lost thermal measurement range. Figure 30 and Figure 31 illustrate how the choice of bandpass filter

wavelengths λ_1 and λ_2 will affect the amount of potential temperature measurement range. A larger difference between the filter wavelengths will increase the lost range and decrease the useful range. It should also be noted that signal noise will be likely be a problem at the lower temperature end of the measurement range since a single bit of noise will significantly alter the signal ratio.

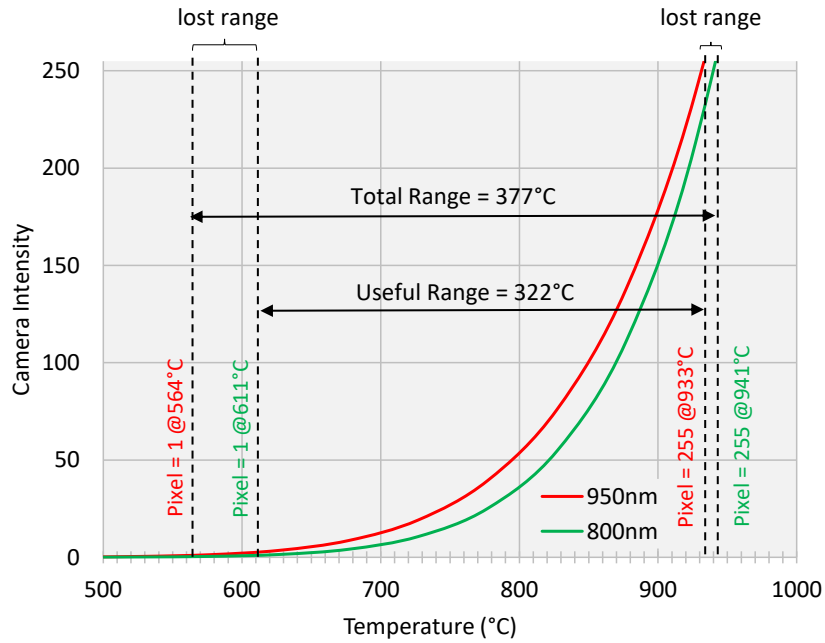


Figure 30: Thermal measurement range for filters separated by 150nm

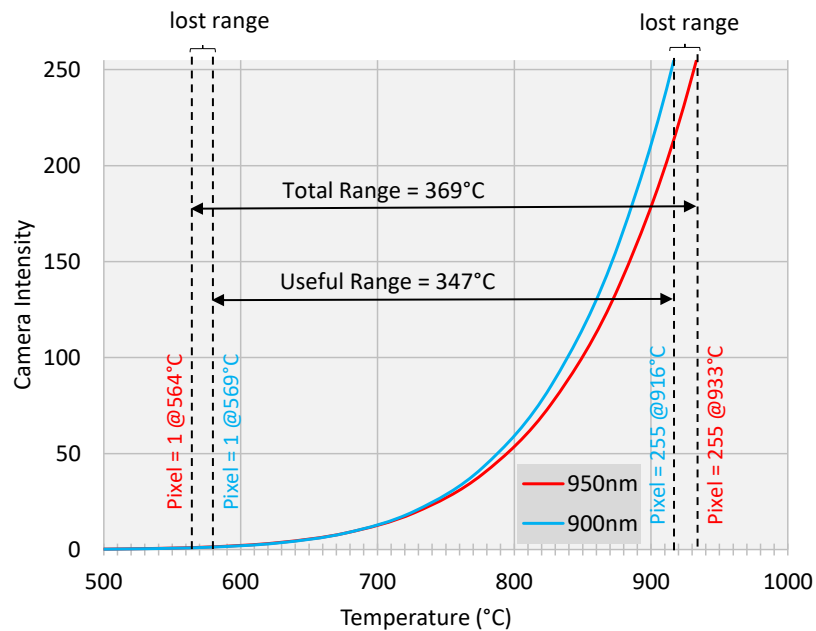


Figure 31: Thermal measurement range for filters separated by 50nm

Chapter 3: Camera Calibration Equipment

So far, this report has discussed several factors involved in the design and performance of a CCD-based thermal imaging system, however, the task of actually building and calibrating such a system still remains. A significant effort was devoted to the development of the equipment required to calibrate the thermal imaging system. The purpose of this chapter is to discuss the basics behind the design, operation, and testing of the specialized calibration equipment which was required for this project.

3.1. Camera Calibration Test Chamber

As discussed in Chapter 2: Thermal Imaging Theory, there are a variety of ways in which the radiation from an actual surface may differ from that of a blackbody. The effects of parameters such as surface roughness, oxidation, and perspective angle can alter the radiation characteristics significantly. Since the exact effects of these parameters are not well known at this time, it is desirable to calibrate and test the thermal imaging cameras in a controlled environment where as many factors as possible can be controlled. A schematic diagram of the test chamber which has been developed for this project is included in Figure 32, and detailed dimensional drawings of the test chamber are included in Appendix A: Camera Calibration Chamber Dimensional Drawings. The camera calibration test chamber allows for a small metallic specimen, which is made with the desired material and surface preparation, to be mounted between the pair of copper electrodes. The purpose of the copper electrodes is to supply large amounts of current to the specimen and create resistive heating. The electrodes are electrically insulated from the walls of the chamber through polymer insulation rings and are liquid cooled to avoid overheating of the polymer insulation. The angle of the test specimen with respect to the cameras is adjustable by $\pm 90^\circ$ from normal through a tilting stage, and the axis of rotation of the tilting stage is along the same plane as the top surface of the test specimen so that angular adjustments do not move the sample with respect to the focal plane of the cameras. A pair of closely spaced cameras is used to perform imaging at the two

wavelengths required for dual-band pyrometry without the need for a complicated beam-splitter arrangement. Finally, the chamber provides argon inlet ports so that the high temperature testing can be conducted in an inert atmosphere to prevent oxidation. It should be noted that although the chamber appears translucent in Figure 32, in actuality, it is constructed out of aluminum and is opaque to isolate the heated specimen from external light sources.

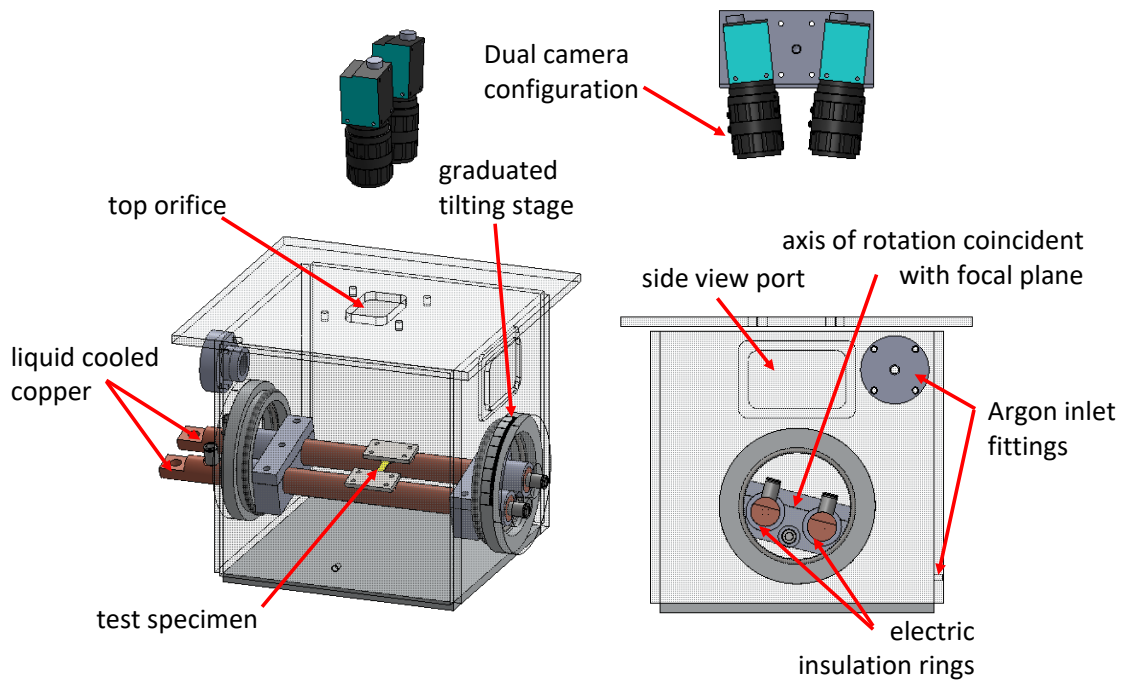


Figure 32: Camera calibration test chamber schematic

3.2. Temperature Control System

In order to calibrate the thermal camera system in a way that accounts for any spectral emissivity inhomogeneity, it is necessary to use the material of interest as the calibration master. By simultaneously measuring the temperature of the surface as well as the thermal radiation arriving at the camera, a direct correlation between temperature and radiation can be determined regardless of emissivity peaks. As a result, it is necessary to have a means of accurately measuring and controlling the temperature of the test sample up to very high temperatures. The method of measuring and controlling the surface temperature which has been implemented in this project involves using a closed loop control system which is

summarized in Figure 33. The temperature control system has been implemented by using a thermocouple to measure the temperature of the specimen and a computer controlled welding power supply to control the temperature of the specimen by adjusting the electric current flowing through it.

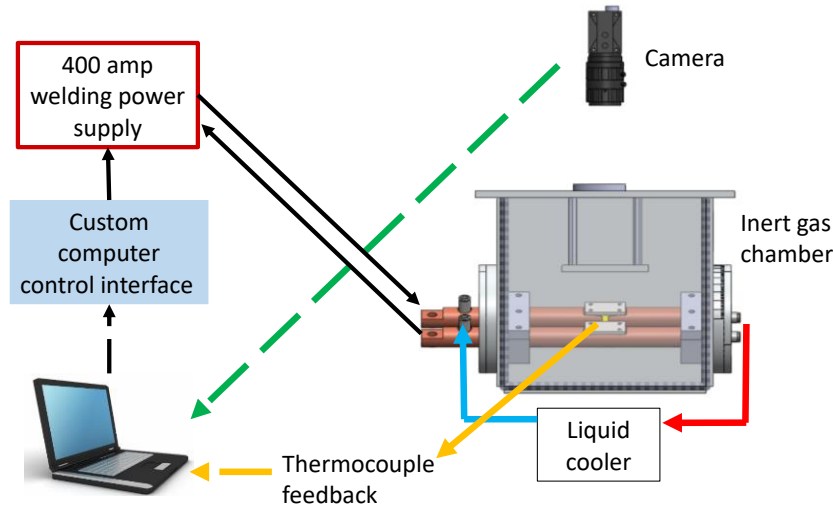


Figure 33: Schematic of closed loop temperature control system

3.2.1. Thermocouple Selection and Implementation

The temperature feedback required to control and calibrate the thermal cameras is achieved by a thermocouple junction welded directly to the surface of the test specimen. As illustrated in Figure 34, the thermocouples are placed a small distance apart from each other and aligned so that they lie upon the same isotherm. Leaving a gap between the thermocouples allows the average intensities of a long and narrow region of isothermal pixels between the thermocouples to be used for the calibration.

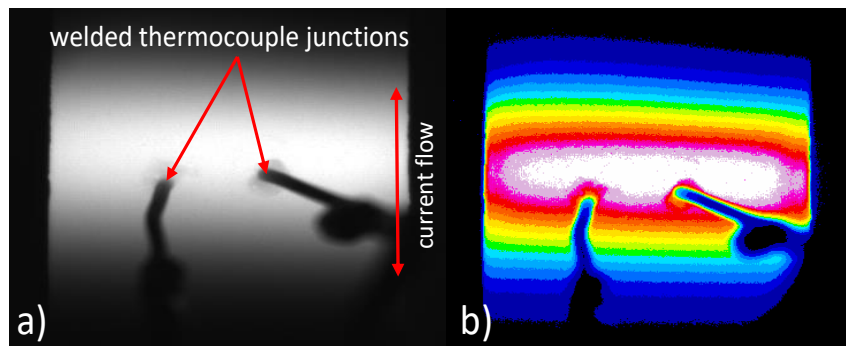


Figure 34: a) Single-band thermal image showing welded thermocouple junctions; b) Isotherms visualized by colour map

Although common K-type thermocouples are rated to operate between 0°C and 1260°C [35], there are several sources of inaccuracy that can affect K-type thermocouples when operating at high temperatures. A summary of the high temperature effects on K-type thermocouples is included in Table 2. In order to overcome the issues listed in Table 2, N-type thermocouples were used since they are specifically designed to reduce the high temperature stability issues faced by K-type thermocouples.

Table 2: K-type thermocouple issues reported for high temperature applications [36], [37]

K-type Thermocouple: High Temperature Issue	Description
Short range ordering	From 425°C to 550°C, nickel and chromium atoms in the chromel leg tend to form an ordered crystalline structure
Cumulative Drift	Above 900°C, cumulative drift occurs due to preferential oxidation of the chromel leg. The composition of the wire allows for internal and external oxidation
Hysteresis	Cycling above and below 980°C causes crystalline changes which permanently change the Seebeck coefficient function

Since the temperature measured by the thermocouple will correspond to the temperature of the location where it is welded to the sample, it is important that presence of the thermocouple itself does not significantly alter the local surface temperature. Any heat being conducted away from the surface by the thermocouple wire will decrease the local surface temperature and thermocouple measurement. In order to limit the thermal conduction through the thermocouple wire, the wire diameter was chosen to be as fine as possible while still being durable enough for this application. For this project, the thermocouple wire size which was chosen was 0.255mm in diameter, or #30 American wire gauge (AWG). Finally, the device used to measure and record the thermocouple's temperature was National Instruments' 9211 thermocouple measurement module with built in cold-junction compensation.

3.2.2. Ohmic Offset Errors

Since thermocouples transduce temperature into a voltage signal through the Seebeck effect, any external source of voltage applied across the thermocouple wires will also be detected by the sensing electronics and degrade the accuracy of the temperature measurement. As a result, care must be taken to avoid interference from the electrical resistance heating of the test specimen. For example, consider the simplified electrical equivalent circuit for the resistively heated test specimen shown in Figure 35. Note that the thermocouples are welded directly onto the specimen and are electrically connected.

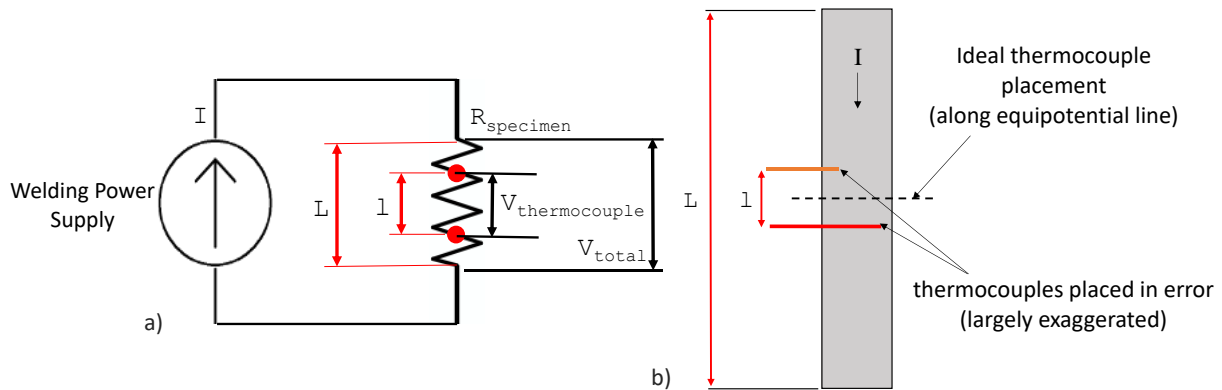


Figure 35: a) Circuit diagram of Joule heated specimen; b) Thermocouple placement error with respect to equipotential line

According to Equation 7: Ohm's law, in order for current to pass through the test specimen, a voltage must exist across the specimen which is proportional to the product of the current and resistance.

Equation 7: *Ohm's Law: Voltage = Current × Resistance = $I \times R$*

In an ideal scenario, the thermocouples would be placed at electrically equipotential locations that are the exact same distance along the length of the sample. In reality, a small error in thermocouple placement will always be present. According to Equation 8, the electrical resistance of the sample is a function of the material's inherent resistivity, length, and cross sectional area.

Equation 8: *Resistance = $\frac{\text{resistivity} \times \text{length}}{\text{area}} = \frac{\rho L}{A}$*

Assuming that the resistivity and cross section of the sample are uniform along the whole conduction length L , the voltage will drop across the resistive specimen in a linear fashion. As a result, the Ohmic voltage bias applied to the longitudinally separated thermocouple probes will be proportional to the total voltage drop and the junction separation distance according to the length ratio given in Equation 9.

$$\text{Equation 9: } V_{thermocouple} = V_{total} \frac{l}{L}$$

Since the Seebeck voltages produced by the thermocouple are in the tens of millivolts range, and since the electric currents required to heat up the given specimen are in the hundreds of amps range, it is expected that large thermal measurement errors may be generated if the longitudinal separation of the thermocouple wires is not carefully controlled. In order to test the level of error caused by Ohmic voltage bias, an experimental specimen was prepared as shown in Figure 36. Two pairs of thermocouples were welded to this sample with exaggerated separation along the length of the specimen in order to amplify the Ohmic offset voltage error.

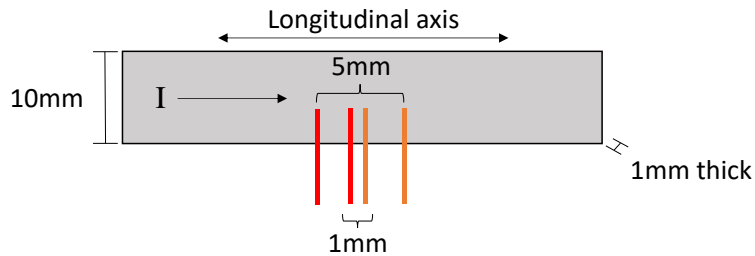


Figure 36: Thermocouple locations of Ohmic offset voltage test specimen

The specimen was mounted in the test chamber and temperature measurements were taken with zero current flow as well as a low current of 10 amperes (A). The temperature measurements taken with no current applied should be the most accurate since the effects of Ohmic offset voltage are eliminated. The low current of 10A was chosen so that the resistive heating of the specimen will be limited to less than 1°C. As a result, any difference between the no current and 10A conditions should be largely attributable to Ohmic offset error. The results of the Ohmic offset error experiment are shown in Figure 37.

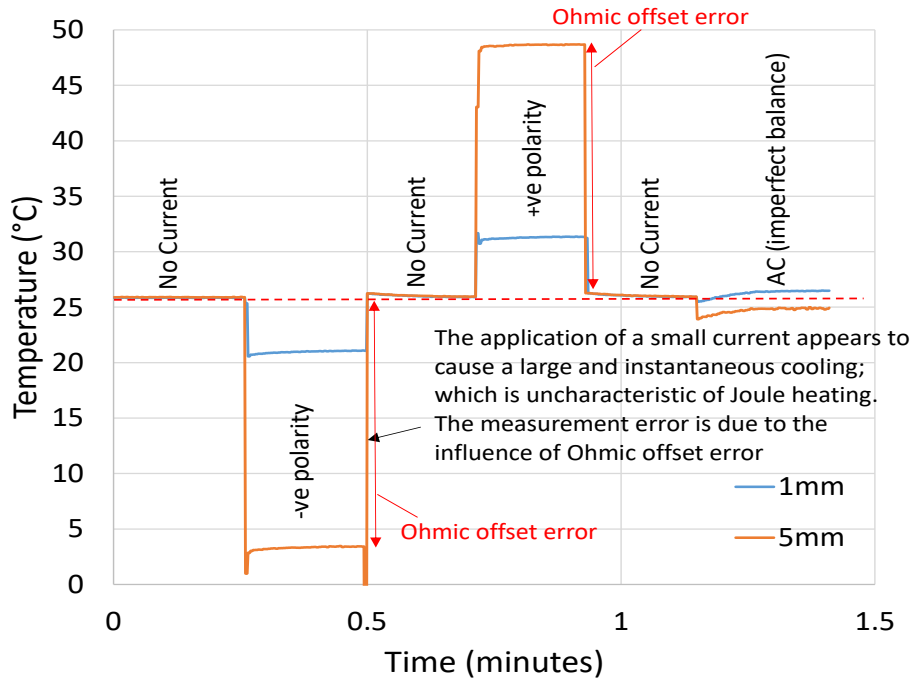


Figure 37: Ohmic offset error experiment results

According to Figure 37, the ambient temperature of the room, which is marked by the red dashed line, was roughly 26°C and 10A of direct current (DC) caused sizeable thermal measurement errors. Although the errors resulting from positive and negative DC current are large, they appear to be equally and oppositely biased. As a result, the Ohmic offset error can be reduced if an equal amount of time is spent at opposite current polarities within a given thermocouple measurement sample. Figure 38 a) illustrates how a constant alternating current (AC) with a balanced duty cycle and a wave period which is an integer multiple of the thermocouple sampling period can be used to nullify the effects of Ohmic offset error.

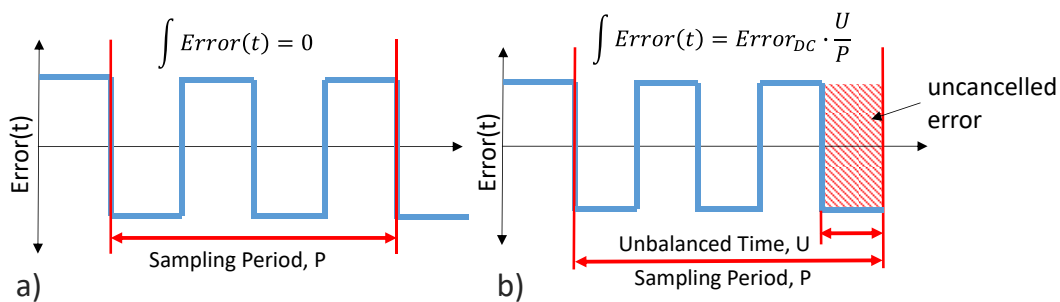


Figure 38: a) Complete error cancellation using AC current; b) Incomplete error cancellation

The welding machine which is being used to supply the current is capable of producing square wave AC current, however, the frequency and duty cycle is controlled through low precision potentiometer dials. As a result, it is difficult to set the AC frequency and duty cycle to exact values. In order to overcome this issue, the frequency of AC current was increased to be very fast in comparison to the sampling time. If the AC frequency is much faster than the sampling frequency, a lack of precision or drift in the frequencies over time can lead to a worst case scenario, illustrated in Figure 38 b), where a single half-cycle of the AC current is measured without being cancelled. Increasing the AC frequency will shorten the period of the AC cycle, and as a result, the non-cancelled half cycle will spend a proportionally less amount of time contributing to Ohmic offset errors. In addition, if the AC and sampling frequencies are not exact integer multiples of each other, the influence of Ohmic offset error will drift in and out of phase and cause harmonic interference, however, the magnitude of this interference can also be reduced by increasing the AC frequency. Figure 39 includes experimental results which show that increasing the frequency of alternating current reduces the total error resulting from this type of harmonic resonance.

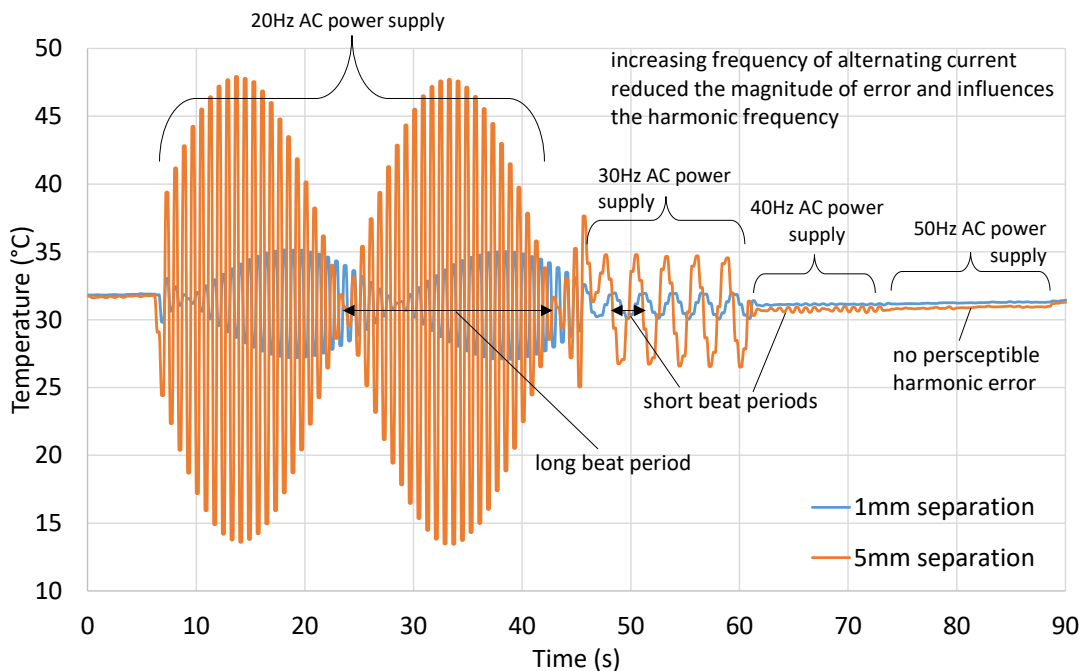


Figure 39: Ohmic offset error sampling harmonics (1Hz sampling rate)

In order to minimize the effects of Ohmic offset errors, it is also necessary to ensure that the AC duty-cycle is completely balanced. Once again, the control panel of the welding power supply did not provide a reliable readout for this parameter. As a result, the duty cycle of the power supply was balanced experimentally by comparing the two thermocouple channels. Recall that the test specimen prepared for the study of Ohmic offset error contains two pairs of thermocouple channels with separations of 1mm and 5mm. If a low current is driven through the sample, so that no significant temperature gradient exists along the sample, the two thermocouple channels should report the same temperature. Although the two thermocouple channels will experience the same temperature, the channel with a further separation will be more susceptible to Ohmic offset error. Therefore, if the AC duty cycle is adjusted until the two channels report the same temperature value, the effect of Ohmic offset error must be zero and the duty cycle must be balanced. Figure 40 shows that the experimental balancing of the AC duty cycle could reduce the total Ohmic offset error to roughly 0.26°C when using an AC frequency of 60Hz, a sampling rate of 1Hz.

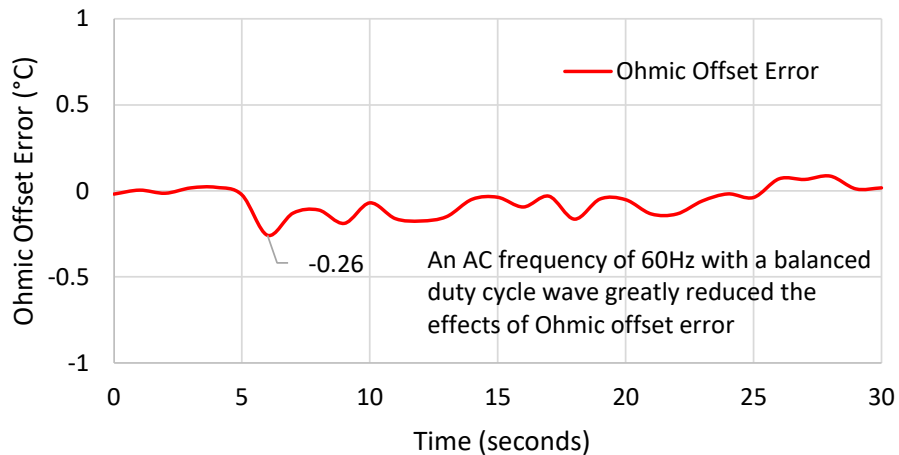


Figure 40: Ohmic offset error after AC duty cycle balancing procedure (60Hz AC, 1Hz sampling, 10A)

3.2.3. PID Tuning & Ramp Tracking Tests

With the calibration system now capable of accurately measuring the surface temperature with thermocouples, it is possible to use the temperature information as feedback for a closed loop control system. An automatic control system is desirable since it will allow the thermal history of the sample to be programmed at will. For example, maintaining the surface at an elevated temperature for a given time or ramping temperatures up or down at a controlled rate are just some of the possible ways that a closed loop control system can improve the capabilities of the calibration equipment. A discrete time equivalent to a proportional-integrative-differential (PID) controller was implemented at a sampling rate of 2 Hz. Due to the relatively slow sampling rate, it was necessary to tune the system in a conservative manner to avoid instability. The control system was tuned manually using step response and ramp tracking tests until satisfactory results were achieved. Figure 41 illustrates the step and ramp tracking responses of the tuned system to be more than sufficient for the camera calibration application.

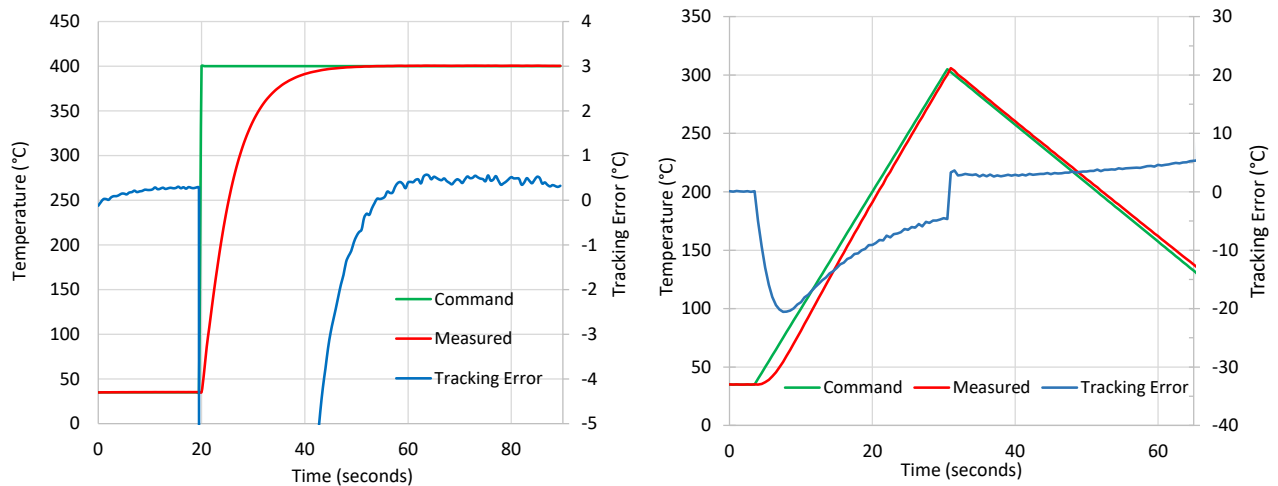


Figure 41: a) Step tracking response; b) Ramp tracking response

3.3. Dual Camera Spatial Calibration

In order to maximize the radiation reaching the camera sensors and avoid the added complexity of using a beam splitter, a dual camera imaging system has been developed based on two fully independent cameras. In order to keep the sample within the field of view of both cameras, the cameras have been tilted at the 6° angle illustrated in Figure 42. By tilting the cameras at an angle with respect to the surface they are imaging, the spatial information of one of the surface axes will be compressed into a slightly reduced number of pixels, however, the level of spatial compression caused by a 6° angle is only about 5%. In addition, since the cameras are both tilted by the same angle, the spatial compression will be the same for both images. As a result, it is still possible to map the pixels directly from one camera to another as will be required when thermal imaging and taking pixel intensity ratios.

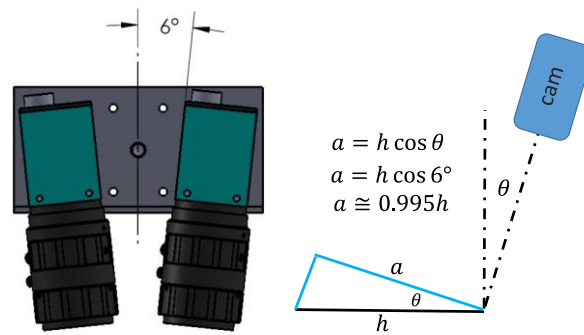


Figure 42: Camera tilt angle and X-axis spatial compression factor

In order to check the alignment of the cameras, a special specimen was prepared with a grid pattern scribed onto the surface. By comparing the central location and alignment of the grid pattern between both cameras, it is possible to check for misalignment of the cameras due to manufacturing and installation errors. Figure 43 includes images taken from Camera A and Camera B and it is evident that there is a slight mismatch between the images. Although there is a slight mismatch between images, the mismatch can be easily measured and corrected for by shifting the pixel values in software by ΔX and ΔY .

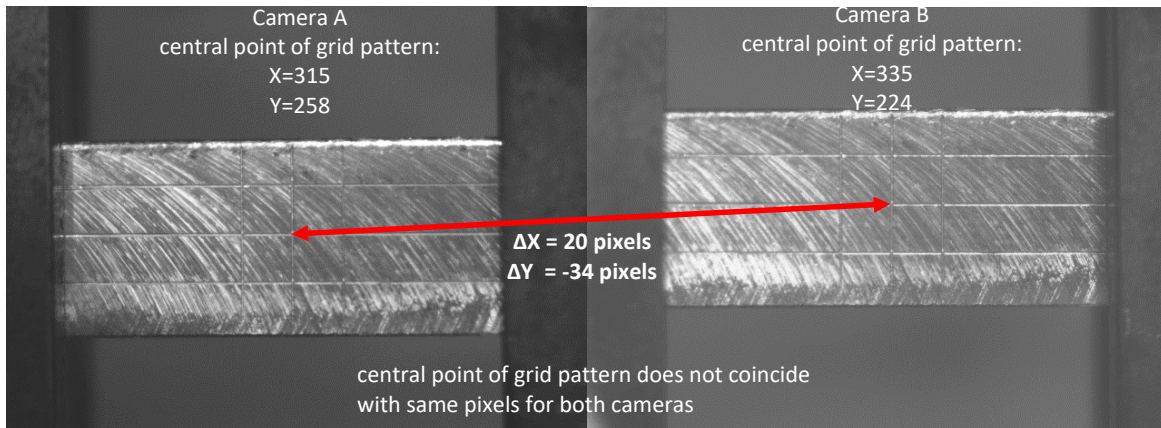


Figure 43: Spatial mismatch between camera A and camera B

3.4. Measurement System Synchronization

In order to combine the thermocouple measurement and dual camera measurement into a single system, a significant effort in software development was required. Using a combination of Microsoft VisualStudio and National Instruments LabView, full control over both cameras and the temperature control system was integrated into a graphical user interface (GUI). The GUI provides real-time video display from both cameras as well as thermocouple control and data logging. In addition, the camera exposure and thermocouple sampling times are synchronized to occur based on the rising edge of a shared pulse generator. Although discussions of all the details behind the software features and functionality will not be included in this report, the front panels of the GUI are shown in Figure 45 and the program code can be found in Appendix B: LabView Thermal Measurement and Control System and Appendix C: Dual Camera G.

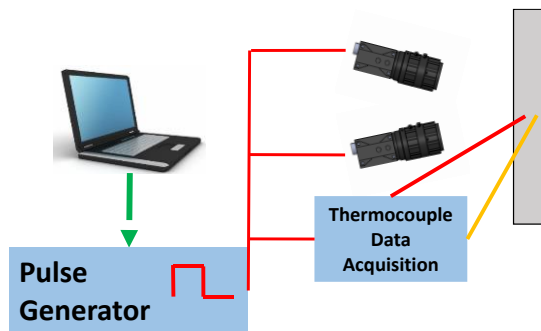


Figure 44: Synchronization of images and thermal feedback data

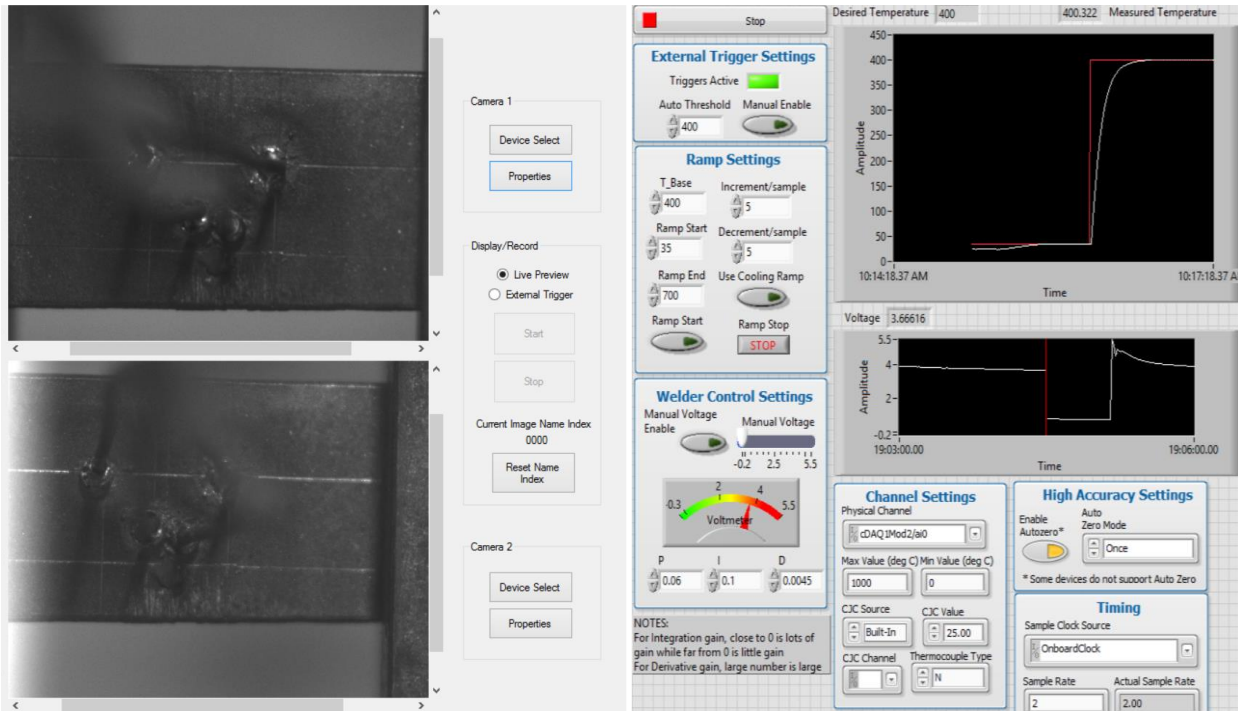


Figure 45: left) Dual camera control GUI; right) Thermal control and data logging GUI

3.5. Maintaining an Inert Atmosphere in the Calibration Chamber

In order to prevent the oxidation of the test surface at elevated temperatures, it is necessary to conduct the thermal camera calibrations within an inert environment. A simple approach to attaining an inert environment is to fill the chamber with an inert gas such as argon. By providing a constant flow of ultrahigh purity argon (99.999%) through an inlet while also constricting the outlet, the argon being introduced into the chamber will mix with the pre-existing gas and prevent any surrounding air from re-entering the chamber. Since the gas exiting the chamber will be a mixture of air and argon, all the air will gradually be carried out of the chamber and replaced entirely with argon. This technique of creating an inert atmosphere is sometimes referred to as a dilution or mixing chamber approach, and it is commonly used to reduce the concentration of oxygen to as low as 10 parts per million (ppm) for oxidation intolerant welding applications. The time required to reduce the oxygen concentration of the camera calibration test chamber to 10ppm will depend on the inlet argon concentration, flow rate, and volume of the

chamber. A schematic representation of the mixing chamber and assumptions used to model the concentration in the mixing chamber as a function of time are included in Figure 46. The concentration of the mixing chamber as a function of time is included in Figure 47, which shows that the target 10ppm O_2 can be achieved after roughly 12.5 minutes of purging time.

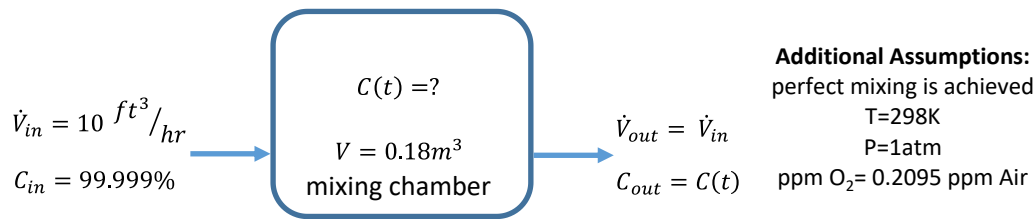


Figure 46: Mixing chamber schematic

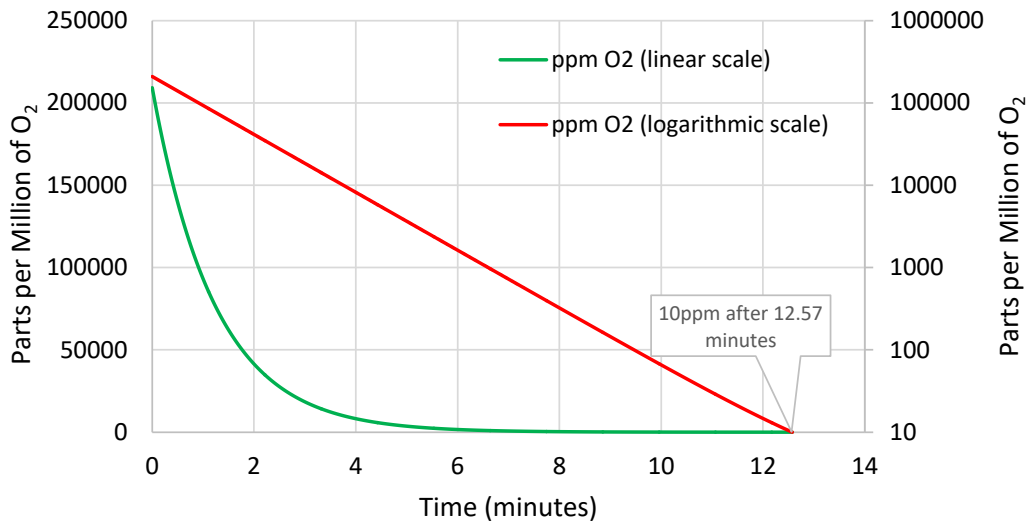


Figure 47: Oxygen concentration during argon purge process

In order to verify that a purge time of 12.5 minutes will actually provide a high level of oxidation prevention, a series of tests were conducted where an AISI 4140 steel alloy was held at an elevated temperature and imaged using a single camera with a NIR filter. Since the surface temperature is held constant, any change in the brightness of the image can be attributed to emissivity change due to oxidation or changes in the surface structure. Figure 48 shows an image taken of a heated specimen after spending several minutes at 570°C in the purged calibration chamber. By visual inspection of Figure 48

and Figure 49, it is possible to see that the brightness of the image has changed significantly between the beginning and the end of the test.

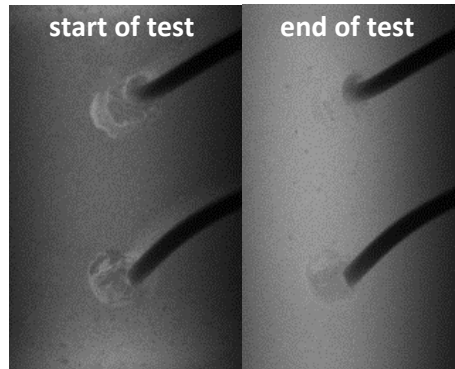


Figure 48: Visual effect of oxidation on emissivity (570°C, 850nm filter, sandblasted preparation)

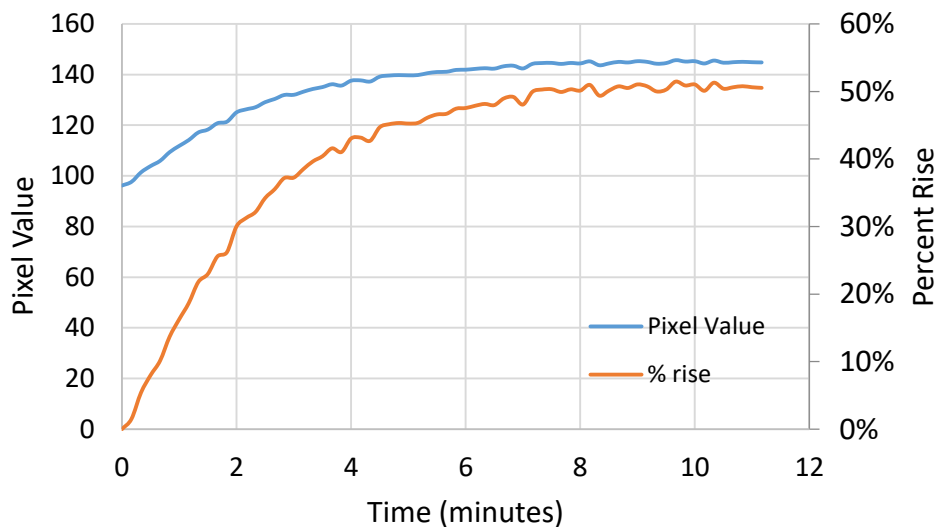


Figure 49: Effect of oxidation on average pixel value at 570°C and 850nm

Although a purging time of 12.5 minutes was expected to provide a high degree of oxidation protection based on the mixing chamber calculations, these calculations assume that there is perfect mixing within the chamber. In reality, it is possible that the flow pattern established within the chamber does not provide good mixing and so some oxygen remains trapped within the chamber. In order to assess whether or not the surface was oxidizing, the sample was bent in order to fracture the top oxide layer and was then examined with SEM and energy dispersive x-ray (EDX) chemical analysis. Figure 50 includes a

micrograph showing the measured chemical composition of an oxide flake and the underlying metal. Based on the evidence of oxidation in Figure 50, it is clear that the argon purge of 12.5 minutes was not effective at providing a fully inert atmosphere.

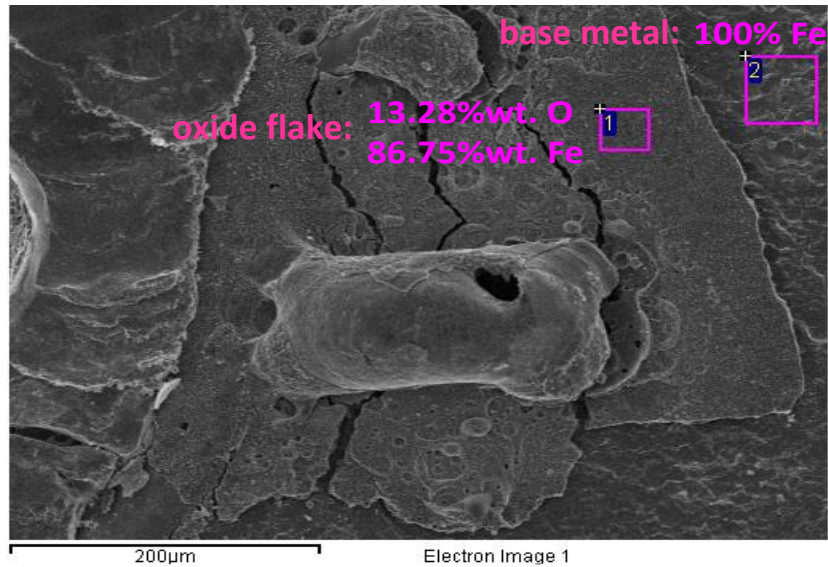


Figure 50: SEM image and energy dispersive x-ray (EDX) chemical analysis of fractured oxide layer

In order to improve the quality of the inert atmosphere, it is possible that continuing to purge for longer times will gradually reduce the oxygen concentration even further, however, the amount of time and gas which is wasted by this approach makes it undesirable. An alternative approach to provide argon shielding to the test specimen was implemented based on a directed nozzle. By directing the flow of ultrahigh purity argon directly at the test specimen, it is possible that oxidation may be prevented more effectively. Figure 51 shows an image of the argon nozzle shielding arrangement as well as the visual change in surface appearance and emissivity after testing at 800°C. Based on these results, the nozzle shielding approach was much more effective at preventing oxidation.

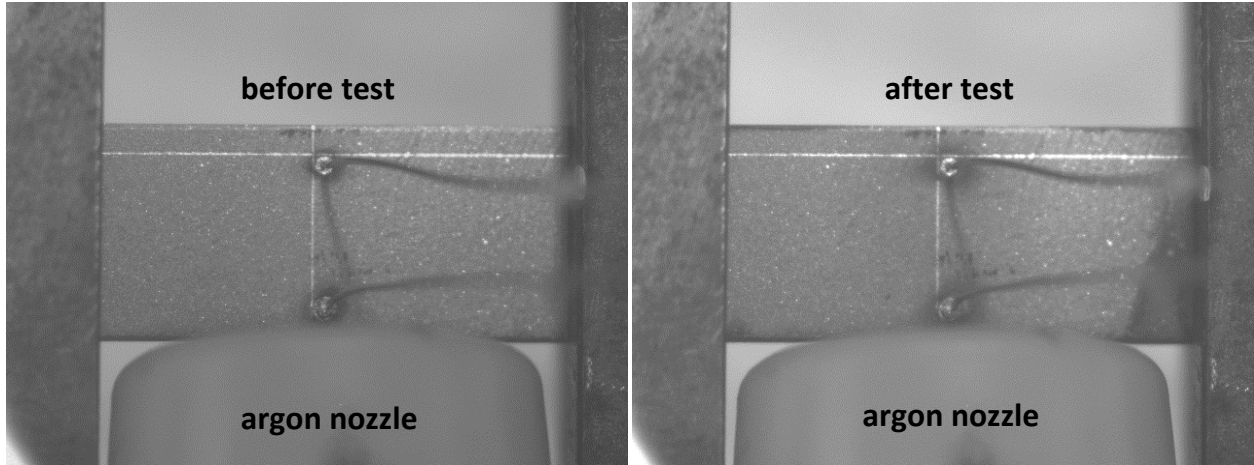


Figure 51: Sandblasted steel shielded with argon nozzle after cycling at 800°C

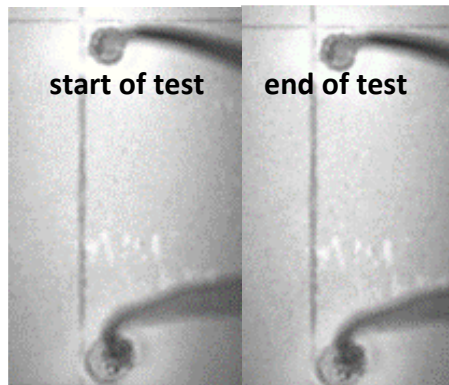


Figure 52: Visual effect of oxidation on emissivity (800°C, 850nm filter)

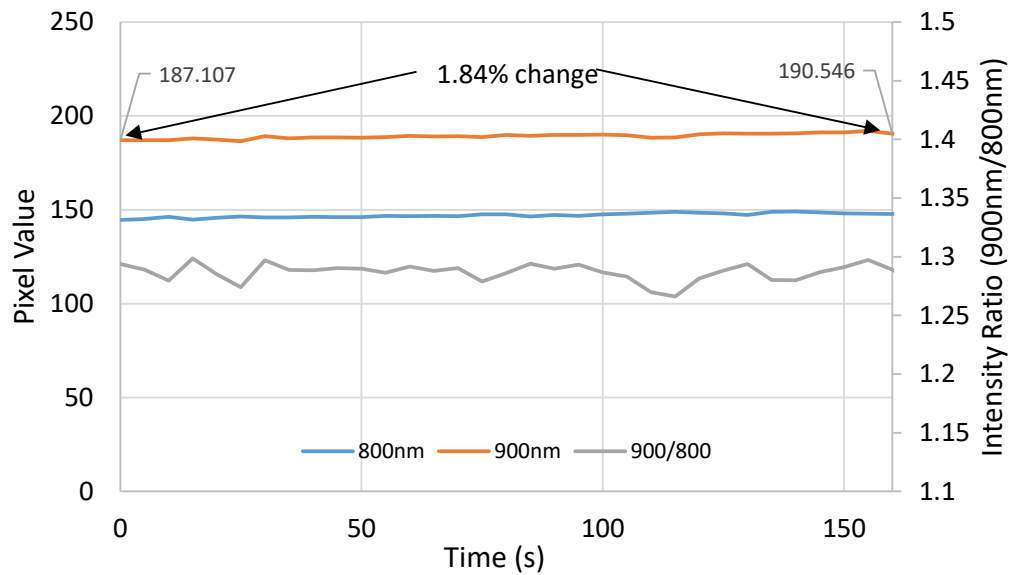


Figure 53: Effect of oxidation on average pixel value a sandblasted steel sample at 800°C

Chapter 4: Thermal Camera Calibration Procedure

Using the thermal camera calibration equipment discussed in Chapter 3, it is possible to calibrate the CCD cameras to operate as a dual-band pyrometer system. The purpose of this chapter is to summarize the preparation steps, equipment settings, and data processing strategies that are involved in setting up and calibrating the thermal camera.

4.1. Material Selection and Sample Preparation

Due to the adverse effects of spectral emission peaks, it is expected that different materials may require their own specific thermal calibration functions. As a result, one of the most important variables for the calibration is the material being tested. The steel alloy AISI 4140 was chosen for the initial calibration tests due to the fact that it is a popular heat-treatable alloy, it has a moderate hardenability, and it is widely studied and documented in a large volume of materials science literature. The use of a well-studied alloy such as AISI 4140 makes it easier to compare the material's microstructure and hardness properties against the thermal history observed by the camera. The standardized dimensions of the test specimen, the locations of the thermocouple junctions, and the region of pixels used during the calibration process are provided in Figure 54.

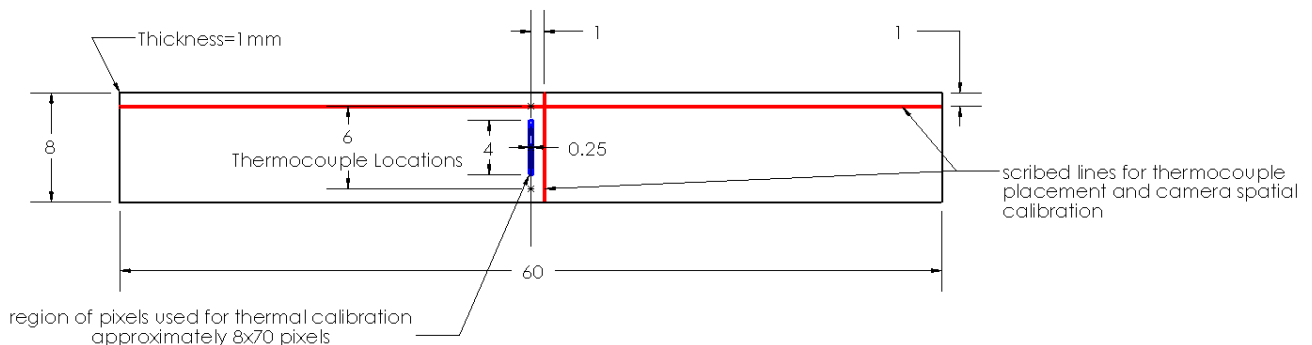


Figure 54: Dimensions of the standardized thermal camera calibration test specimen

In addition to the material type, the surface condition may have an influence on the calibration results. For the following work, samples were intentionally prepared with two significantly different

surface textures; half of the samples were prepared by sandblasting the surface in order to give it a dull, rough texture while the other half of the samples were polished with 320 grit silicon carbide sandpaper in order to create a shiny, smooth texture. The polished samples were prepared with the polishing marks being parallel to the length of the test specimen. In addition, all samples were rinsed in ethanol to dissolve any surface oils and were handled with clean Nitrile gloves to avoid subsequent contamination of the surface. Examples of polished and sandblasted samples which have undergone the complete preparation process are included in Figure 55.

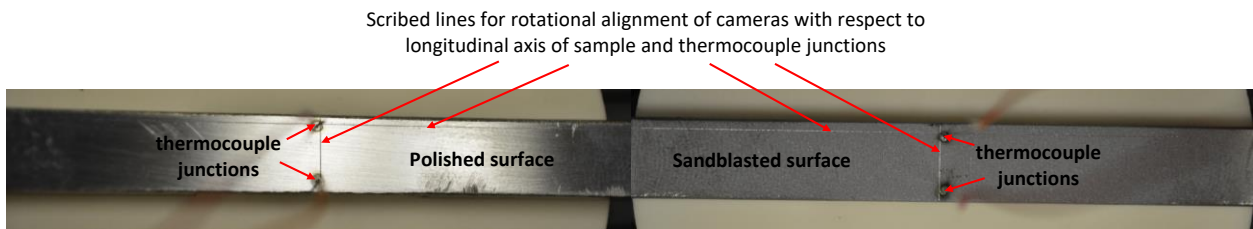


Figure 55: Examples of polished and sandblasted thermal camera calibration test specimens

4.2. Imaging Settings and Filter Specification

Recall from Chapter 2: Thermal Imaging Theory, that the camera sensors being used for this project can encode the incident radiation signal with only 8-bits of linearly spaced dynamic range. In order to improve the useful imaging range of the camera, three imaging parameters are available which allow the camera to be adjusted to operate across a wider range of lighting conditions. For example, a camera's lens often contains an orifice or aperture which determines the relative fraction of light rays which can pass through the lens and reach the sensor without being blocked. Using a large aperture allows the lens to gather more light and causes the sensor to detect a greater signal intensity. In a similar manner, changing the amount of time that the imaging sensors are exposed the incident radiation will influence the sensor's output for a given lighting condition. Finally, it is possible to apply an electrical amplification or gain to the analog signal generated by each pixel prior to analog to digital conversion in order to adjust its output for a given lighting condition. Since adjusting the imaging settings will alter the relationship


between incident radiation and signal intensity, it is important that these settings are documented as part of the thermal camera calibration process. For the specification of the sensor’s exposure time, it is possible to state the allotted time directly in seconds, however, since most exposure times are small fractions of a second, it is preferred to record the exposure frequency instead. Rather than expressing the exposure time in seconds, a frequency of exposure frame rates in Hertz (Hz) will be used in this thesis, such that exposure times of 1/4, 1/15, and 1/60 seconds can be represented instead as 4Hz, 15Hz, and 60Hz respectively.

The gain settings provided by the camera represent the level of electronic amplification which is applied to each pixel’s signal before being digitized into an 8-bit value. Electronic gain is commonly implemented using the logarithmic Decibel scale (dB) given in Equation 10. It should be noted that the use of electric signal gain should be minimized since it will introduce additional noise into the image and degrade image quality.

Equation 10: $G_{linear} = 20 \log_{10} G_{dB}$

In order to test the calibration procedure with a variety of camera parameters, the four settings included in Table 3 were selected. These settings are expected to allow the cameras to operate over a wide range of temperatures.

Table 3: Standardized exposure frequency and gain settings

Camera Settings			
4Hz, 6.91dB	4Hz, 0dB	15Hz, 0dB	60Hz, 0dB
Low Temperature Imaging			High Temperature Imaging

For example, the long exposure and high gain settings will still be effective at generating a signal despite the relatively small amount of radiation leaving a cold surface, however, these settings will cause the sensor to saturate easily as the radiation intensity increases. In contrast, the short exposure and low gain settings will not be able to detect the radiation emitted by cool surfaces, however, these settings will

prevent the sensor from saturating until higher temperatures are achieved and the level of radiation is increased. Finally, it should be noted that the large aperture size of f/1.4 was chosen to maximize the amount of light available to the sensor and increase low temperature imaging capabilities.

Recall that in section 2.5: Sensor-Compensated Model of Dual-Band Pyrometry of a Blackbody, the thermal imaging performance of the system was simulated using a variety of bandpass filter choices. For the sake of simplicity, the calibration experiments included in this report were conducted using only a single pair of filters. The filters which were chosen are 800nm and 900nm thin film interference bandpass filters which both have a full-width-half max (FWHM) values of 10nm. The spectral transmission curves for the 800nm and 900nm filters are provided in Figure 56 and Figure 57 respectively.

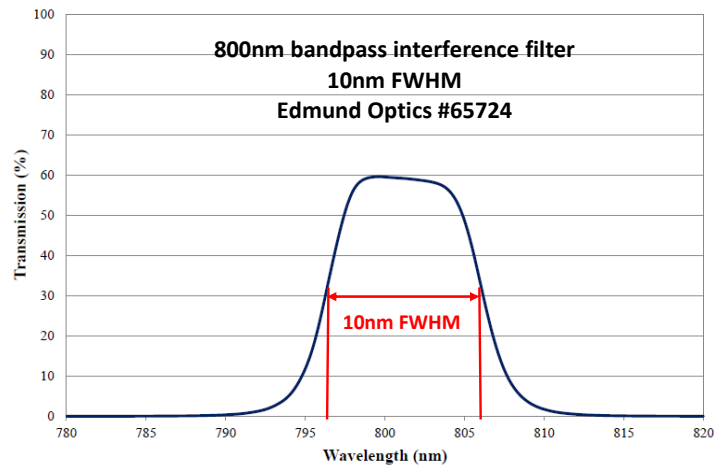


Figure 56: 800nm bandpass filter spectral transmissivity [38]

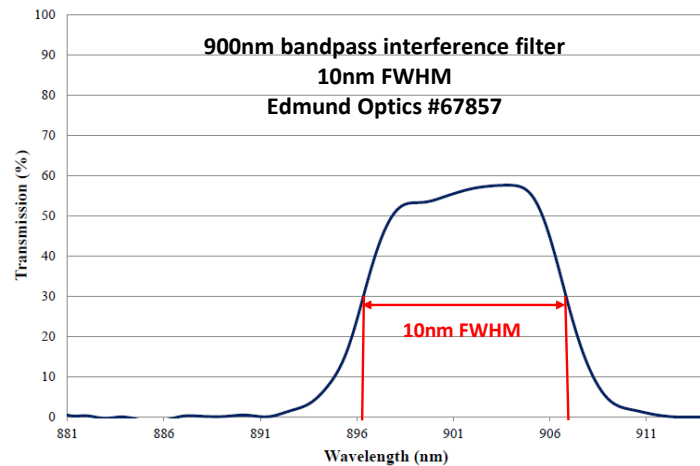


Figure 57: 900nm bandpass filter spectral transmissivity [39]

4.3. Data Collection and Processing

Once the test sample has been prepared and the camera's imaging parameters have been specified, it is possible to proceed with the data collection and processing steps of the thermal camera calibration procedure. The details of the data collection and processing steps will be illustrated in sequential order while using a set of experimental data as an example. The example data was collected from a polished sample, at a stage angle of 0° , and with camera settings of 60Hz exposure frequency and 0dB of gain. It should be noted that the purpose of the results provided in this chapter is to illustrate the data collection and processing steps rather than to draw conclusions about the results of the calibration process.

4.3.1. Step 1: Data Collection

The first step in the data collection process is to configure the temperature control and acquisition parameters. A heating rate of 10°C per second was found to be sufficient to limit oxidation at high temperature while also being slow enough to limit temperature changes during the longer exposure imaging settings. Once the thermal ramping process has begun, the data collection process is configured to begin automatically once the command temperature has exceeded the threshold value of 400°C . After the threshold temperature is reached, the thermocouple and cameras begin taking synchronized measurements at a rate of 2Hz. As a result, the experimental data provides a direct correlation between temperature and dual-band radiation intensity information for every 5°C of the temperature ramping process. A schematic illustration of the synchronized temperature and camera data collection is included in Figure 58.

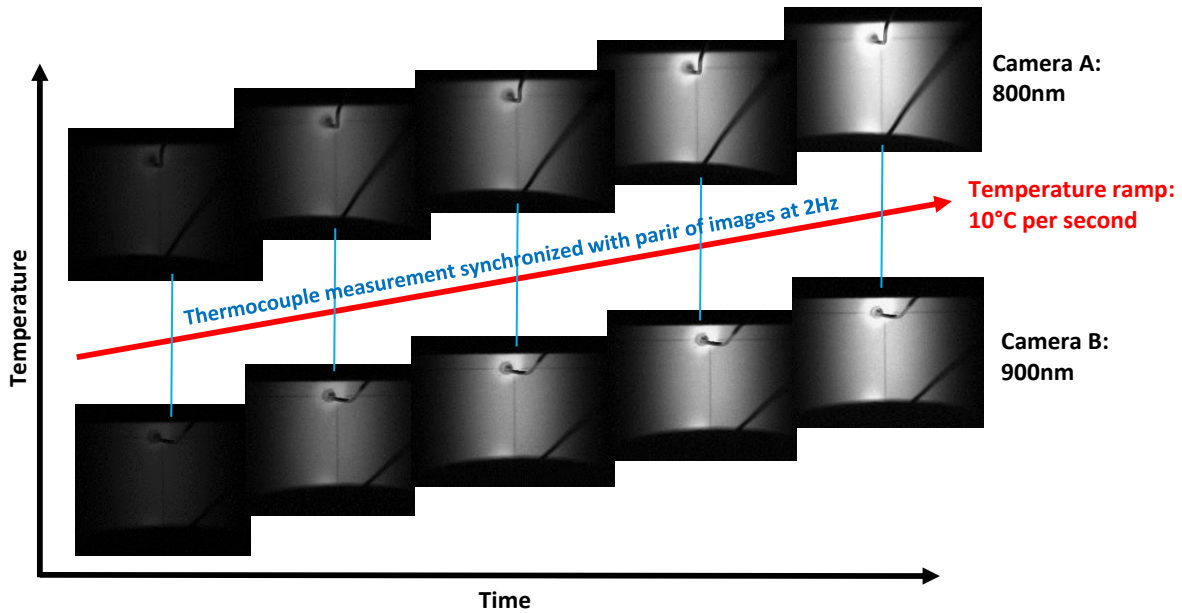


Figure 58: Synchronization of temperature ramp, thermocouple measurements, and image acquisition

4.3.2. Step 2: Thermal Calibration Data Extraction

After the temperature and image data has been collected, it is necessary to process the image data to extract the required pixel intensity information. Recall that the temperature measured by the thermocouple only correlates with the surface temperature within a narrow isothermal region existing between the thermocouples. This region is referred to as the thermal calibration region of interest (ROI), and only the data from the pixels within this region can be associated with the temperature measured by the thermocouple. Figure 59 identifies the thermal calibration ROI to contain a region 8 by 70 pixels, for a total of 560 data points that can be used from each image.

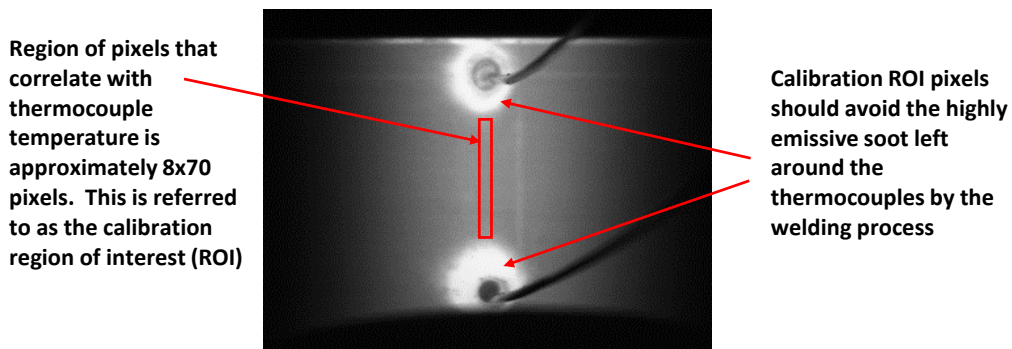


Figure 59: Surface appearance of heated steel specimen, highlighting region of interest for extracting thermal image calibration data

In order to reduce the influence of measurement error, the pixel-to-temperature correlation is based on the average pixel intensity within the thermal calibration ROI. Due to the large number of images and pixels that must be processed in order to extract the required data, a Matlab script has been developed which can perform this task automatically. The code of the Matlab script is included in Appendix D: Matlab Data Processing Code: Image_Processor_2CameraCalibrationProcessor_2.m. In addition to calculating the average pixel intensity, the included script calculates the minimum, maximum, range, and standard deviation of the calibration ROI of both cameras, while accounting for the cameras' spatial offset correction values.

4.3.3. Step 3: Separation of Valid and Invalid Thermal Calibration Results

By comparing thermocouple measurements with averaged pixel values from both cameras, it is possible to determine the correlation between temperature and pixel intensity ratio, however, since the data collection process is designed to begin before the cameras have begun detecting any radiation and end after both cameras have saturated, some of the collected data will be invalid for thermal calibration purposes. Fortunately, careful analysis of the data itself will provide the information required to distinguish between valid and invalid data.

As soon as a single pixel within the thermal calibration ROI reaches its maximum 8-bit digital value of 255, any additional radiation reaching that pixel will not be recorded. As a result, the relationship between surface temperature and pixel intensity ratio becomes invalid once pixels have begun to saturate. The point of saturation is easy to identify since the image processing script returns the maximum pixel value within the thermal calibration ROI. Figure 60 includes a plot of the maximum pixel intensity within the thermal calibration ROI during the thermal ramping process, however, this figure shows some unexpected results. For example, the camera which was imaging at the 900nm wavelength saturated at a digital value of 248 rather than 255. So far, this saturation mismatch can only be explained as an internal

error the sensor's analog to digital converter. Although the saturation mismatch was unexpected, the fact that the saturation of one of the cameras happens at 248 rather than 255 can easily be incorporated into the data analysis procedure. Another unexpected result from Figure 60 is the fact that there is an inflection at 824°C; which is slightly before saturation occurs. The exact cause of the inflection is not certain, but it is speculated that it may be caused by a non-linear response in the camera's onboard electronics. Since the inflection in signal intensity does not accurately reflect the underlying thermal radiation phenomena, any data collected beyond the inflection point is considered to be invalid for the thermal camera calibration process.

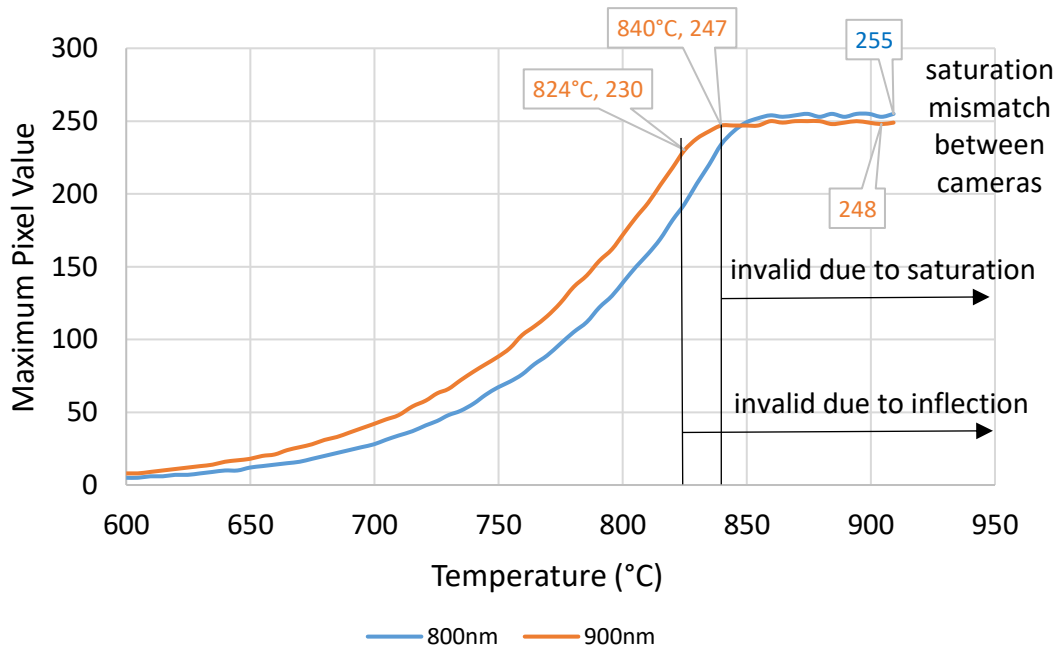


Figure 60: Maximum camera pixel values for both cameras versus thermocouple temperature measurements and the identification of a signal inflection

Once the signal enters the inflection and saturation zones, the natural variability of pixel values in the thermal calibration ROI will begin to decrease due to the fact that more and more pixels are approaching saturation. As a result, the inflection point will coincide with the temperature at which the range in pixel values begins to decrease. Figure 61 illustrates how the peak of the pixel range curve coincides with the same 824°C temperature which was previously identified as the signal inflection point.

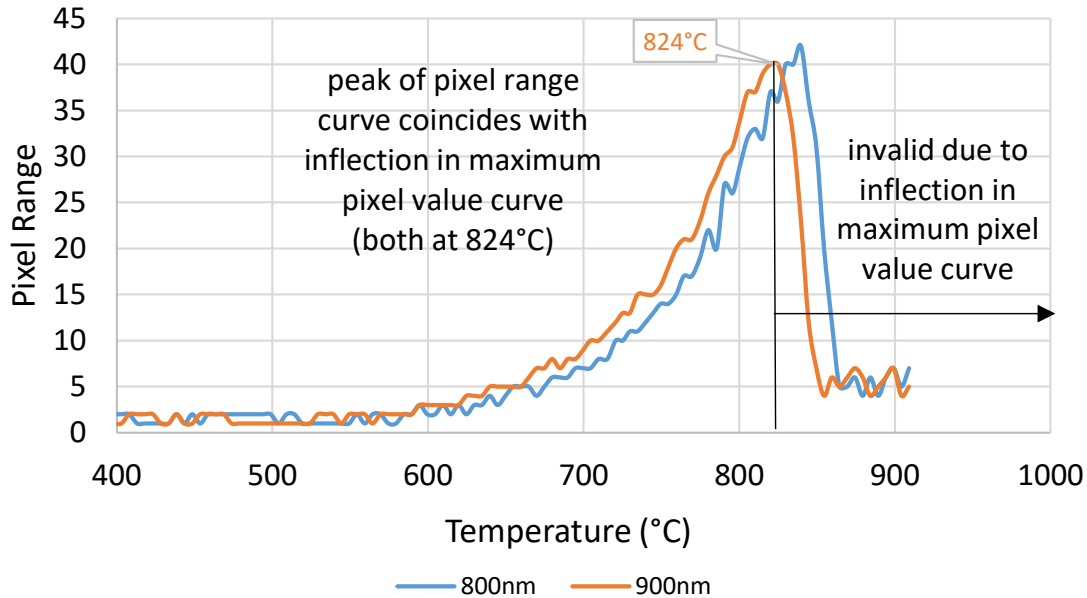


Figure 61: Identification of signal inflection temperature by using the maxima of pixel range curve

Another region of experimental data that is invalid for the thermal calibration process is the low temperature region where the signal detected by the camera is very small. When this occurs, the relative influence of electrical noise increases and results in a poor signal-to-noise ratio. Since dual-band pyrometry relies on the ratio between two pixel values, the influence of random noise is amplified at low temperatures because the denominator of the intensity ratio is small and the discretization resolution becomes coarse. As a result, the presence of even a single bit of noise can alter the resulting pixel intensity ratio in a significant and unstable manner. The temperature at which the signal to noise ratio and digital resolution become poor can be identified by the onset of instability in the standard deviation and average pixel intensity ratio values. According to Figure 62 and Figure 63, instability in the standard deviation and pixel intensity ratio data is observed at temperatures below 640°C. It should be noted that the oscillations observed in the low temperatures regions of these figures are due entirely to the shortcomings of the measurement equipment. Since the pixel measurements at low temperatures do not accurately reflect the underlying radiation phenomena, all data collected at temperatures below the region of instability is omitted from the valid camera calibration range.

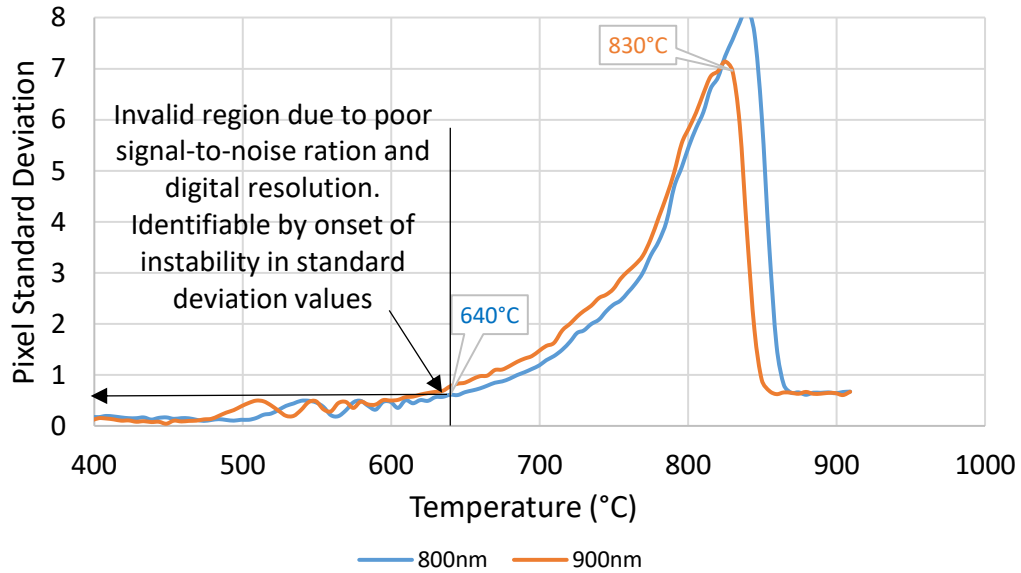


Figure 62: Instability of standard deviation results at low signal intensities

Instability is contrary to the radiation phenomena.

Instability is evidence of measurement error

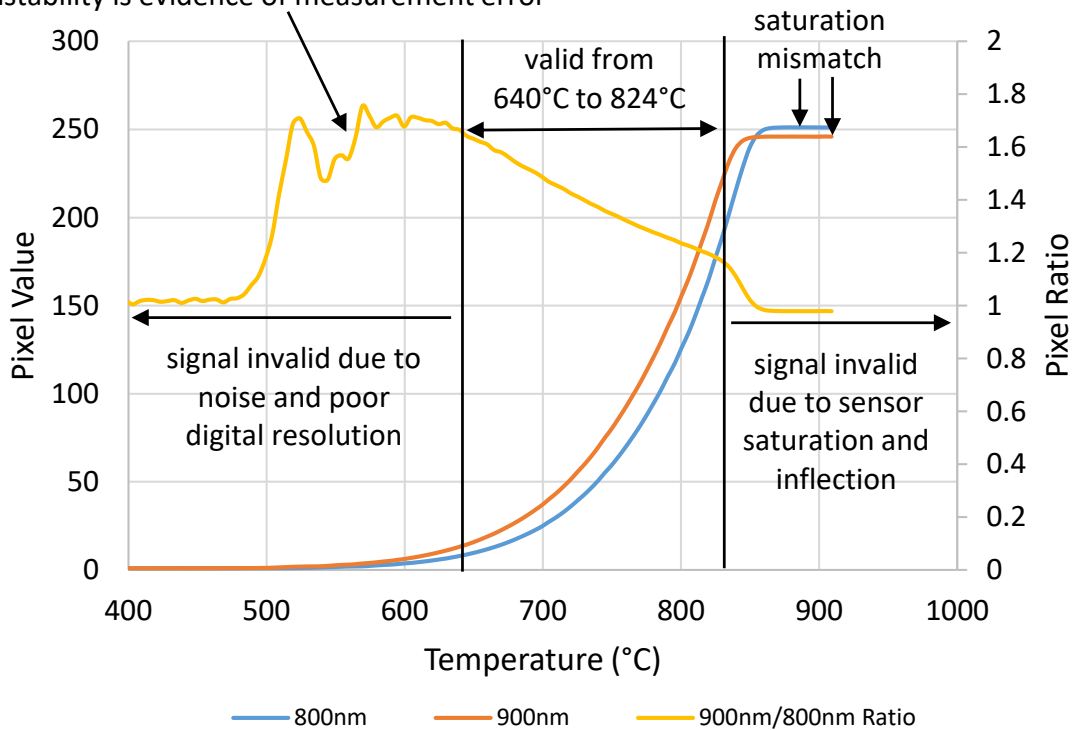


Figure 63: Valid thermal measurement range with respect to average pixel intensity and pixel ratio

4.3.4. Step 4: Identification of Thermal Calibration Polynomial

The next step in the data processing procedure is the identification of a polynomial which matches the experimental data and describes the surface temperature as a function of pixel intensity ratio. This has been accomplished by applying a 5th order least squares polynomial regression to the experimental data over the valid temperature range identified in Step 3. Figure 64 illustrates an excellent 5th order polynomial fit to the experimental data.

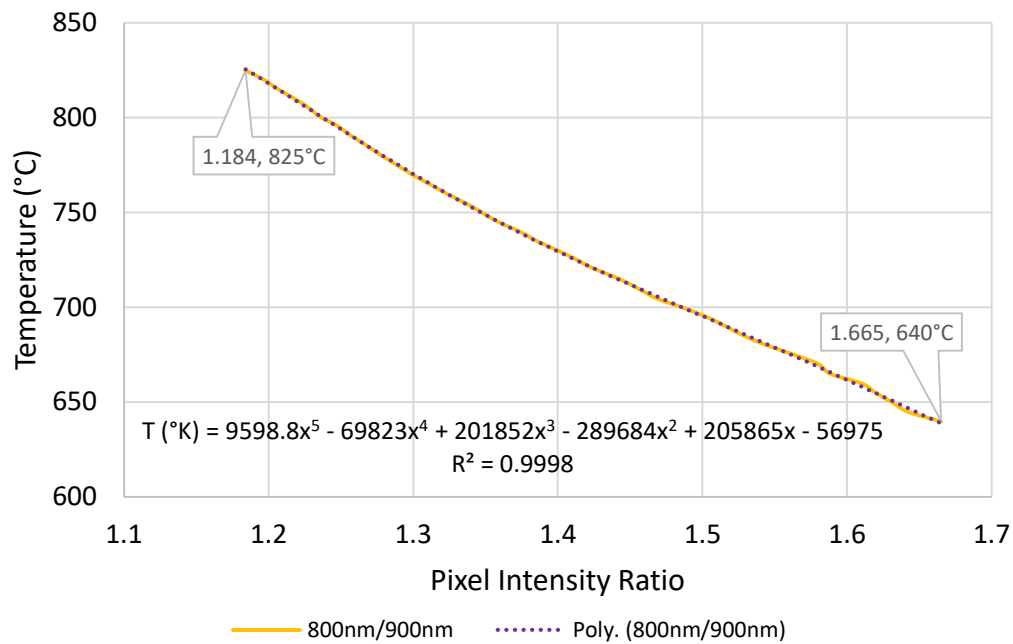


Figure 64: 5th order polynomial fit for pixel intensity ratio measured for cameras using 800 and 900 nm filters

4.3.5. Step 5: Apply the Thermal Camera Calibration Polynomial

By applying the thermal camera calibration polynomial identified in step 4, it is now possible to perform pyrometric temperature measurements. In order to apply the polynomial to a pair of bandpass filtered images, a special Matlab script has been developed and is included in Appendix E: Matlab Thermal Image Code: ThermallImageGenerator2.m. The thermal image generator script takes the calibration polynomial, valid thermal measurement range, two bandpass filtered images, and a region of interest to analyse. Figure 65 illustrates an example of selecting a thermal analysis ROI.

Region of pixels selected for thermal imaging analysis. This is referred to as the thermal analysis region of interest (ROI)

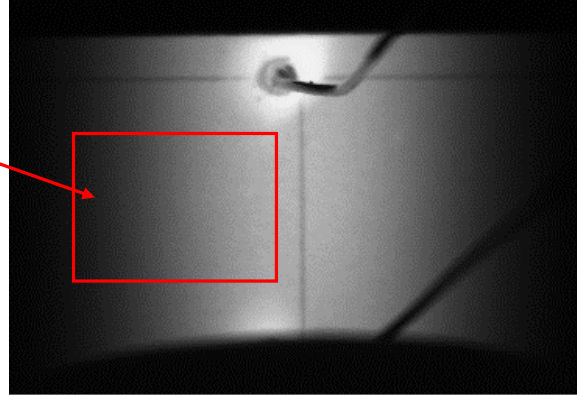


Figure 65: Selection of a thermal analysis ROI

An additional functionality which has been incorporated into the thermal imaging program is to apply a Gaussian blur filter to the images. The Gaussian blur filter is defined in Equation 11.

$$\textbf{Equation 11: } G(x, y) = \frac{1}{\sqrt{2\pi\sigma^2}} e^{-\frac{x^2}{2\sigma^2}}$$

As shown in Figure 66 a), there is a significant amount of spatial inhomogeneity in the raw image signal when viewed at the pixel level. The spatial inhomogeneity in the image will potentially become a problem if there is an imperfect spatial offset correction between the two cameras. As a result, it may be possible for a relatively dark pixel in one camera to be paired incorrectly with a relatively bright pixel in the other camera. By blurring the images, any short range pixel gradients are averaged out and the pixel intensity ratios will be less susceptible to the imperfect spatial mapping between cameras. The level of blur introduced to the image by the Gaussian blur filter is proportional to the σ factor. Figure 66 illustrates the effect of increasing the σ factor from 0 to 2, 4, and 8. The σ factor value of 8 was selected to be the standard blur factor for the remainder of the work in this report.

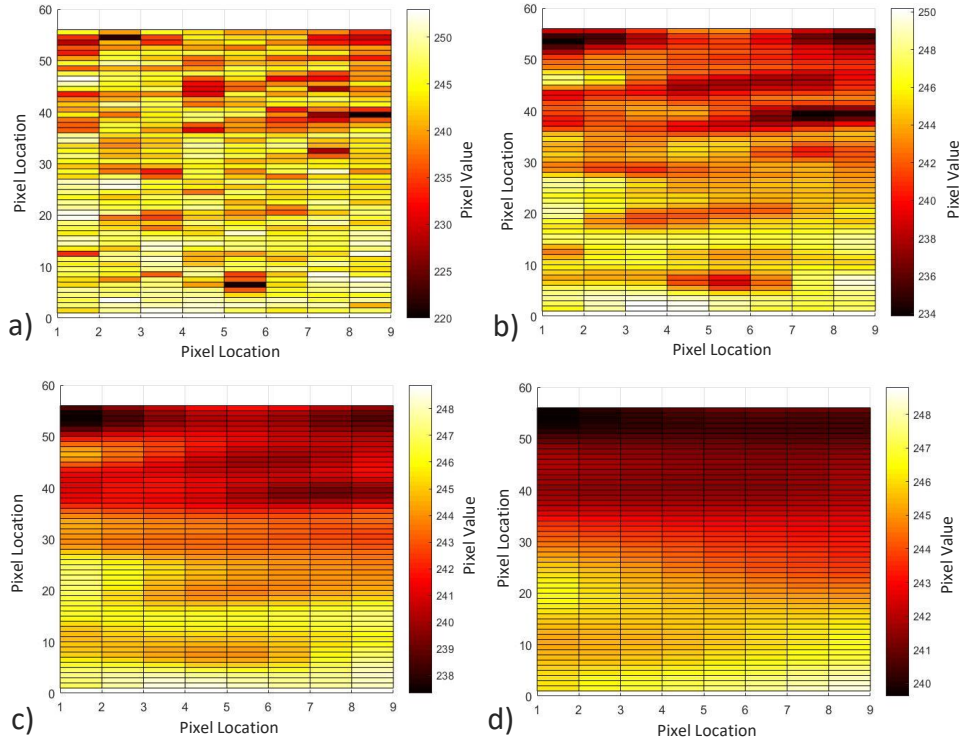


Figure 66: Pixel homogeneity with varying degrees of Gaussian blurr a) $\sigma=0$; b) $\sigma=2$; c) $\sigma=4$; d) $\sigma=8$

Using the blurred images, the thermal image program applies the thermal camera calibration polynomial and calculates the surface temperature. The process of converting two camera images into a single thermal image is illustrated in Figure 67. This figure is rather significant, for it is the cumulative result of a large development effort, and it demonstrates the capability of the low cost CCD system to acquire true thermal images based on dual-band pyrometry techniques.

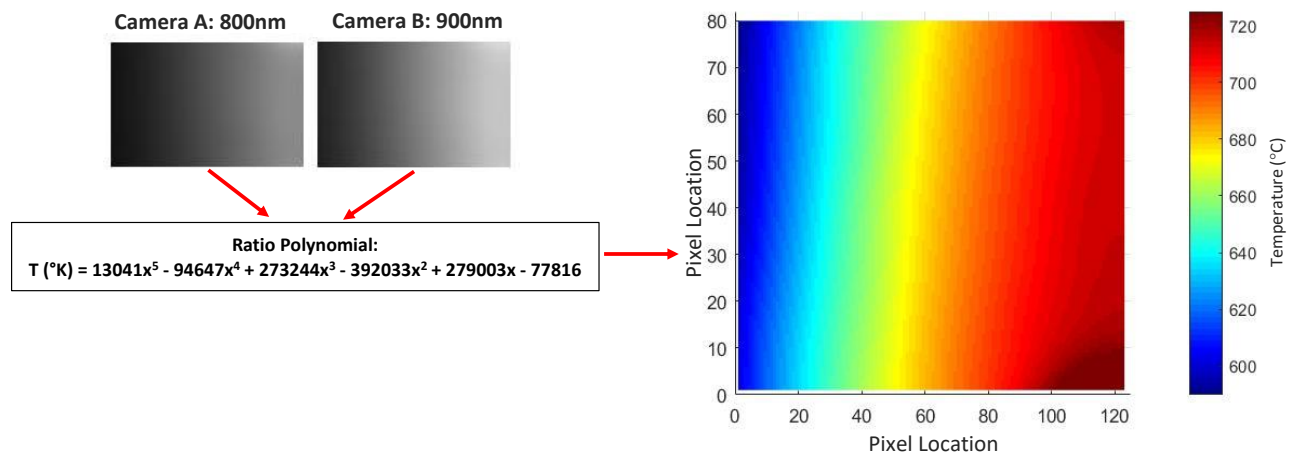


Figure 67: Temperature map generated by the CCD imaging system

Chapter 5: Thermal Calibration Results

As illustrated in Chapter 2: Thermal Imaging Theory, an appropriate data collection and processing procedure has been developed which allows the dual camera system to be calibrated to operate as a dual-band pyrometer. In order to compare the performance characteristics with the predictions made previously, a series of experiments have been conducted which evaluate the effects of material and imaging conditions on the thermal calibration results. The purpose of this chapter is to present and discuss the results of these thermal calibration experiments, however, it should be noted that the results provided in this report represent the only the initial stage of performance testing. A full investigation into the system's performance and capabilities as a thermal monitoring and microstructure prediction device are beyond the scope of the current project.

5.1. Calibration Repeatability Study

In order to be confident in the temperatures reported by the thermal imaging system, it is necessary to first be confident in the repeatability of the calibration process. A series of experiments were conducted in order to quantify the amount of discrepancy that exists between calibrations that are performed with the same test parameters.

5.1.1. Repeatability of Separate Samples

In order to test the repeatability of the thermal calibration process, the same calibration procedure was performed three times while using a newly prepared sample each time. The three samples were prepared in the same manner and imaged using the same camera parameters, therefore, any differences between the calibration results should illustrate the repeatability of the sample preparation procedure. The samples used for this experiment were all sandblasted to roughen the emitting surface and were imaged at a perspective angle of 0° , 15Hz exposure frequency, and 0dB of gain. Figure 68 shows the final thermal calibration curve attained for each of the three tests. According to Figure 68, the second

and third iterations of the test were almost identical, however the first test yielded thermal calibration results which are slightly different. For a given pixel intensity ratio, the discrepancy between the three calibration attempts was found to be less than 10°C. Although a calibration error of 10°C is likely to be an acceptable level of precision for the intended application of weld thermal monitoring, it is desirable to better understand the source of this calibration discrepancy. According to the results provided so far, it is possible to conclude that the calibration procedure is sensitive enough to subtle changes in the surface preparation, however, the influence of other test parameters and measurement errors remain unexplored and require further experimentation.

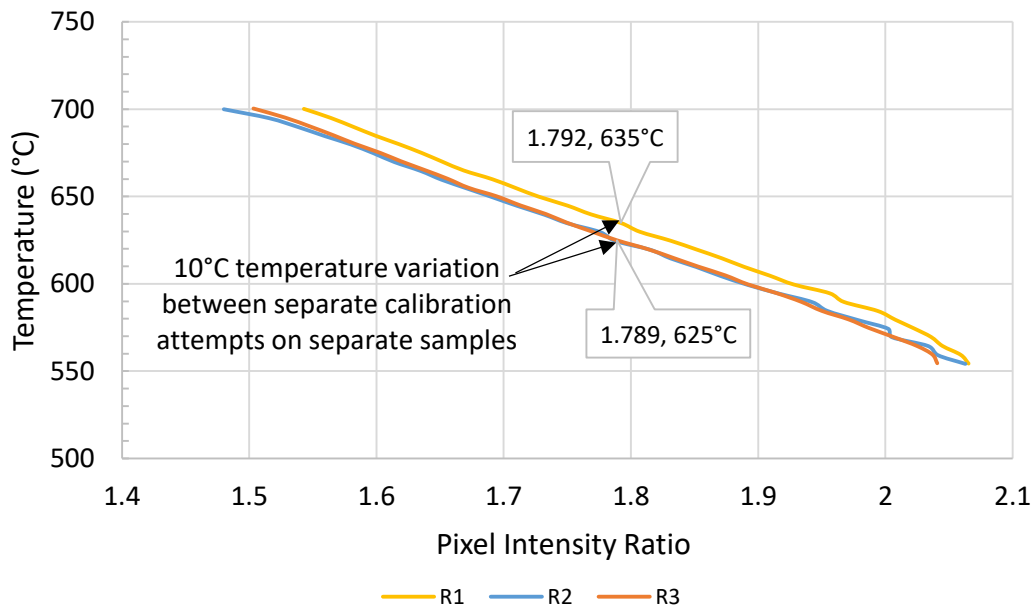


Figure 68: Thermal calibration repeatability tests using separate samples (Settings: Sandblasted surface oriented at 0°, imaging at 15Hz, and 0dB gain)

5.1.2. Repeatability of Consecutive Testing

A similar thermal calibration repeatability study was performed where the calibration procedure was performed three times, however, rather than using three different samples, this time the experiments were conducted by consecutive testing of the same sample. By using the same sample again and again, this repeatability investigation can eliminate the effects of sample preparation repeatability, however, it is possible that surface variation due to heating or oxidation may accumulate between multiple heating

cycles. The sample used for this experiment was polished and imaged at a perspective angle of 0° with 4Hz exposure frequency and 0dB of gain. Figure 69 shows the final thermal calibration curve attained for each of the three tests. According to Figure 69, disagreement between the first and second test is much larger than the disagreement between the second and third tests. As a result, it is possible that some surface variation takes place during the first thermal ramping process, however, the surface becomes more stable with subsequent tests.

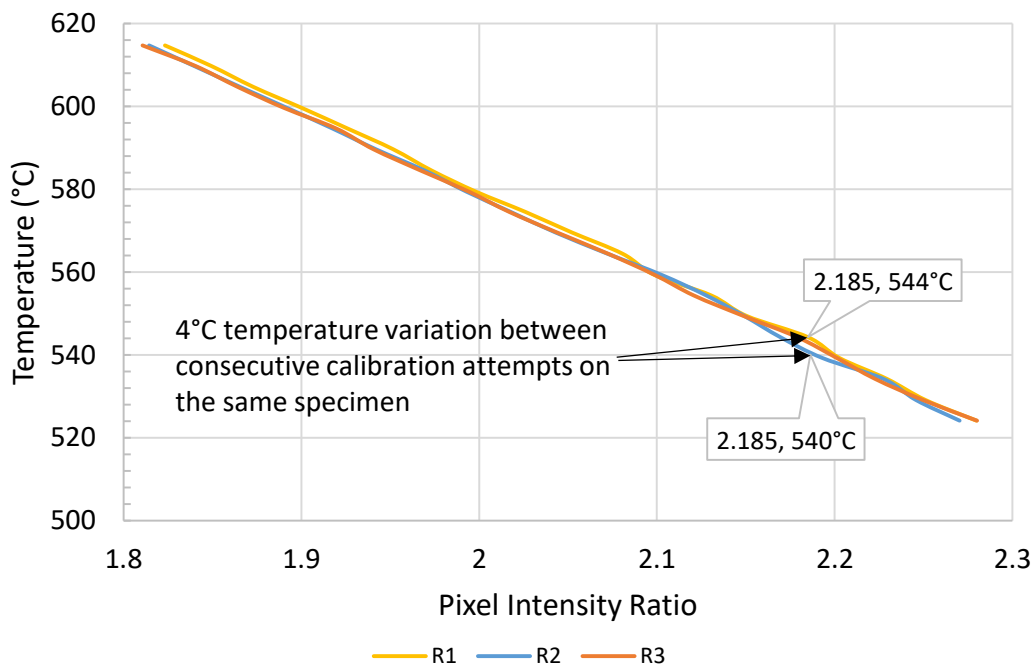


Figure 69: Thermal calibration repeatability tests using the same sample (Settings: Polished surface oriented at 0°, imaging at 4Hz and 0dB gain)

When comparing the results in Figure 69 with those of the previous repeatability experiment, it is evident that the maximum calibration disagreement has reduced from 10°C to 5°C. As a result, the repeatability between consecutive testing of the same sample appears to be better than that of the testing of similarly prepared samples. Although this result seems to indicate that differences in surface preparation may contribute towards a significant portion of the calibration discrepancy, it is important to consider the other characteristics of the surfaces before drawing any conclusions. For example, recall that of the two repeatability studies conducted so far, the first was conducted using sandblasted samples

while the second was conducted using polished samples. As a result, another possible explanation for the greater calibration discrepancy in the separately prepared samples is that the sandblasted surface itself is naturally less consistent. Figure 70 compares the standard deviation in the calibration data from two experiments carried out with identical imaging settings but different surface preparations. According to Figure 70, the standard deviation of the calibration data is significantly larger for the sandblasted surface when compared to the polished surface. Due to the fact that greater standard deviation was observed for the sandblasted samples, it is expected that both the natural surface variability of rough surfaces may be responsible for the greater discrepancy between subsequent calibrations.

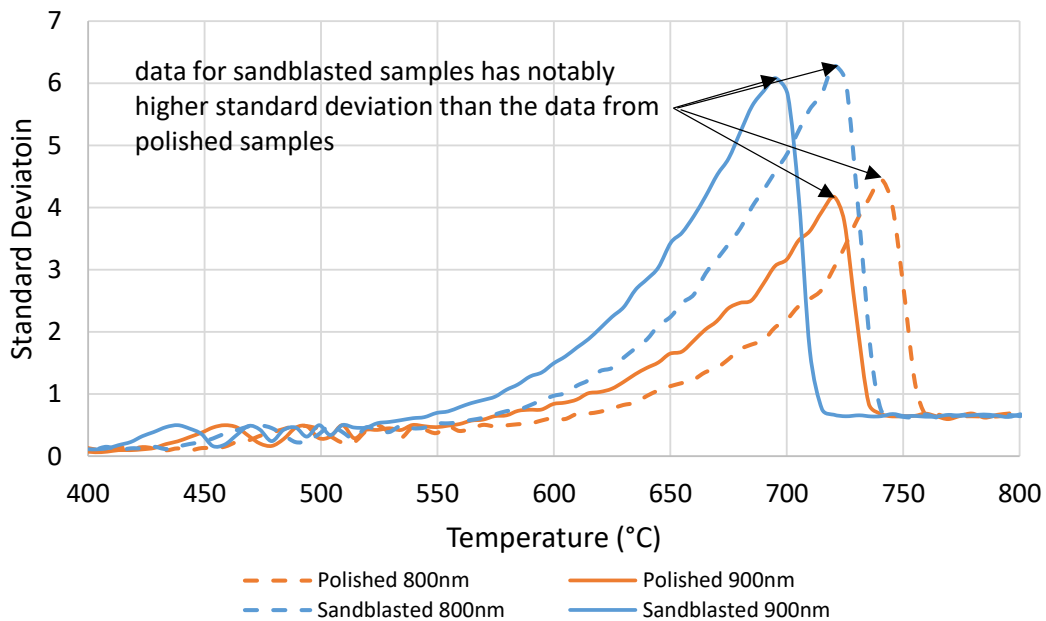


Figure 70: Comparison of standard deviation in thermal calibration data between sandblasted and polished samples (Settings: surface oriented at 0°, imaging at 15Hz and 0dB gain)

5.2. Influence of Imaging Settings on Calibration Results

In section 4.2: Imaging Settings and Filter Specification, a set of four considerably different imaging conditions were selected with the expectation that changing the imaging settings will allow the camera to be tuned to operate well at either low or high temperature conditions. In addition, in section 2.5L Sensor-Compensated Model of Dual-Band Pyrometry of a Blackbody, it was predicted that configuring the camera to measure low or high temperatures will change the system’s dynamic measurement range. In order to test these predictions, set of four polished test samples were prepared and tested with each of the four standardized imaging settings. The final calibration curves and measurement ranges for these imaging settings have been included in Figure 71 and Table 4 respectively.

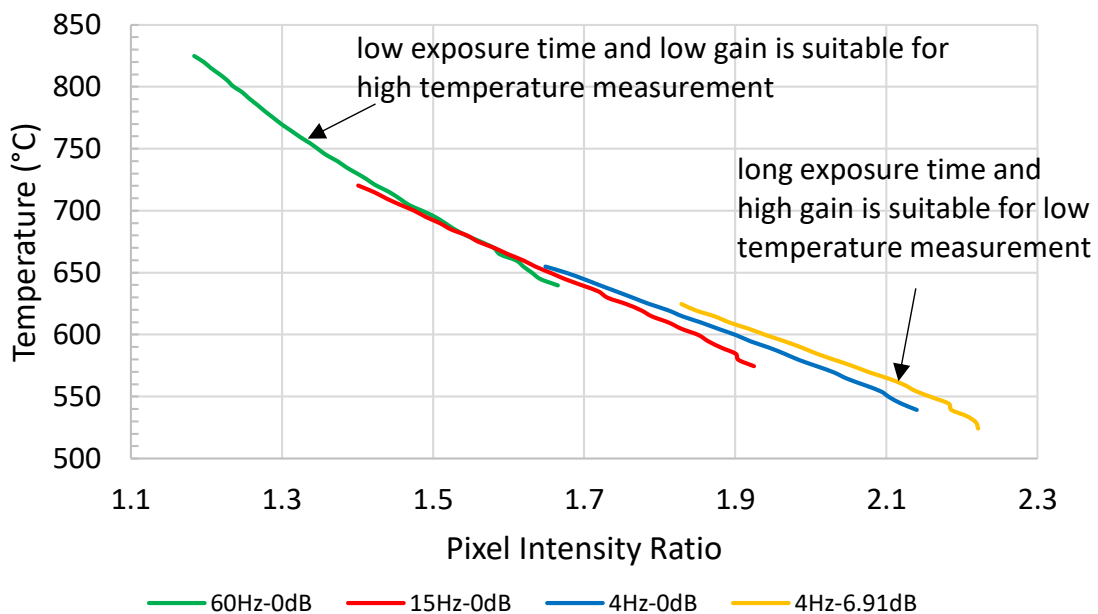


Figure 71: Thermal calibration results for various camera settings

Table 4: Thermal measurement capabilities of the standardized camera settings

	Camera Settings			
	4Hz, 6.91dB	4Hz, 0dB	15Hz, 0dB	60Hz, 0dB
Min. Measurable Temperature (°C)	525	540	575	640
Max. Measurable Temperature (°C)	625	655	720	825
Measurable Range (°C)	100	115	145	185

The results given in Figure 71 and Table 4 confirm the general predictions about the effects of camera settings on the system's performance. For example, it is evident that using long exposure times and large signal gains, such as the 4Hz, 6.91dB configuration, will allow the system to detect lower temperatures at the expense of dynamic range. In contrast, using short exposure times and low signal gains, such as the 60Hz, 0dB configuration, will allow the system to detect higher temperatures and have an increased dynamic range. Unfortunately, none of the available imaging settings have sufficient capability to measure the 800°C to 500°C temperature range required to observe T8/5 times directly. Although no individual combination of settings can provide the desired dynamic range, the maximum and minimum temperatures observed between the four tested camera settings are 825°C and 525°C respectively. As a result, it is expected that the desired temperature range can be achieved by capturing an image at each of the four camera settings and then combining the thermal information into a single high dynamic range measurement. This technique is known as high dynamic range imaging (HDRI) and is commonly used for photography applications that involve difficult lighting conditions. An example of the application of HDRI for standard photography can be seen in Figure 72, and this can be easily implemented using a number of available algorithms.

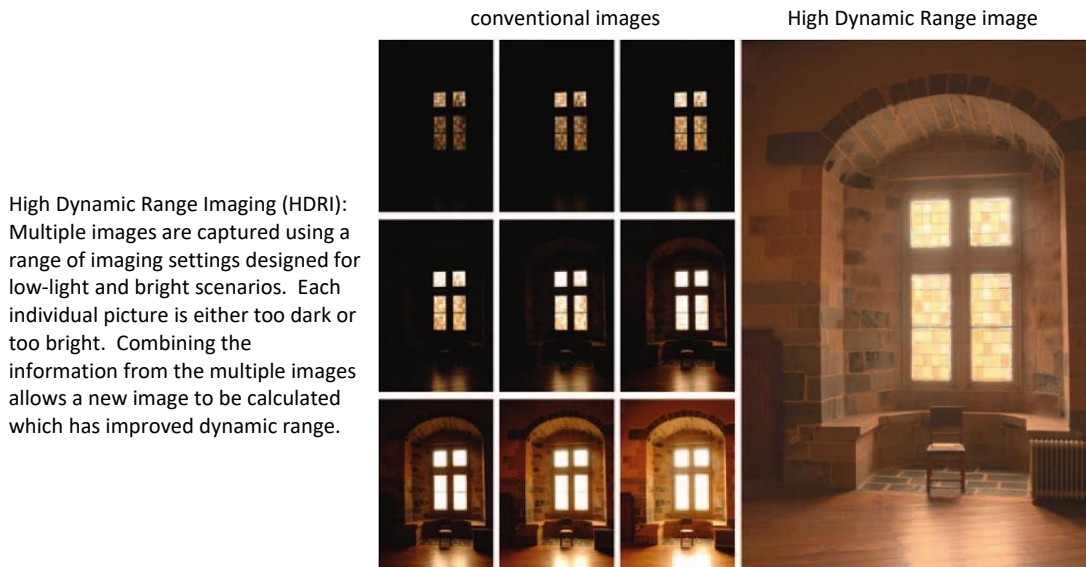


Figure 72: Example application of high dynamic range imaging [40]

In Chapter 2: Thermal Imaging Theory, spectral emission peaks were identified as a potential source of error for dual-band pyrometers. In Chapter 3: Camera Calibration Equipment, it was predicted that the presence of spectral emissive peaks could be observed and corrected for during the calibration process. Figure 73 shows the comparison between the simulated pixel intensity ratios and the experimental pixel intensity ratios with respect to temperature. Recall that the simulated pixel intensity ratios are based on the camera's response to the ideal emission profile from a blackbody, therefore, any discrepancy between the simulated and experimental results is evidence of test surface having a non-ideal spectral emission profile. According to Figure 73, there is a significant discrepancy between the ideal spectral power ratio and the experimental results, however, the experimental results underestimate the temperature consistently by a factor of 0.755 correction across all the tested camera settings. In order for the emissive power ratios to differ by a consistent factor of 0.755, it is likely that either the $900\pm 10\text{nm}$ waveband corresponds to a spectral valley or the $800\pm 10\text{nm}$ waveband corresponds to a spectral peak. In summary, these results suggest that the tested material possesses significant spectral emissive peaks, however, the prescribed calibration process can successfully compensate for their effects.

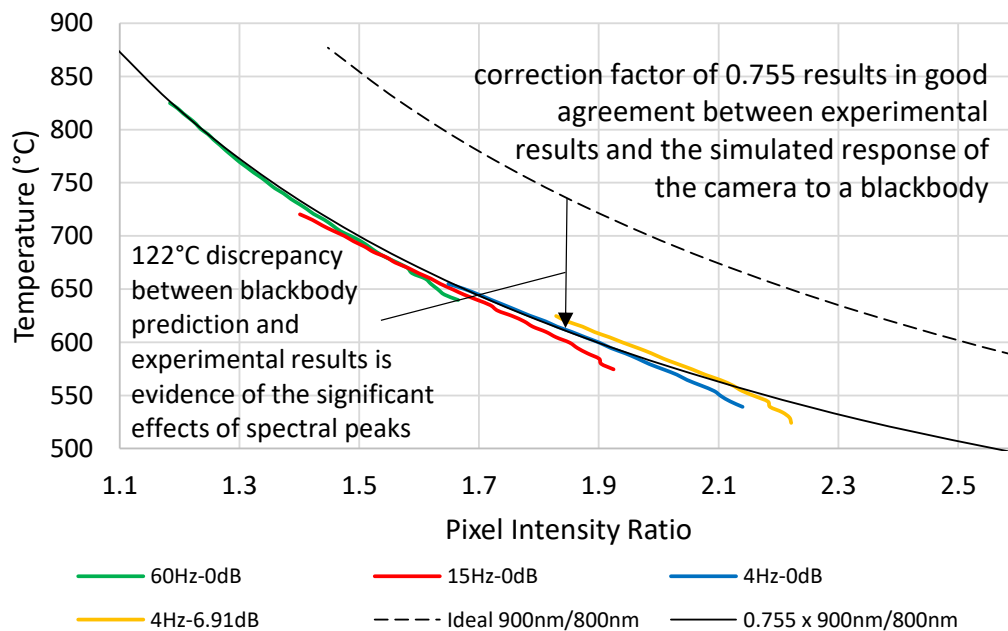


Figure 73: Evidence of spectral peaks through comparing simulated and measured pixel intensity ratios.

5.3. Effect of Surface Type and Perspective Angle

Another important step involved in assessing the performance characteristics of the thermal imaging system is to determine the combined effects of surface type and perspective angle. Recall from Chapter 2: Thermal Imaging Theory, that the spectral emissivity can be affected by factors such as the surface roughness and viewing angle. In order to investigate the spectral differences between the sandblasted and polished surfaces, experiments were conducted for both types of sample with the same imaging parameters of 15Hz exposure frequency and 0dB gain. In addition, similar tests were performed at viewing angles of 0° and 45° in order to determine if the spectra inhomogeneity effects are influenced by the viewing angle. The final calibration results of these four experiments are plotted together in Figure 74 and summarized in Table 5 and Table 6.

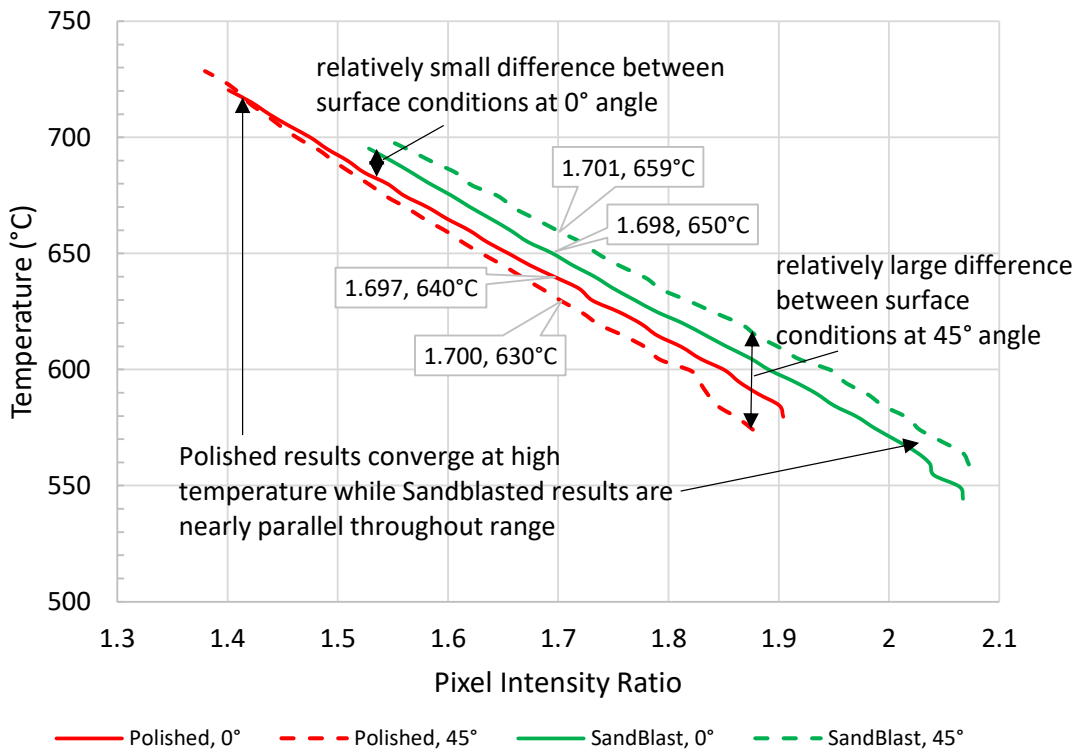


Figure 74: Thermal calibration comparison between surface types and perspective angles

Table 5: Thermal measurement discrepancy between surface types

Perspective Angle	Effect of Sandblasting vs Polishing (°C)
0°	10
45°	29

Table 6: Thermal measurement discrepancy between viewing angles

Surface Condition	Effect of Angle Change from 0° to 45° (°C)
Polished	-10
Sandblasted	9

Based on the results in Figure 74, it can be seen that the radiation intensity ratios do not agree completely between the sandblasted and polished surfaces. In order for the radiation intensity ratios to differ, the spectral emission intensity at the wavelengths of 800nm and 900nm must be different between the surface conditions. These results confirm that spectral inhomogeneity will be an issue for practical applications that cannot be solved without direct calibration of the camera to the emissive properties of the surface of interest. According to Table 5, the discrepancy between surface calibrations increases from 10°C to 29°C when viewed at an angle is increased from 0° to 45°. In order for the pixel intensity ratio to be a function of viewing angle, the relative intensities of the spectral emission at 800nm and 900nm must also be a function of viewing angle. In addition, Table 6 indicates that increasing the viewing angle causes the calibration curve to shift downwards for the polished surface while the opposite is the case for the sandblasted surface. Although the results provided here are only preliminary, they demonstrate that changes in the surface texture and viewing angle will alter the emission spectrum in a measurable way. If the effects of surface condition and viewing angle are not compensated for during the calibration procedure, the calibration uncertainty of a given alloy may exceed $\pm 30^\circ\text{C}$. It is recommended that future work be conducted in order to better understand the effects of alloy type, surface type, and viewing angle on the accuracy of the calibration results.

Chapter 6: Conclusions and Recommendations

The motivation behind this research project was to improve the available tools for the measurement of thermal history in welding applications. By quantifying the thermal history experienced by the material, it is possible for the welding development process to rely less on trial and error and more on fundamental materials science principles. Thermal imaging techniques were identified as the most appropriate measurement technique due to their non-contact, high temperature, and spatial resolution capabilities. In order to provide thermal imaging capabilities at the lowest possible cost, it was proposed that standard CCD sensors could be used to create a dual-band pyrometer system. A literature review determined that similar CCD thermal imaging systems have been developed for welding research purposes, however, commercial versions of the CCD thermal imaging systems are not available. As a result, the desire to use a CCD based thermal imaging system as a feedback device for welding applications could not be realized without first developing the thermal imaging system itself. Due to the significant effort required to develop a custom thermal imaging system, the goals of this report were to focus on documenting the development process and calibration procedure. In other words, this work is to serve as a solid foundation for the foundation for the future work of testing the system as a weld monitoring device.

The dual-band pyrometry approach was chosen due to the fact that it can inherently reduce the influence of the surface's emissivity, however, it was noted that an emitting surface with spectral peaks will require special calibration. The performance of the thermal imaging system was simulated under ideal conditions and it was discovered that the range in signal intensity from surfaces between 800°C to 500°C far exceeds the dynamic range of the camera's sensor. As a result, a given set of camera settings was expected to be able to measure only a narrow range of temperatures. In addition, with the

measurement range predicted to be reduced even further by choosing bandpass filters whose central wavelengths are further apart, or when imaging relatively cool surfaces.

In order to correct for the influence of spectral peaks, a system and method was devised to calibrate the thermal camera system experimentally. By using the actual material and surface preparation of interest during the calibration process, it was expected that the effects of spectral peaks could be identified and compensated for. The equipment which was developed to conduct the thermal camera calibration was designed to provide a controlled environment in which to image the heated material and correlate the bandpass filtered pixel intensity ratios with temperatures measured by a thermocouple. In order to improve the accuracy of the thermocouple measurements, resistive joule heating was conducted with an alternating current frequency of 60Hz or greater and a balanced wave duty cycle. The utility of the calibration system was also greatly enhanced through the development of a closed loop temperature control system and custom data acquisition programs.

The thermal camera calibration process was illustrated in a step-by-step fashion, beginning with the material selection and surface preparation process. By also specifying the imaging settings and control system parameters, the data collection process could be performed automatically by the calibration equipment. Once the experimental data was collected, a series data extraction programs and analysis techniques were provided in order to determine a 5th order thermal camera calibration polynomial which describes the surface temperature as a function of pixel intensity ratio. By applying the calibration polynomial to a pair of bandpass filtered images, the ability of the system to operate as a fully operational dual-band pyrometer was demonstrated.

Although the system has proven its capabilities to operate as a thermal imaging device, the system could not be applied to a welding application without first testing the reliability of the calibration and the system's performance characteristics. Through a series of repeatability tests, it was found that the effects

of surface preparation variations lead to temperature prediction discrepancies of between 5°C and 10°C. In addition, an evaluation of the camera's imaging parameters confirmed the predictions made based on the simulated camera response. It was confirmed that the measurement range of the system will decrease if it is tuned to measure lower temperatures. By comparing the simulated camera response with the experimental results, evidence for the presence of spectral peaks in the material's emission at the 800±10nm and 900±10nm wavelengths was found. The evaluation of the camera's imaging parameters also confirmed that the dynamic range of the surface radiation between 800°C to 500°C is much greater than the dynamic range of the camera at any of the chosen camera settings. Although no individual choice of camera settings could deliver the desired measurement range, the addition of high dynamic range imaging techniques are expected to allow the system to measure temperatures across the entire 800°C to 500°C range. As a result, it is highly recommended that high dynamic range imaging techniques be explored further in future.

The experiments involving the effects of surface roughness and perspective angle suggested that a failure to account for these effects can lead to measurement errors of approximately ±30°C, however, it should be noted that this result was determined from a limited sample size of only 4 samples. As a result, it is recommended that future work be dedicated to improving the understanding of how material chemistry, surface roughness, surface oxidation, and perspective angle influence the calibration results. It is also recommended that future work be conducted in order to quantify the measurement precision which is required for the intended application of weld temperature monitoring and microstructure prediction. It is necessary to specify the required measurement accuracy and range so that effort is not wasted in the pursuit of unnecessarily precise calibrations

In order to test the capabilities of the thermal imaging system in a manner more akin to weld monitoring and microstructure prediction, it is recommended that the test equipment be programmed to

perform a heat treatment of the AISI 4140 material while under the observation of the CCD cameras. By using the temperature control system to heat the sample into the austenitization range, maintain its temperature for a specified dwell time, and then cool the sample at a slow controlled rate, the resulting hardness and microstructure of the sample should be relatively easy to predict based on the CCT curve for AISI 4140. If the cooling rate measured by the CCD camera system matches with that of the programmed cooling rate, the subsequent work of testing the thermal imaging system as a weld monitoring and microstructure prediction can proceed with added confidence.

In summary, a thermal imaging system based on low cost CCD sensors has been developed along with all the required calibration equipment, control systems, support software, and data analysis techniques. In addition, some preliminary investigations into the accuracy of the system and the effects of surface conditions have been conducted. A plan for future work has also been provided in order to transition towards using the system as a weld monitoring and microstructure prediction device.

References

- [1] M. A. Yassin, S. M. S. Khairul, I. Mahadzir and A. K. Basim, "History of Elements and Welding Processes," *Australian Journal of Basic and Applied Sciences*, vol. VIII, no. 13, pp. 296-315, 2014.
- [2] "Welding History Images: Depictions of Welding in Art, People, Stamps, and Engineering," 2016. [Online]. Available: <http://www.weldinghistory.org/whfolder/common/graphics.html>. [Accessed 20 July 2016].
- [3] GoWelding, "The History of Welding," [Online]. Available: <http://www.gowelding.org/articles/history-of-welding/>. [Accessed 21 July 2016].
- [4] Burke Enterprises, "Women of World War II: Photos of WWII Civilian Workers," 2016. [Online]. Available: <http://www.womenofwwii.com/civilians.html>. [Accessed 19 July 2016].
- [5] T. Eager, "Welding and Joining - Moving from Art to Science," *Welding Journal*, vol. 74, no. 6, pp. 49-55, 1995.
- [6] K. Sindo, *Welding Metallurgy* Second Edition, Hoboken, NJ: John Wiley & Sons, 2003.
- [7] L. Lindgren, "Finite Element Modeling and Simulation of Welding Part 1: Increased Complexity," *Journal of Thermal Stresses*, vol. 24, no. 2, pp. 141-192, 2001.
- [8] T. Zacharia and e. al, "Modeling of Fundamental Phenomena in Welds," *Materials Science and Engineering*, vol. 3, no. 2, 1995.
- [9] A. Spille-Kohoff, "Arc Welding: From Process Simulation to Structural Mechanics Part I: Process Simulation with ANSYS CFX," in *European Automotice Simulation Conference*, Munich, 2009.
- [10] Z.-K. Liu, L.-Q. Chen, K. E. Spear and C. Pollard, "An Integrated Education Program on Computational Thermodynamics, Kinetics, and Materials Design," *Journal of Materials*, no. Web-Only Supplement, 2003.
- [11] J. F. Lancaster, *Metallurgy of Welding: Sixth Edition*, Cambridge: Woodhead Publishing, 1999.
- [12] A. K. Sinha, *Physical Metallurgy Handbook*, McGraw-Hill, 2003.
- [13] K. Easterling, "The Heat-Affected Zone," in *Introduction to the Physical Metallurgy of Welding: Second Edition*, Butterworth-Heinemann, 1992, pp. 126-190.
- [14] D. R. Askeland and P. P. Phule, "Heat Treatment of Steels and Cast Irons," in *The Science and Engineering of Materials*, Toronto, Nelson, 2006, pp. 460-487.
- [15] D. H. Phillips, *Welding Engineering: An Introduction*, Chichester: John Wiley and Sons, 2016.

- [16] Canadian Center for Welding and Joining, "COMSOL Multiphysics," [Online]. Available: https://sites.ualberta.ca/~ccwj/lab/equipment/computer_programs/comsol.html. [Accessed 23 July 2016].
- [17] HKS Prozesstechnik, "ThermoProfil Scanner," [Online]. Available: <http://www.hks-prozesstechnik.de/en/products/thermoprofilscanner/>. [Accessed 23 July 2016].
- [18] Flir, "Flir A315/A615," 2016. [Online]. Available: <http://www.flir.com/automation/display/?id=41330>. [Accessed 26 July 2016].
- [19] G. Stott, "Ingots in Melt Shop in Steel Mill," [Online]. Available: <http://www.masterfile.com/stock-photography/image/700-00009233/Ingots-in-Melt-Shop-in-Steel-Mill>. [Accessed 9 August 2016].
- [20] G. Zauner, D. Heim, K. Niel, G. Hendorfer and H. Stoeri, "CCD cameras as thermal imaging devices in heat treatment processes," *Proceedings of SPIE*, vol. 5303, 2004.
- [21] F. Meriaudeau, "Real time multispectral high temperature measurement: Application to control in the industry," *Image and Vision Computing*, vol. 25, pp. 1124-1133, 2007.
- [22] S. Yamashita, A. Fujinaga, M. Yamamoto, K. Shinozaki, K. Kadoi, K. Mitsui and H. Usui, "In-situ Temperature Measurement using Monochrome High-speed Sensors during Laser Welding," *Quarterly Journal of the Japan Welding Society*, vol. 31, no. 4, pp. 78-81, 2013.
- [23] M. Tanaka, K. Waki, S. Tashiro, K. Nakata, E. Yamamoto, K. Yamazai and K. Suzuki, "Visualization of 2D Temperature Distribution of Molten Metal in Arc Welding Process," *Transactions of Joining and Welding Research Institute*, vol. 38, no. 2, 2009.
- [24] M. Planck, *The Theory of Heat Radiation*, New York: Dover Publications, 1959.
- [25] J. R. Howell, R. Siegel and P. M. Menguc, "Chapter 1: Introduction to Radiative Transfer," in *Thermal Radiation Heat Transfer: Fifth Edition*, Boca Raton, CRC Press, 2010, pp. 1-40.
- [26] T. L. Bergman, A. S. Lavine, F. P. Incropera and D. P. Dewitt, "Chapter 12 Radiation: Processes and Properties," in *Fundamentals of Heat and Mass Transfer: Seventh Edition*, Hoboken, John Wiley and Sons, 2011, pp. 767-830.
- [27] K. Chrzanowski, "Influence of measurement conditions and system parameters on accuracy of remote temperature measurement with dualspectral IR systems," *Infrared Physics and Technology*, vol. 37, pp. 295-306, 1996.
- [28] Y. Touloukian and D. DeWitt, *Thermal Radiative Properties: Metallic Elements and Alloys*, New York: Plenum Publishing, 1970.
- [29] Teledyne DALSA, "CCD vs. CMOS," 2016. [Online]. Available: <https://www.teledynedalsa.com/imaging/knowledge-center/appnotes/ccd-vs-cmos/>. [Accessed 29 July 2016].
- [30] Axis Communications, "CCD and CMOS sensor technology: Technical white paper," October 2010. [Online]. Available:

http://www.axis.com/files/whitepaper/wp_ccd_cmos_40722_en_1010_lo.pdf. [Accessed 29 July 2016].

- [31] Sony Corporation, *ICX618ALA specification data sheet*.

- [32] The Imaging Source, "Industrial Cameras: Spectral Sensitivity," [Online]. Available: http://s1.dl.theimagingsource.com/api/2.0/packages/publications/whitepapers-cameras/wpspectsens/512e966b18/wpspectsens_1.10.en_US.pdf. [Accessed 2 August 2016].

- [33] Edmund Optics Incorporated, "Anti-Reflection (AR) Coatings," 2016. [Online]. Available: <http://www.edmundoptics.com/resources/application-notes/optics/anti-reflection-coatings/>. [Accessed 11 August 2016].

- [34] The Imaging Source, "The Imaging Source: Technology Based on Standards," 2016. [Online]. Available: <https://www.theimagingsource.com/>. [Accessed 31 August 2016].

- [35] ASTM Committee on Temperature Measurement, *Manual on the use of thermocouples in temperature measurement: Fourth Edition*, 1993.

- [36] N. Burley, R. Powell, G. Burns and M. Scroger, "The Nicrosil versus Nisil Thermocouple: Properties and Thermoelectric Reference Data," National Bureau of Standards, Washington, 1978.

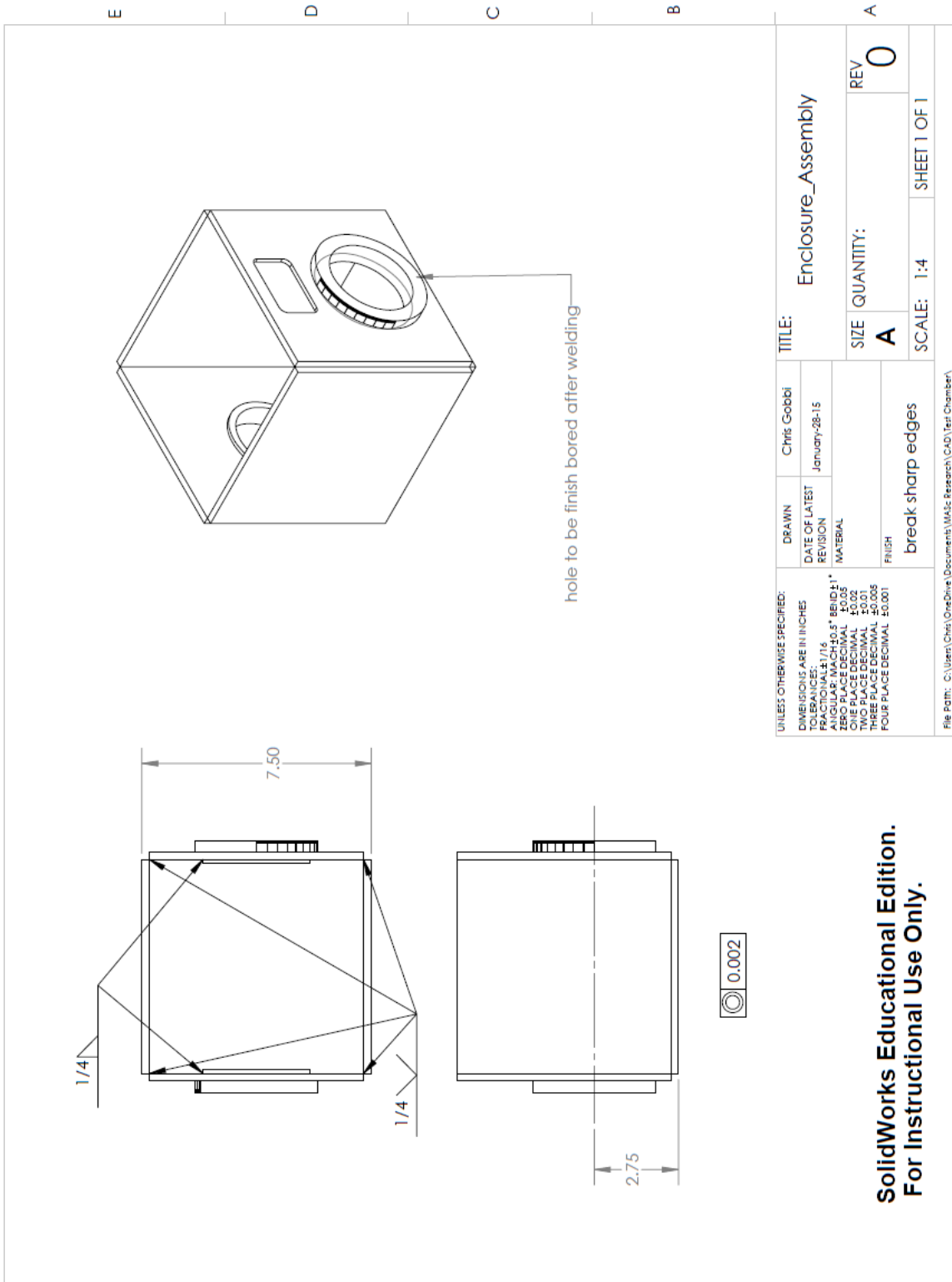
- [37] K. K. Montgomery, "Type N versus Type K Thermocouple Comparison in a Brick Kiln," [Online]. Available: <http://www.jms-se.com/catalog/file0109.pdf>. [Accessed 10 August 2016].

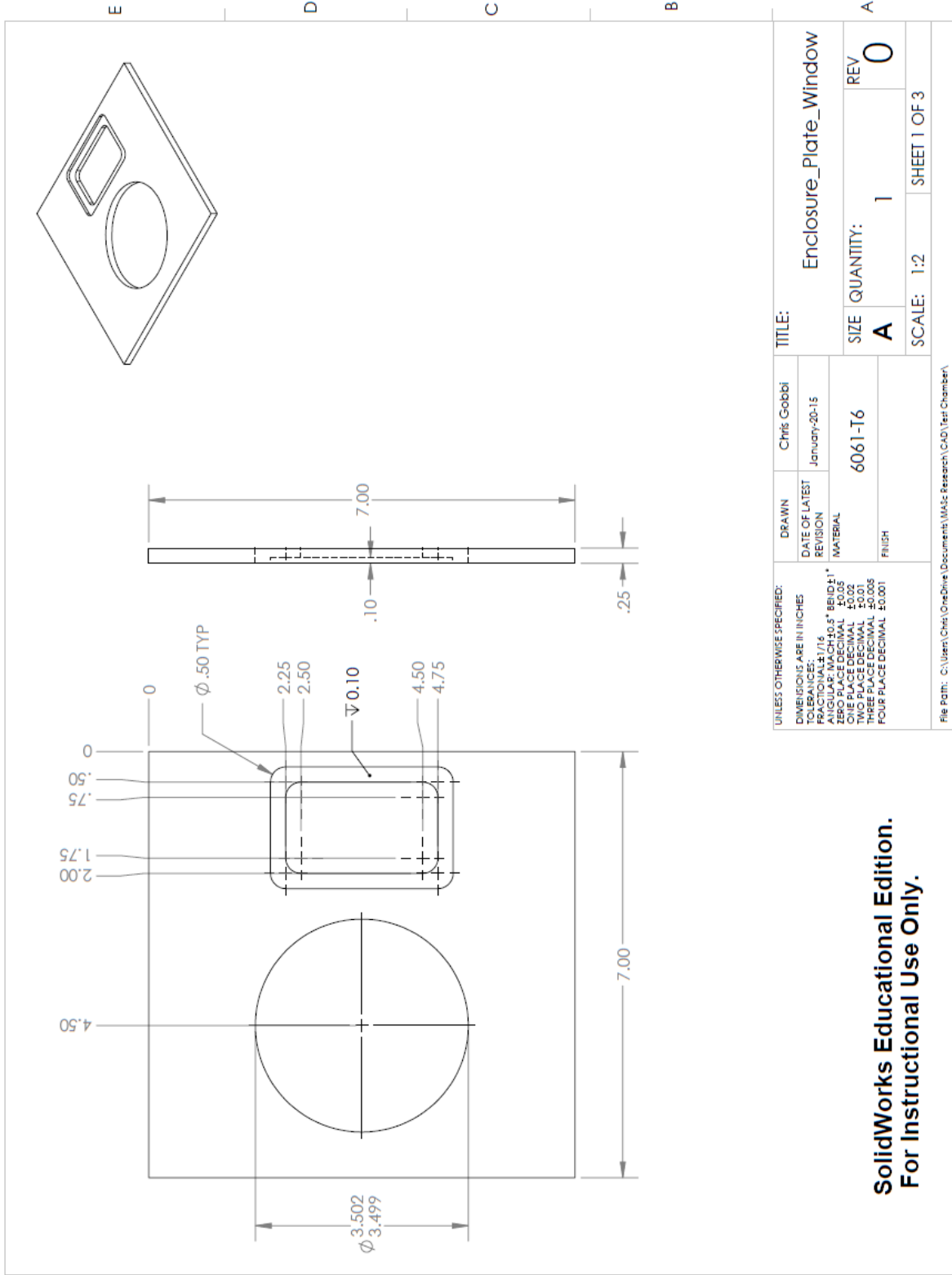
- [38] Edmund Optics, "800nm CWL, 10nm FWHM, 25mm Mounted Diameter," 2016. [Online]. Available: <http://www.edmundoptics.com/optics/optical-filters/bandpass-filters/traditional-coated-700-999nm-bandpass-interference-filters/65724/>. [Accessed 27 August 2016].

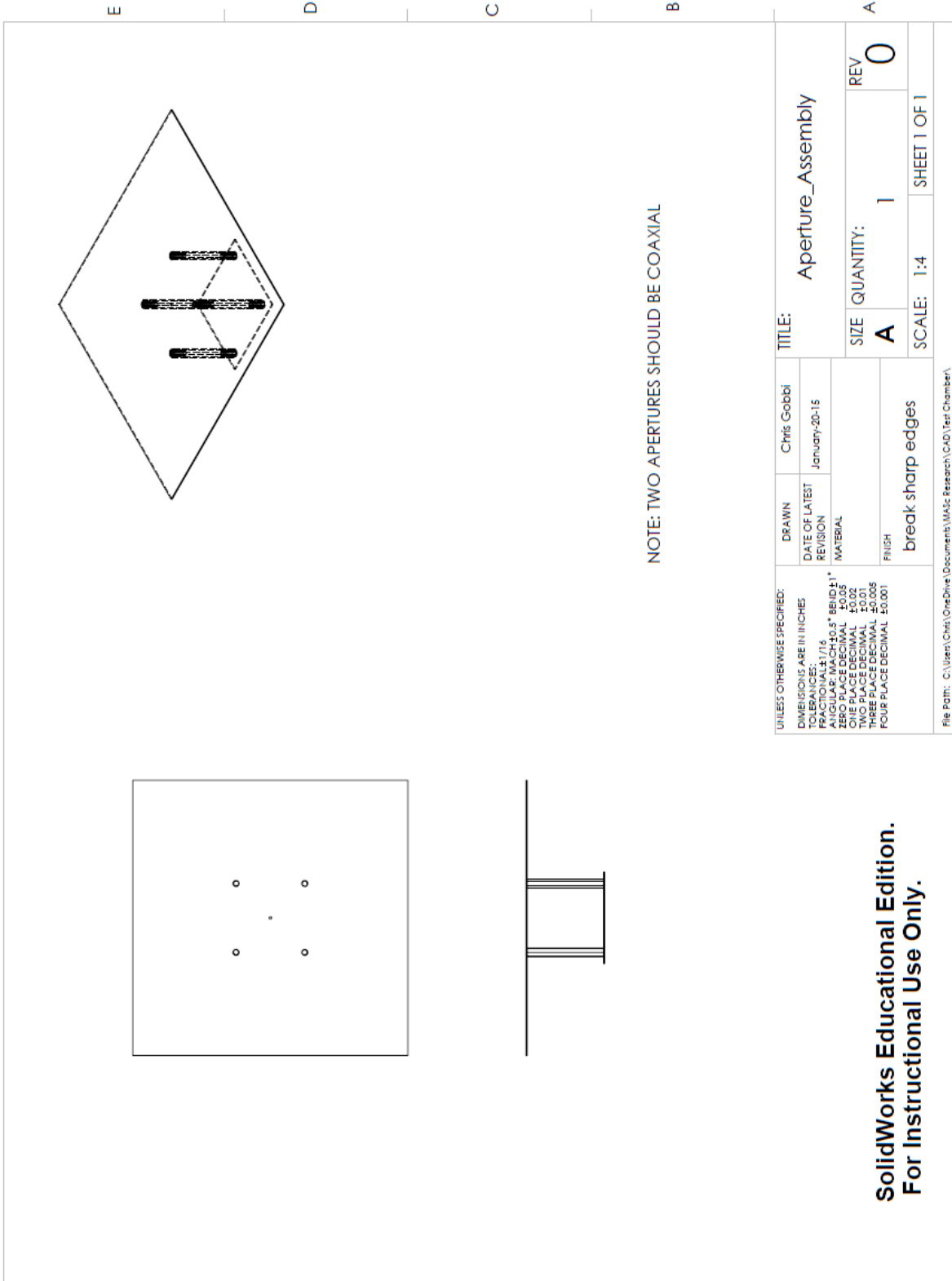
- [39] Edmund Optics, "900nm CWL, 10nm FWHM, 25mm Mounted Diameter," 2016. [Online]. Available: <http://www.edmundoptics.com/optics/optical-filters/bandpass-filters/traditional-coated-700-999nm-bandpass-interference-filters/67857/>. [Accessed 27 August 2016].

- [40] E. Reinhard, G. Ward, P. Sumanta, D. Paul, W. Heidrich and K. Myszkowski, "Introduction," in *High Dynamic Range Imaging: Acquisition, Display and Image-Based Lighting: Second Edition*, Morgan Kaufmann, 2010, p. 13.

Appendix A: Camera Calibration Chamber Dimensional Drawings



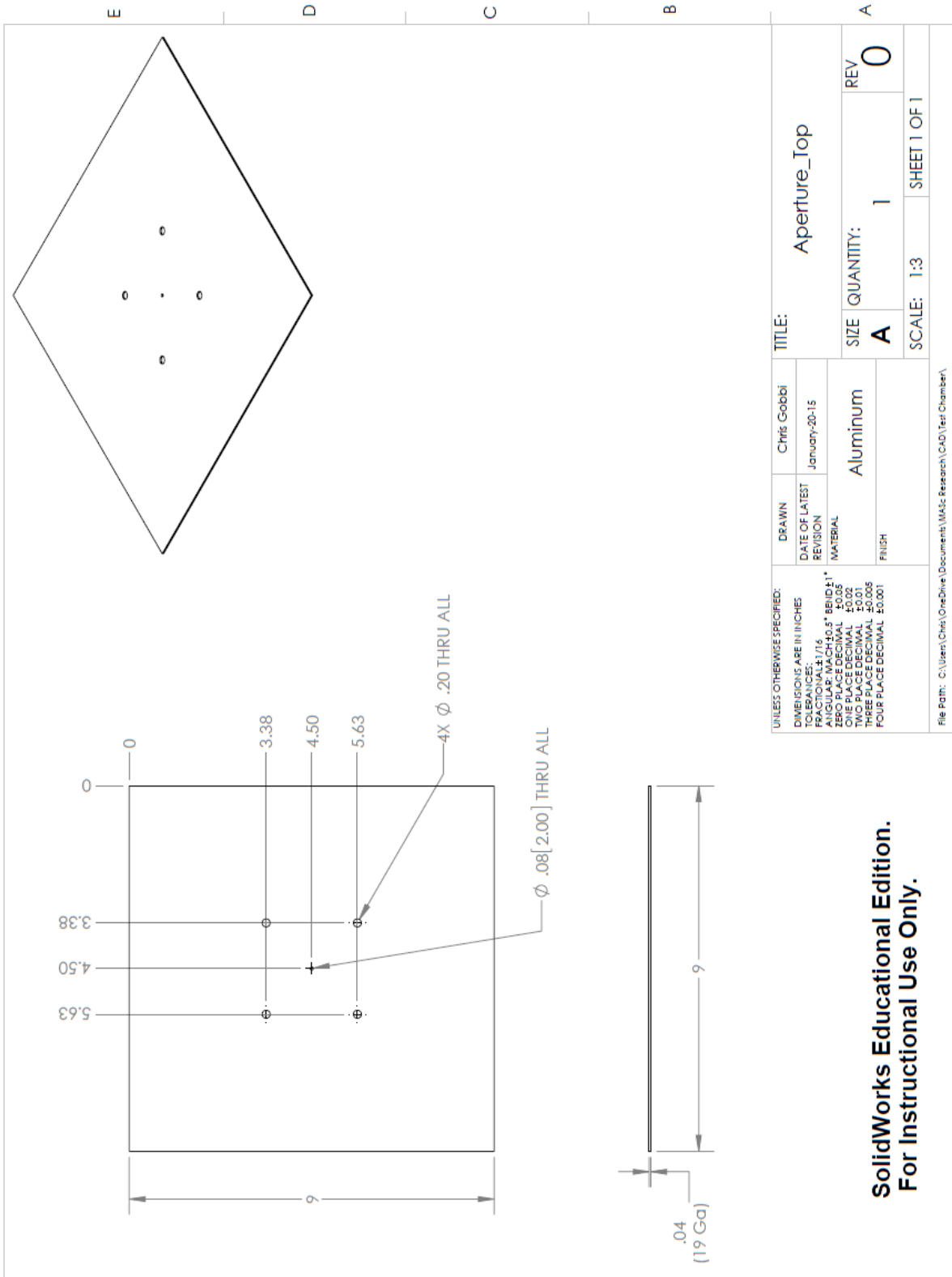




NOTE: TWO APERTURES SHOULD BE COAXIAL

UNLESS OTHERWISE SPECIFIED:		DRAWN	Chris Gobbi	TITLE:	Aperture_Assembly	
DIMENSIONS ARE IN INCHES		DATE OF LATEST REVISION	January-20-15	SIZE	A	REV
TOLERANCES:		MATERIAL		QUANTITY:	1	0
FRACTIONS: 1/16				SCALE:	1:4	SHEET 1 OF 1
DECIMALS: .0005				break sharp edges		
ANGULAR: MAX 40.5° BEND: 1°				File Path: C:\Users\Chris\OneDrive\Documents\W&S_Research\CAD\Test Chamber\		
ZERO PLACE DECIMAL ±0.05						
ONE PLACE DECIMAL ±0.02						
TWO PLACE DECIMAL ±0.005						
THREE PLACE DECIMAL ±0.0005						
FOUR PLACE DECIMAL ±0.0001						

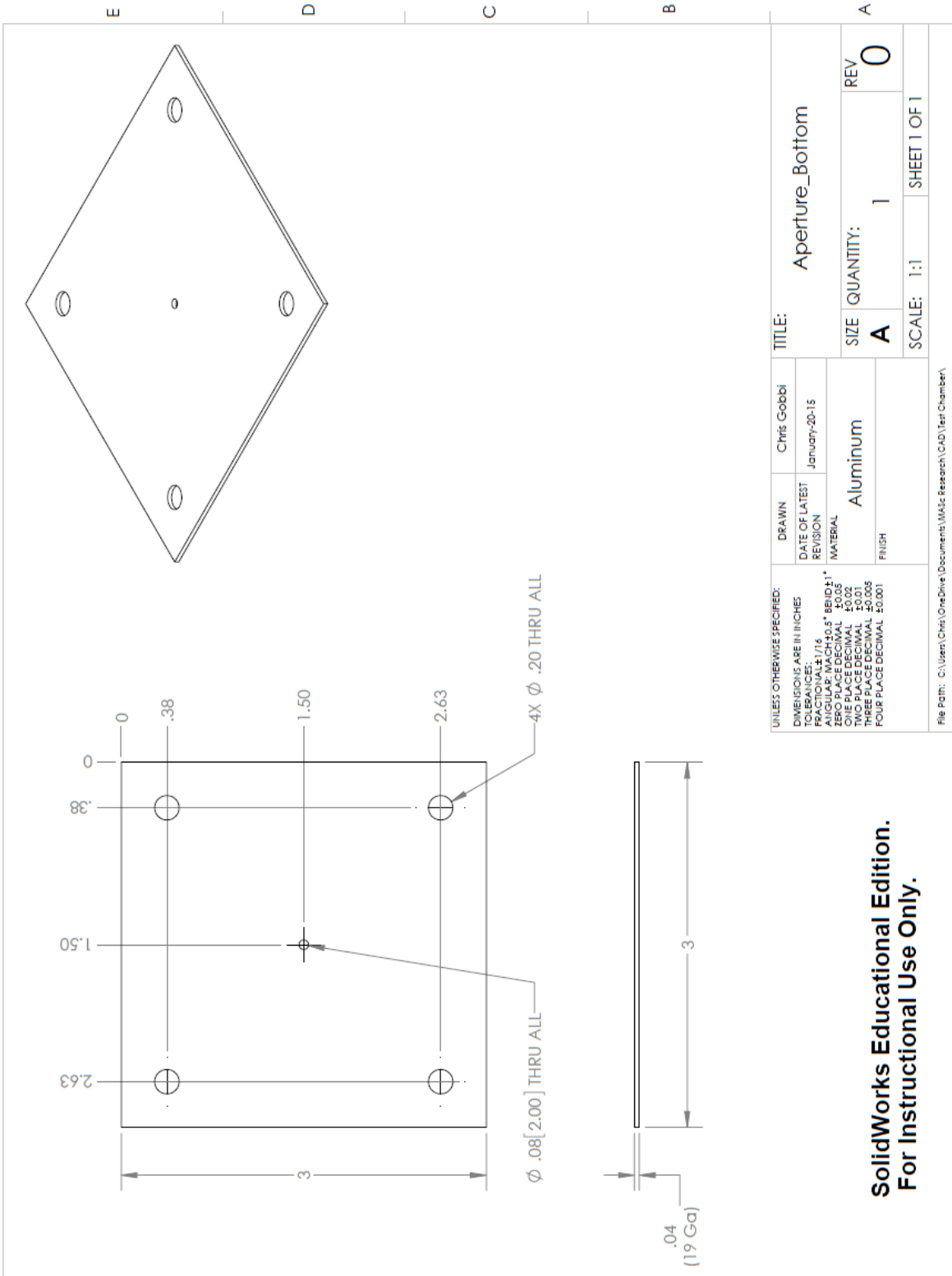
**SolidWorks Educational Edition.
For Instructional Use Only.**



UNLESS OTHERWISE SPECIFIED: DIMENSIONS ARE IN INCHES TOLERANCES: FRACTIONAL ± 1/16 DECIMAL ± 0.005 ZERO PLACE DECIMAL ± 0.005 ONE PLACE DECIMAL ± 0.02 TWO PLACE DECIMAL ± 0.01 THREE PLACE DECIMAL ± 0.005 FOUR PLACE DECIMAL ± 0.001		DRAWN DATE OF LATEST REVISION MATERIAL FINISH	Chris Gobbi January 20-15 Aluminum	TITLE: Aperture_Top
SIZE	QUANTITY:	REV		
A	1	0		
SCALE: 1:3		SHEET 1 OF 1		

**SolidWorks Educational Edition.
For Instructional Use Only.**

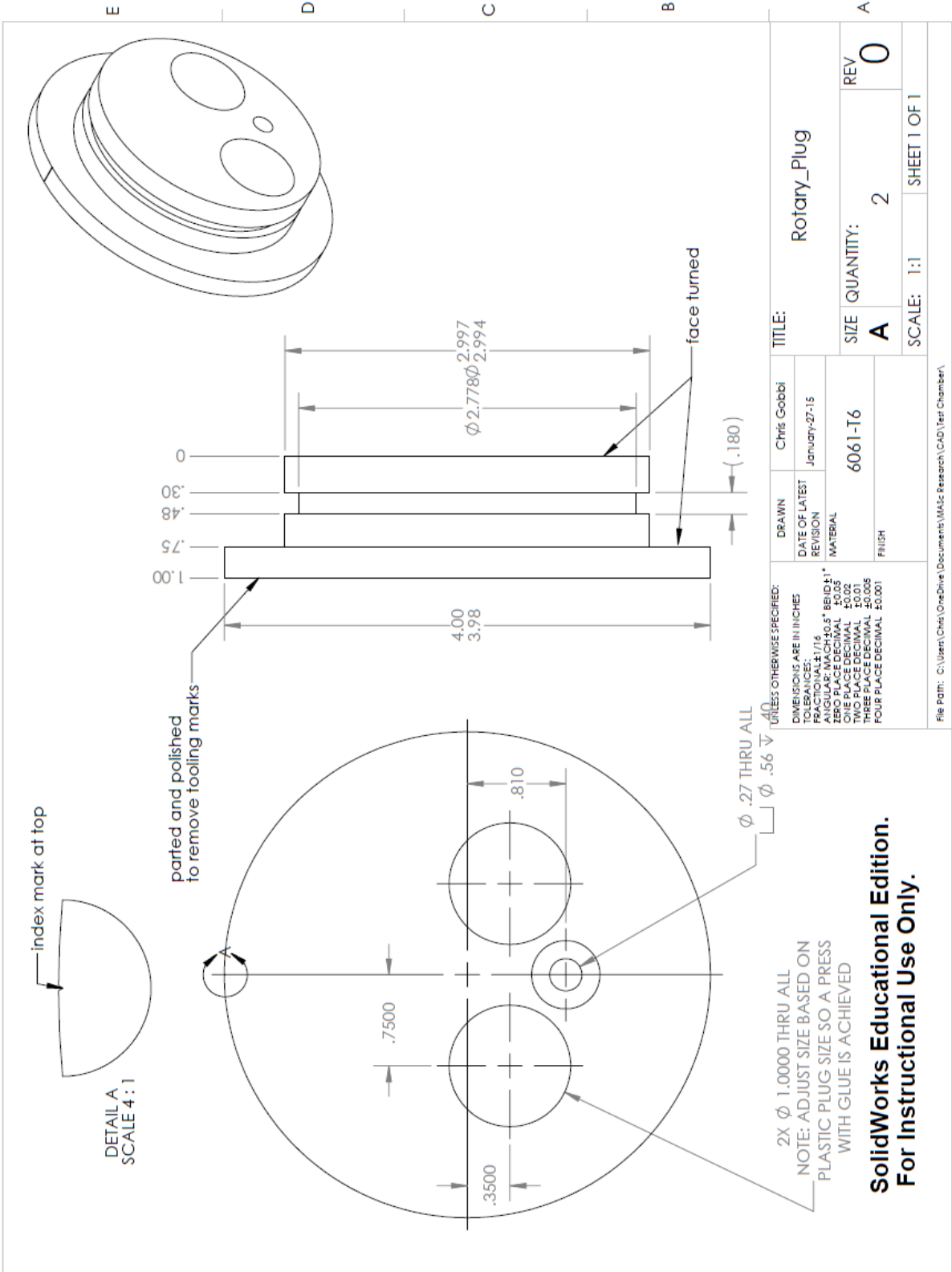
File Path: C:\Users\Chris\OneDrive\Documents\MAc Research\CAD Test Chamber\

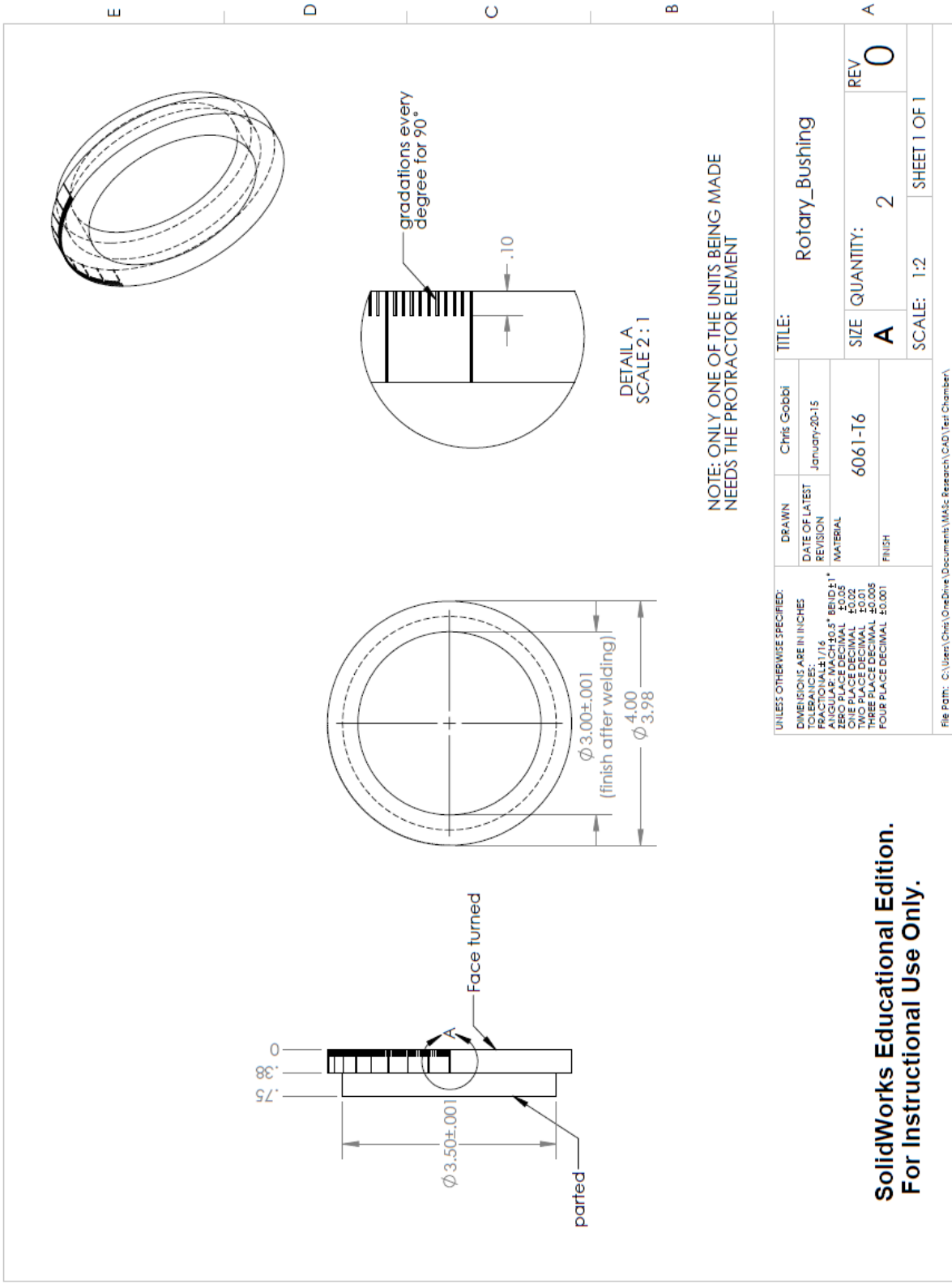


UNLESS OTHERWISE SPECIFIED:		DRAWN		TITLE:	
DIMENSIONS ARE IN INCHES		Chris Gobbi		Aperture_Bottom	
TOLERANCES:		DATE OF LATEST REVISION		SIZE	
FRACTIONAL: 1/16		January 20, 15		A	
DECIMAL: .005		MATERIAL		QUANTITY:	
ANGULAR: MACHOLS * BEVELS		Aluminum		1	
HOLE DIMENSIONS		FINISH		REV	
ONE PLACE DECIMAL ±0.01				O	
TWO PLACE DECIMAL ±0.01				SCALE: 1:1	
THREE PLACE DECIMAL ±0.005				SHEET 1 OF 1	
FOUR PLACE DECIMAL ±0.001					

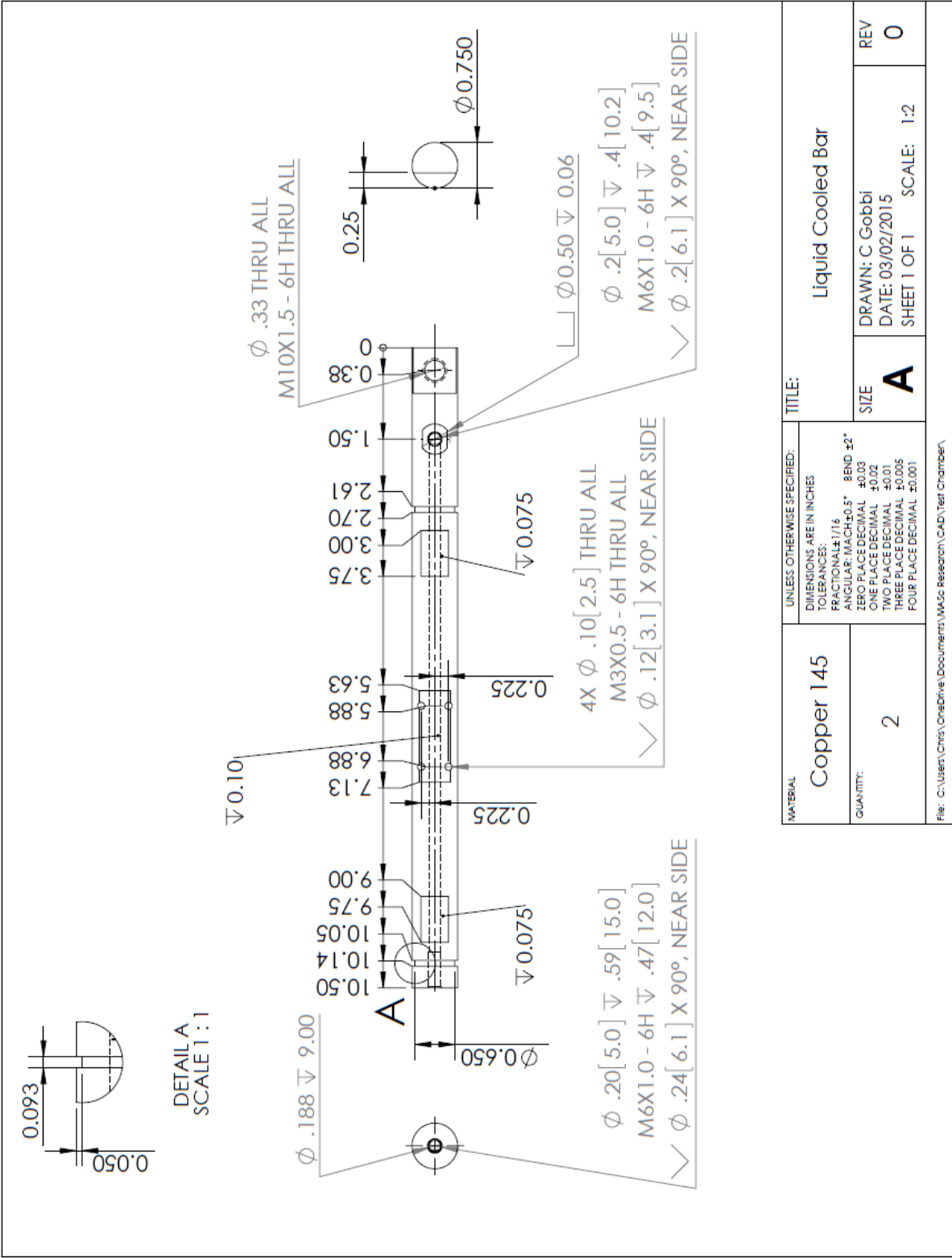
**SolidWorks Educational Edition.
For Instructional Use Only.**

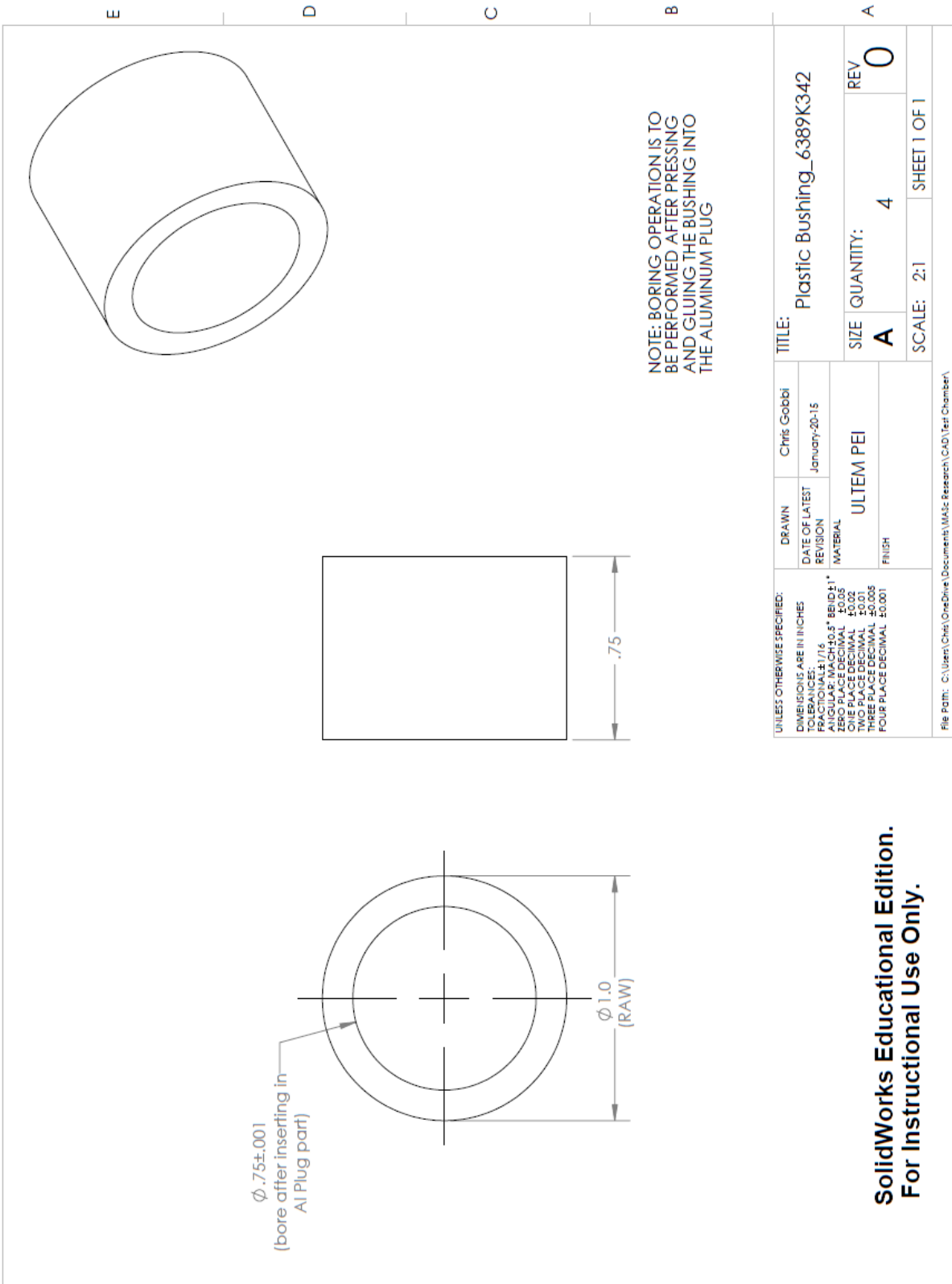
File Path: C:\Users\Chris\OneDrive\Documents\Misc Research\CAD\Test Chamber\



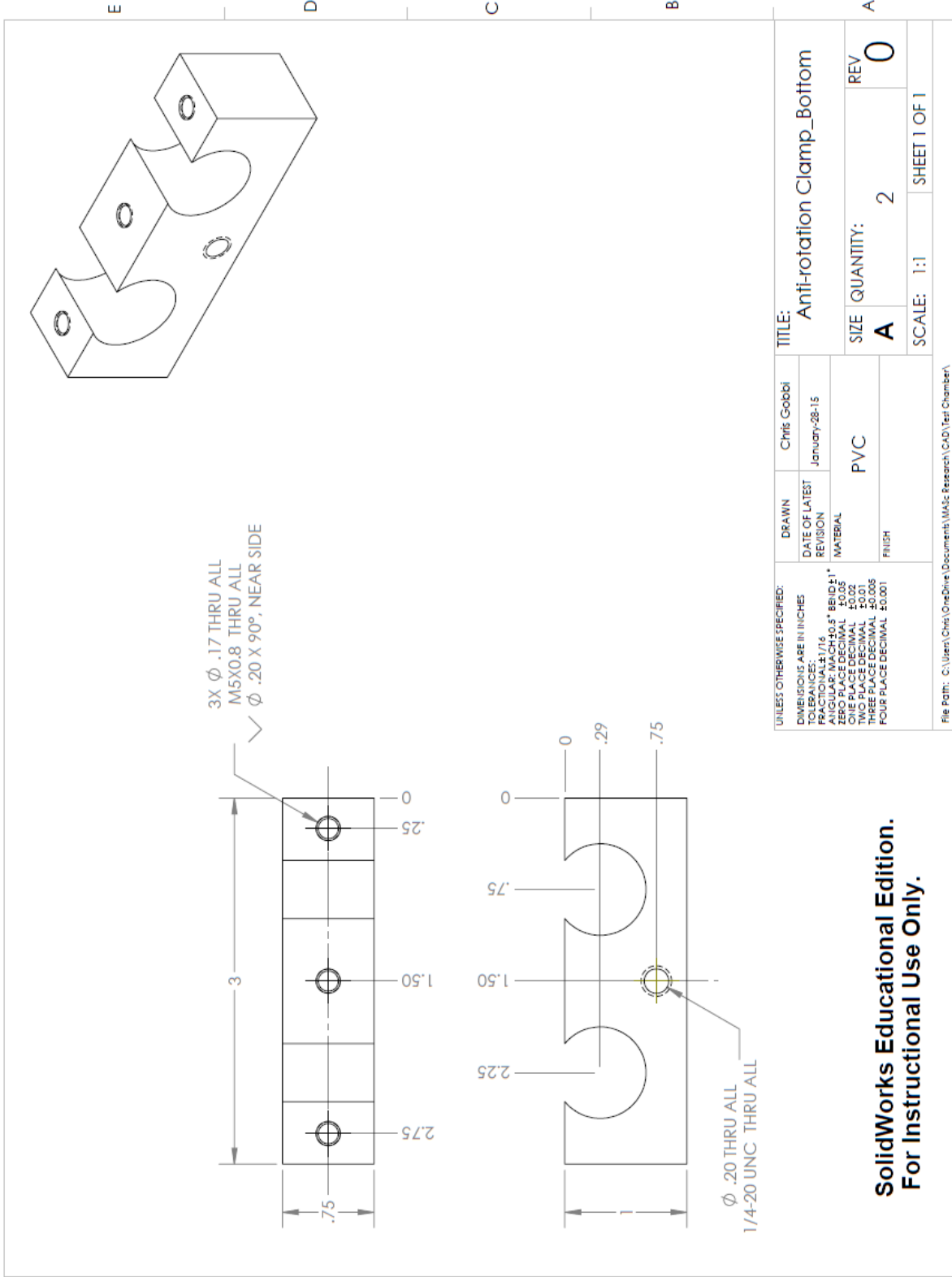


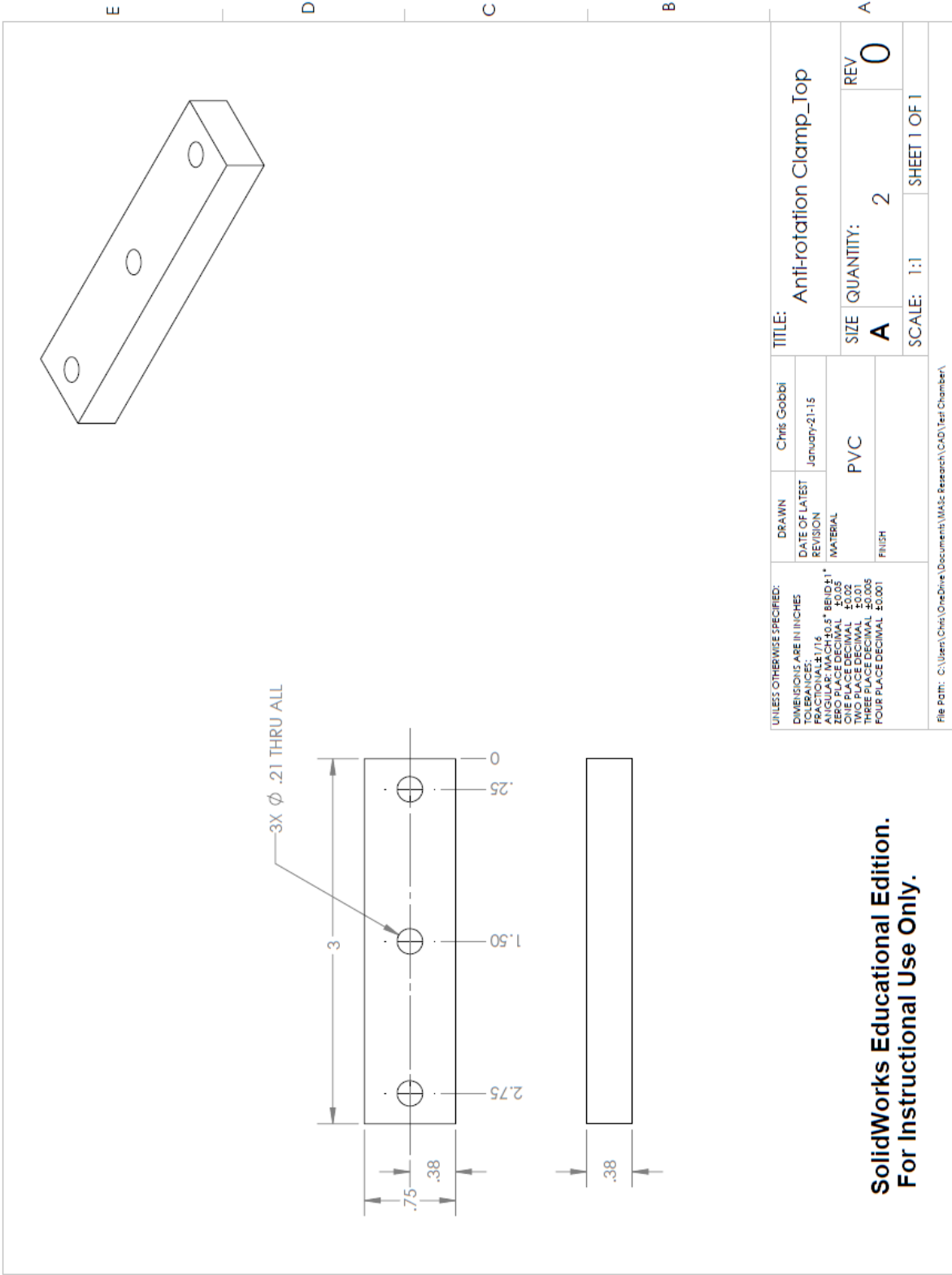
**SolidWorks Educational Edition.
For Instructional Use Only.**

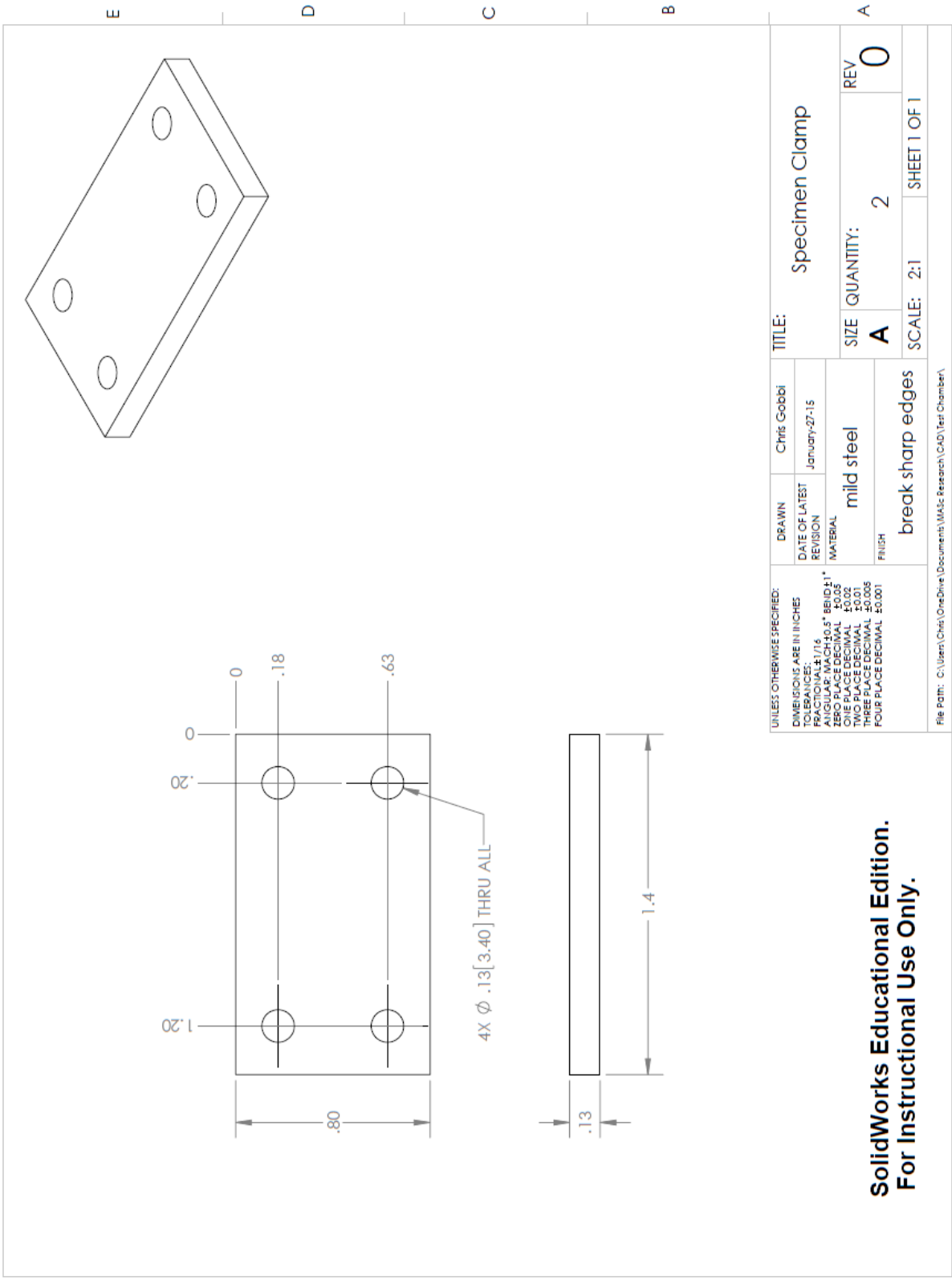




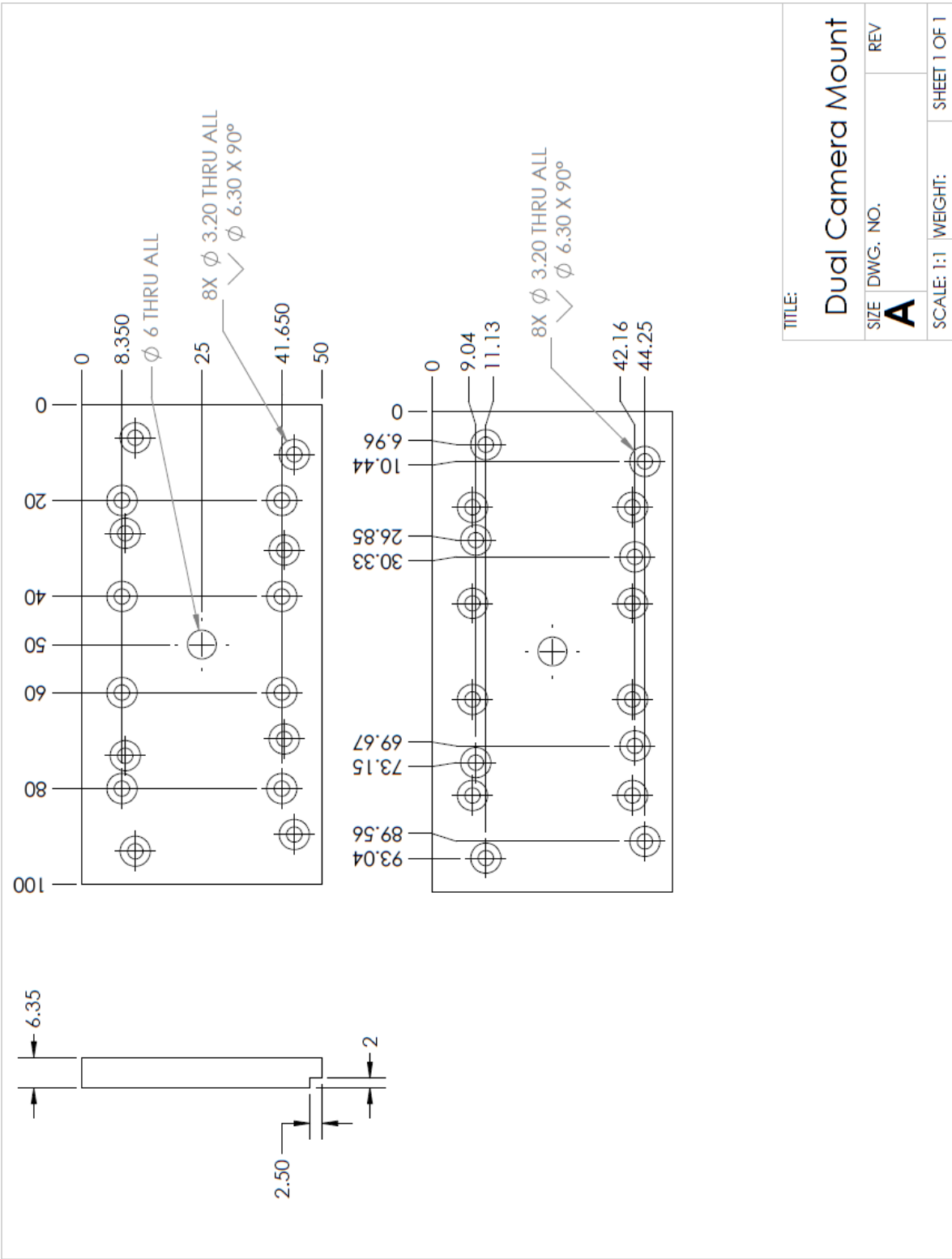
**SolidWorks Educational Edition.
For Instructional Use Only.**







**SolidWorks Educational Edition.
 For Instructional Use Only.**



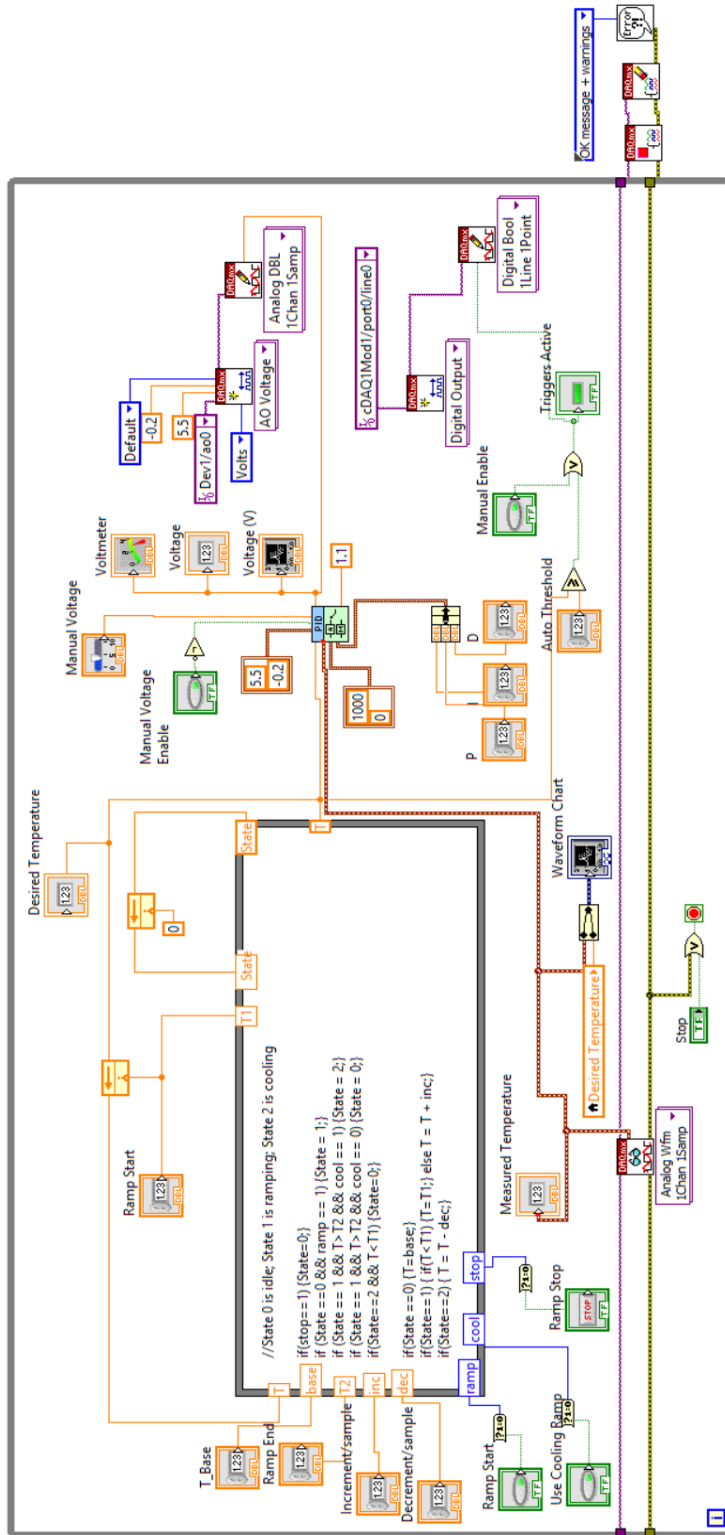
TITLE: Dual Camera Mount

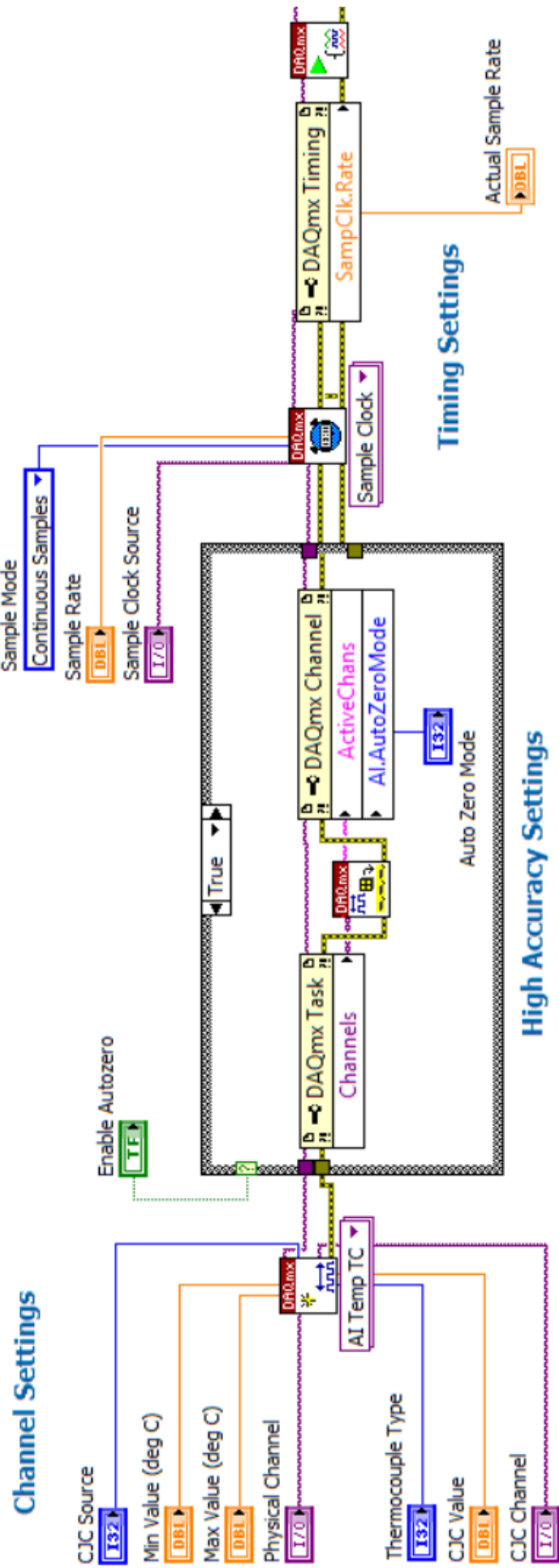
SIZE	DWG. NO.	REV
A		

SCALE: 1:1 WEIGHT: SHEET 1 OF 1

1 2 3 4 5

Appendix B: LabView Thermal Measurement and Control System





■ Stop

Desired Temperature 400 400.322 Measured Temperature

External Trigger Settings

Triggers Active ■

Auto Threshold Manual Enable

Ramp Settings

T_Base Increment/sample


Ramp Start Decrement/sample

Ramp End Use Cooling Ramp

Ramp Start Ramp Stop

Welder Control Settings

Manual Voltage Enable Manual Voltage



Voltmeter

P I D

Channel Settings

Physical Channel

Max Value (deg C) Min Value (deg C)

CJC Source CJC Value

CJC Channel Thermocouple Type

High Accuracy Settings

Enable Autozero* Auto Zero Mode

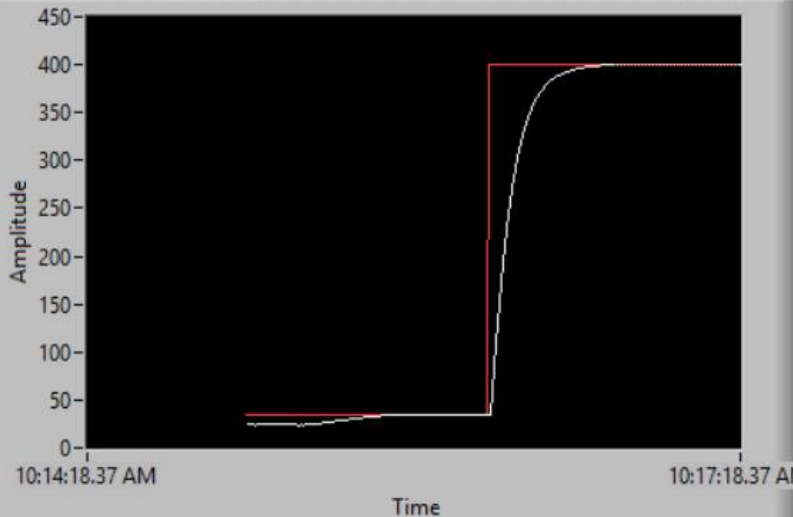
* Some devices do not support Auto Zero

Timing

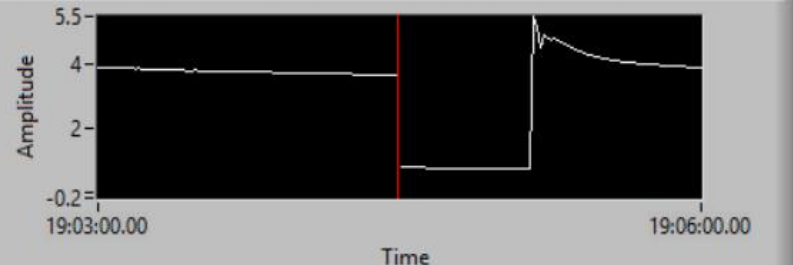
Sample Clock Source

Sample Rate Actual Sample Rate

Amplitude vs Time (10:14:18.37 AM to 10:17:18.37 AM)



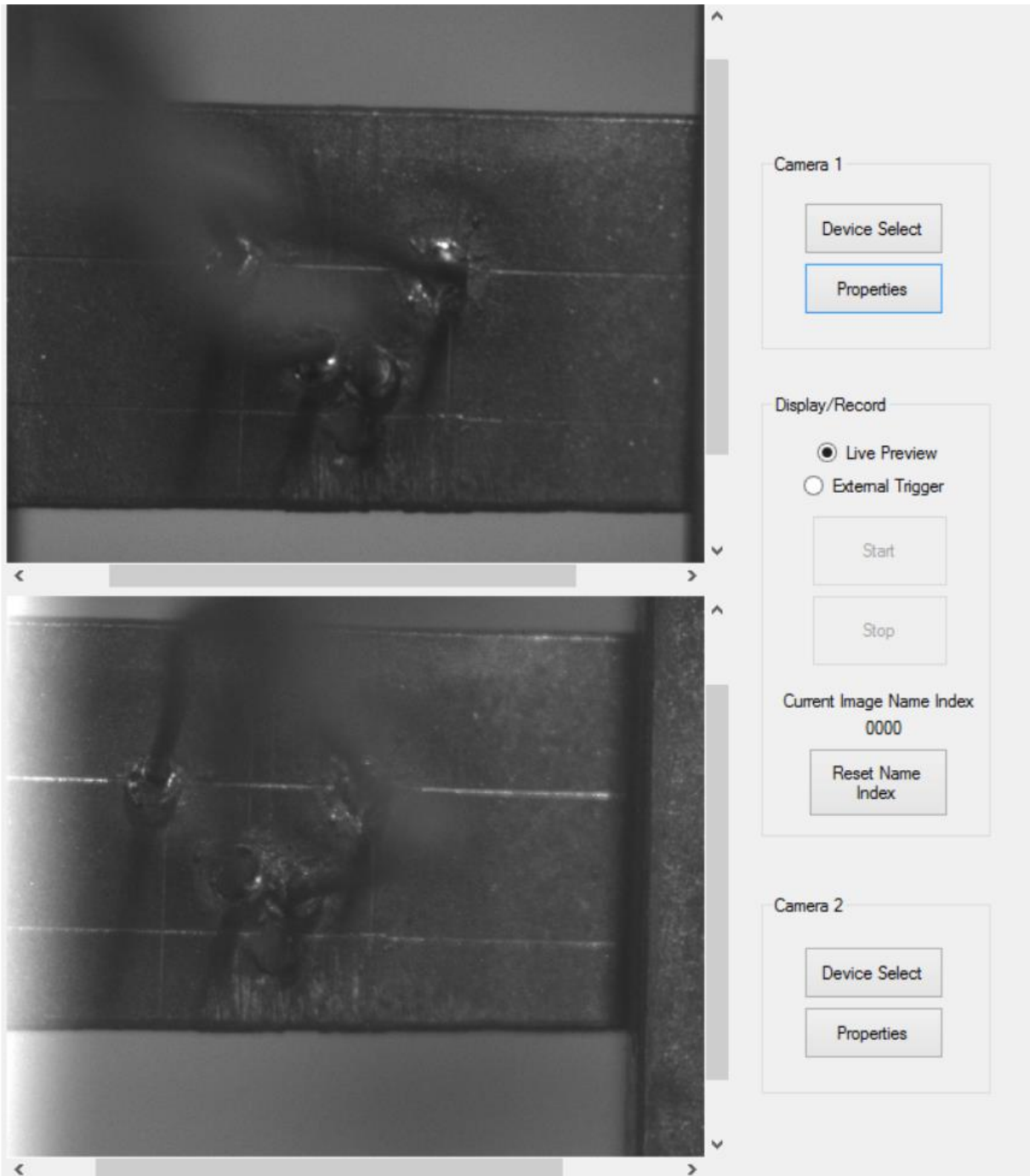
Amplitude vs Time (19:03:00.00 to 19:06:00.00)



Voltage

NOTES:
 For Integration gain, close to 0 is lots of gain while far from 0 is little gain
 For Derivative gain, large number is large

Appendix C: Dual Camera Graphical User Interface



Appendix D: Matlab Data Processing Code: Image_Processor_2CameraCalibrationProcessor_2.m

```
display('The image processing script works for pairs of grayscale  
bitmap images');  
display('press any key to run');  
pause;  
  
display('Select folder path for Cam1');  
FolderPathCam1 = uigetdir('C:\Users\Chris\OneDrive\Documents\MASc  
Research\Video Files');  
DirDataCam1 = dir(fullfile(FolderPathCam1, '*.bmp'));  
NumImagesCam1 = numel(DirDataCam1);  
NumImagesCam1 = cast(NumImagesCam1, 'uint16');  
  
display('Select folder path for Cam2');  
FolderPathCam2 = uigetdir('C:\Users\Chris\OneDrive\Documents\MASc  
Research\Video Files');  
DirDataCam2 = dir(fullfile(FolderPathCam2, '*.bmp'));  
NumImagesCam2 = numel(DirDataCam2);  
NumImagesCam2 = cast(NumImagesCam2, 'uint16');  
  
NumImages = min(NumImagesCam1, NumImagesCam2);  
Data = zeros(NumImages, 10);  
clear NumImagesCam1; clear NumImagesCam2;  
  
PreviewImageCam1 = imread(fullfile(FolderPathCam1,  
DirDataCam1(NumImages*4/5).name));  
%PreviewImage = transpose(PreviewImage);  
%imshow(PreviewImageCam1);  
display('Beginning Cam1 spatial calibration');  
Cam1_h1 = input('Please input vertical values of first point on  
horizontal line: ');  
Cam1_h2 = input('Please input vertical values of second point on  
horizontal line: ');  
Cam1_v1 = input('Please input horizontal values of first point on  
vertical line: ');  
Cam1_v2 = input('Please input horizontal values of second point on  
vertical line: ');  
Cam1X = (Cam1_v1 + Cam1_v2)/2;  
Cam1Y = (Cam1_h1 + Cam1_h2)/2;  
clear Cam1_h1 Cam1_h2 Cam1_v1 Cam1_v2;  
%close PreviewImageCam1;  
  
PreviewImageCam2 = imread(fullfile(FolderPathCam2,  
DirDataCam2(NumImages*4/5).name));  
%PreviewImage = transpose(PreviewImage);  
%imshow(PreviewImageCam2);  
display('Beginning Cam2 spatial calibration');
```

```

Cam2_h1 = input('Please input vertical values of first point on
horizontal line: ');
Cam2_h2 = input('Please input vertical values of second point on
horizontal line: ');
Cam2_v1 = input('Please input horizontal values of first point on
vertical line: ');
Cam2_v2 = input('Please input horizontal values of second point on
vertical line: ');
Cam2X = (Cam2_v1 + Cam2_v2)/2;
Cam2Y = (Cam2_h1 + Cam2_h2)/2;
clear Cam2_h1 Cam2_h2 Cam2_v1 Cam2_v2;
%close(PreviewImageCam2);

Cam2XOffset = cast(Cam2X - Cam1X, 'int16'); %this value will be added
to Cam2 to translate pixels to match Cam1
Cam2YOffset = cast(Cam2Y - Cam1Y, 'int16'); %this value will be added
to Cam2 to translate pixels to match Cam1

display('Beginning ROI setup (Cam1 is master)');
%imshow(PreviewImageCam1);
x1_temp = input('Please enter region of interest pixel X1: ');
y1_temp = input('Please enter region of interest pixel Y1: ');
x2_temp = input('Please enter region of interest pixel X2: ');
y2_temp = input('Please enter region of interest pixel Y2: ');

X1 = min(x1_temp, x2_temp);
X2 = max(x1_temp, x2_temp);
Y1 = min(y1_temp, y2_temp);
Y2 = max(y1_temp, y2_temp);
X1_2 = X1+Cam2XOffset;
X2_2 = X2+Cam2XOffset;
Y1_2 = Y1+Cam2YOffset;
Y2_2 = Y2+Cam2YOffset;

clear x1_temp y1_temp x2_temp y2_temp;
NumPixels = (X2-X1+1)*(Y2-Y1+1);
display(NumPixels);

display('processing...');

for n = 1:NumImages
    Temp1 = imread(fullfile(FolderPathCam1, DirDataCam1(n).name));
    Crop1 = Temp1(Y1:Y2, X1:X2);% y's are first since matlab expects
(row, col)
    Crop1 = cast(Crop1, 'double');
    Crop1 = reshape(Crop1, [], 1);

    Temp2 = imread(fullfile(FolderPathCam2, DirDataCam2(n).name));
    Crop2 = Temp2(Y1_2:Y2_2, X1_2:X2_2);% y's are first since matlab
expects (row, col)
    Crop2 = cast(Crop2, 'double');

```



```

Crop2 = reshape(Crop2,[],1);

Mean1 = mean(Crop1);
Min1 = min(Crop1);
Max1 = max(Crop1);
Range1 = Max1-Min1;
STDEV1 = std(Crop1);

Mean2 = mean(Crop2);
Min2 = min(Crop2);
Max2 = max(Crop2);
Range2 = Max2-Min2;
STDEV2 = std(Crop2);

Data(n,:) = [Mean1, Min1, Max1, Range1, STDEV1, Mean2, Min2, Max2,
Range2, STDEV2];
end

xlswrite(fullfile(FolderPathCam1, 'ImageStats'),Data);

display('The script has completed');
display('The Processed data is in workspace as "Data"');
display('An excel file has also been created in the folder containing
the image files');

```

Appendix E: Matlab Thermal Image Code: ThermallImageGenerator2.m

```
display('The thermal image generator is about to run');
display('Input images should be RGB .bmp images');
display('Be sure to input values for Poly and Range (Celsius)');
display('press any key to run');
pause;

%Poly=[0 0 0 0 0 0];
S=8;
display('Select file path for Cam1');
[FileNameCam1,FilePathCam1] =
uigetfile('C:\Users\Chris\OneDrive\Documents\MASc Research\Video
Files');

display('Select file path for Cam2');
[FileNameCam2,FilePathCam2] =
uigetfile('C:\Users\Chris\OneDrive\Documents\MASc Research\Video
Files');

Image1= imread(fullfile(FilePathCam1,FileNameCam1));
Temp1=Image1(:,:,1);
fig1PreFilter = figure;
fig1PreFilter.Name = 'Cam1 Preview';
imshow(Temp1);

Image2= imread(fullfile(FilePathCam2,FileNameCam2));
Temp2=Image2(:,:,1);
fig2PreFilter = figure;
fig2PreFilter.Name = 'Cam2 Preview';
imshow(Temp2);
%Temp2=cast(Temp2,'double');
%Temp2=imgaussfilt(Temp2, S);
%display('Paused: press any key to continue');
%pause;

display('Beginning Cam1 spatial calibration');
Cam1_h1 = input('Please input vertical values of first point on
horizontal line: ');
Cam1_h2 = input('Please input vertical values of second point on
horizontal line: ');
Cam1_v1 = input('Please input horizontal values of first point on
vertical line: ');
Cam1_v2 = input('Please input horizontal values of second point on
vertical line: ');
Cam1X = (Cam1_v1 + Cam1_v2)/2;
Cam1Y = (Cam1_h1 + Cam1_h2)/2;
clear Cam1_h1 Cam1_h2 Cam1_v1 Cam1_v2;

display('Beginning Cam2 spatial calibration');
```

```

Cam2_h1 = input('Please input vertical values of first point on
horizontal line: ');
Cam2_h2 = input('Please input vertical values of second point on
horizontal line: ');
Cam2_v1 = input('Please input horizontal values of first point on
vertical line: ');
Cam2_v2 = input('Please input horizontal values of second point on
vertical line: ');
Cam2X = (Cam2_v1 + Cam2_v2)/2;
Cam2Y = (Cam2_h1 + Cam2_h2)/2;
clear Cam2_h1 Cam2_h2 Cam2_v1 Cam2_v2;

Cam2XOffset = cast(Cam2X - Cam1X, 'int16'); %this value will be added
to Cam2 to translate pixels to match Cam1
Cam2YOffset = cast(Cam2Y - Cam1Y, 'int16'); %this value will be added
to Cam2 to translate pixels to match Cam1

display('Beginning ROI setup (Cam1 is master)');
%imshow(PreviewImageCam1);
x1_temp = input('Please enter region of interest pixel X1: ');
y1_temp = input('Please enter region of interest pixel Y1: ');
x2_temp = input('Please enter region of interest pixel X2: ');
y2_temp = input('Please enter region of interest pixel Y2: ');

X1 = min(x1_temp, x2_temp);
X2 = max(x1_temp, x2_temp);
Y1 = min(y1_temp, y2_temp);
Y2 = max(y1_temp, y2_temp);
X1_2 = X1+Cam2XOffset;
X2_2 = X2+Cam2XOffset;
Y1_2 = Y1+Cam2YOffset;
Y2_2 = Y2+Cam2YOffset;

clear x1_temp y1_temp x2_temp y2_temp;

Temp1=cast(Temp1,'double');
Temp1=imgaussfilt(Temp1, S);
fig1PostFilter = figure;
fig1PostFilter.Name = 'Cam1 Spatial Filter';
imshow(cast(Temp1,'uint8'));

Temp2=cast(Temp2,'double');
Temp2=imgaussfilt(Temp2, S);
fig2PostFilter = figure;
fig2PostFilter.Name = 'Cam2 Spatial Filter';
imshow(cast(Temp2,'uint8'));

Crop1 = Temp1(Y1:Y2, X1:X2, 1);% y's are first since matlab expects
(row, col)
Crop2 = Temp2(Y1_2:Y2_2, X1_2:X2_2, 1);% y's are first since matlab
expects (row, col)

```

```

Size = size(Crop1);
R = zeros(Size(1),Size(2));

fig1Crop = figure;
fig1Crop.Name = 'Cam1 Crop Spatial Filter';
imshow(cast(Crop1,'uint8'));

fig2Crop = figure;
fig2Crop.Name = 'Cam2 Crop Spatial Filter';
imshow(cast(Crop2,'uint8'));
%display('Paused: press any key to continue');
%pause;

for i=1:Size(1)
    for j=1:Size(2)
        R(i,j) = Crop2(i,j)/Crop1(i,j);
        %if R(i,j) > Range(2)
        %    R(i,j)=Range(2);
        %end
        %if R(i,j) < Range(1)
        %    R(i,j)=Range(1);
        %end
    end
end

T = polyval(Poly, R);
T = T-273;

for i=1:Size(1)
    for j=1:Size(2)
        if T(i,j) > Range(2)
            T(i,j)=Range(2);
        end
        if T(i,j) < Range(1)
            T(i,j)=Range(1);
        end
    end
end

Thermal = figure;
Thermal.Name = 'Thermal Image';
h=surf(T);
set(h, 'LineStyle', 'none');
colormap jet;
colorbar;

```